UNIVERSITÀ DI TRENTO
Dipartimento di Ingegneria Industriale

Doctoral School in Materials, Mechatronics and Systems Engineering

XXXII Cycle

Study of the anisotropic sintering shrinkage of green iron and stainless steel

Silvia Baselli

June 2020

STUDY OF THE ANISOTROPIC SINTERING SHRINKAGE OF GREEN IRON AND STAINLESS STEEL

Silvia Baselli
E-mail: silvia.baselli@unitn.it

Approved by:

Prof. Alberto Molinari, Advisor
Department of Industrial Engineering
University of Trento, Italy

Prof. Ilaria Cristofolini, Advisor
Department of Industrial Engineering
University of Trento, Italy

Ph.D. Commission:

Prof. Herbert Danninger,
Institute of Chemical Technologies and Analytics
Technische Universität Wien, Austria

Prof. José Manuel Torralba,
Department of Materials Science and Engineering and Chemical Engineering
Universidad Carlos III de Madrid, Spain

Prof. Vigilio Fontanari,
Department of Industrial Engineering
University of Trento*, Italy.*

University of Trento
Department of Industrial Engineering

June 2020

University of Trento -
Department of
Industrial Engineering

Doctoral Thesis

Silvia Baselli - 2020
Published in Trento (Italy) – by University of Trento

ISBN: - - - - - - - - -

To my family

CONTENTS

1.INTRODUCTION

Powder metallurgy (PM) is a near net-shape technology that guarantees excellent dimensional control and surface finishing in the production of parts with complex shapes. Press and sinter is the conventional PM process. The powder mix is compacted into rigid dies to obtain the so called green part that is subsequently sintered to promote the formation of metallic bonding between the powder particles. The differences in terms of geometrical and dimensional features between the green compact and the final part are related to the dimensional variations occurring during sintering, therefore, to preserve the cost effectiveness of the process, their in-depth knowledge is crucial. In this context, post-sintering machining should be limited to the realization of geometrical details that cannot be directly obtained through uniaxial cold compaction or to achieve strict tolerances required by specific applications. The dimensional changes in sintering that may be either shrinkages or swellings are affected by many parameters and, among them, we can consider: material, presence of lubricant and additives, green density, compaction strategy, sintering temperature and time, atmosphere, heating and cooling rate. Furthermore, the dimensional variations along the direction parallel to compaction (longitudinal, axial) are different from the dimensional variations in the compaction plane (transversal, radial) causing an anisotropy that depends, in addition to the mentioned parameters, on the geometry and the dimension

of the part. At present, in absence of an adequate designing tool to account for the anisotropy, engineers rely on empirical methods often based on the trial-and-error approach.
International literature addresses the issue of sintering shrinkage and its anisotropy according to two approaches: physical metallurgy and continuum mechanics.

For some years, the Metallurgy Group of the University of Trento has started a research program aiming at studying the dimensional changes in sintering and their anisotropy according to the physical metallurgy approach and the present PhD thesis is part of this project.

The objectives are:

- Study of the effect of the green density on the sintering shrinkage and validation of a kinetic model for the isothermal shrinkage
- Study of the effect of the powder morphology, and then of the driving force correlated to the excess of surface area, on the sintering shrinkage
- Comparison of the results obtained with iron with those gained with austenitic stainless steel. AISI 316L is poorly affected by structural activity introduced by prior cold compaction since high sintering temperature is required to have shrinkage and, being paramagnetic, does not undergo the increase in volume diffusivity due to the dislocation pipe diffusion mechanism.

The work is organized as follow.
Chapter 2 is an overview of the state of the art in which the two theories (classical and continuum mechanics) that allow the study of the dimensional variations in sintering and their anisotropy are described and the important parameters identified.

For this study, two iron powders (atomized and sponge) and two austenitic stainless steel AISI 316L powders (coarse and fine) have been considered. First of all, they were characterized and the microstructure of the green parts, in terms of contact lengths between the particles, was studied. The dimensional changes during the whole sintering cycle were measured by means of dilatometry tests carried out both in the longitudinal and in the transversal direction, to investigate the anisotropy. The experimental procedures are comprehensively explained in Chapter 3.

A new kinetic equation for the isothermal shrinkage accounting for the extension of the interparticle contact areas is proposed in Chapter 4. Bulk diffusivity is the mass transport mechanism that determines the dimensional changes. The shrinkage is enhanced by the increase of the internal radius of the neck, that represents the geometrical activity in sintering of prior cold compacted powders.

After that, the focus passes to the results that are divided depending on the material in Chapter 5.

Through atomized iron, the effect of green density on the longitudinal and transversal shrinkage was investigated. In addition, the shrinkage kinetic model was validated. In particular, considering the geometrical activity of the green parts and the corresponding shrinkages on heating, the geometrical activity at the sintering temperature was estimated and, based on it, the theoretical isothermal shrinkages were calculated. Thanks to the effective diffusion coefficient as a function of the isothermal holding time it has been possible to evaluate the structural activity, that was found to be isotropic. From the comparison of the shrinkages of the samples produced with the atomized iron and sponge iron at green density of 6.9 g/cm^3, the influence of the morphology of the powder particles was assessed. The results showed that, on heating, the effect of deformation prevails and the morphology of the powder does not influence the shrinkage. On the contrary, the isothermal

shrinkage depends on the specific surface area since it affects the driving force of sintering.

AISI316L requires higher sintering temperature than iron to have shrinkage. Moreover, the contribute to the dimensional variations due to the dislocation pipe diffusion mechanism is expected to be modest. The dependence of the sintering shrinkage of such a material on the driving force related only to the particle size excluding others morphological aspects was evaluated considering two powders with different particle sizes.

At the end of the chapter, the differences between the behavior of iron and AISI 316L are pointed out.

Chapter 6 is dedicated to a preliminary study of the shrinkage that occurs on heating and it may represent a starting point for further development of the topics of this PhD thesis. The work ends with some concluding remarks.

2. STATE OF THE ART

The compaction pressure and the constrains exerted by the rigid die and core in the compaction plane lead to an anisotropic stress field that causes heterogeneous packing and deformation of the powder particles in the green parts. As a consequence, the dimensional variations in sintering are anisotropic. A link between sintering shrinkage and prior compaction was proposed by Kuroki [1], who demonstrated a correlation between the anisotropic shrinkage and the anisotropic springback during the ejection of the parts from the die cavity.

Sintering may be studied either through a microscopic or a macroscopic approach. The former is that of the physical metallurgy while the latter is that of continuum mechanics. The classical theory of sintering is based on the discrete nature of particulate media. Sintering is the result of thermally activated mechanisms that produce the growth of contacts between particles and their coalescence. The local kinetic of the process, which depends on the properties of the particles and the nature of their interaction, is generalized to predict the behavior of the part at a macroscopic level. The continuum theory of sintering uses the tools of the continuum mechanics and founds on the theories of plastic and nonlinear-viscous deformation of porous bodies. The flow of the material is studied as a rheological problem.

A study on the correlation between the macroscopic dimensional change and microscopic phenomena occurring at the interparticle regions was published by Vagnon *et al.*

[2]. By using in situ microtomography, the presence of two different types of pores in the green microstructure was highlighted: the larger and non-oriented packing pores and the smaller and oriented contact pores in the interparticle contact regions. Both these types of pore shrink during sintering, the formers just on heating. They also demonstrate the effect of the lubricant escape and of the relaxation of compaction residual stresses on the axial expansion during heating.

Both the theories deal with the issue of anisotropy. The classical theory of sintering identifies the causes in an anisotropic diffusivity because of a different dislocation density generated during cold compaction and an anisotropic extension of the contact areas between the powder particles. According to continuum theory of sintering, the sintering stress and the viscosity are anisotropic because of an inhomogeneity in the packing of the particles and in the pore morphology (the porosity is oriented).

2.1 CLASSICAL THEORY OF SINTERING

According to the classical theory, the sintering of a green part may be explained starting from the sintering of two powder particles. To this purpose, the behavior of identical and spherical particles in point contact is investigated [3]. The assumption of not strain hardened particles implies that the prior cold compaction is neglected. Sintering occurs under isothermal conditions. The reference publications for this approach are [4] and [5].

The driving force of sintering is the reduction of the total interfacial energy [6-13] which is, for a powder compact, the product between the specific surface energy γ and the total surface area *A* of the part.

$$\Delta(\gamma A) = \Delta\gamma A + \gamma\Delta A \qquad 2.1$$

This can happen because of a change in interfacial energy $\Delta\gamma$ due to densification and because of a change in interfacial area ΔA due to grain coarsening. The result of densification and coarsening are represented in Figure 2.1.

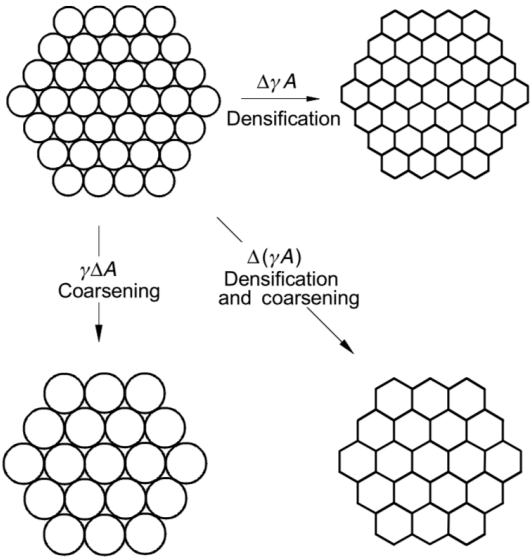

Figure 2.1 Schematic representation of densification and coarsening that occur under the driving force of sintering (adapted from [5])

In case of solid state sintering $\Delta\gamma$ is associated to the substitution of the solid/vapor interface with a solid/solid interface.

Mass transport mechanisms determine how the atoms move as a consequence of the driving force and can be divided in two classes depending on where the transport takes place: on the surface or through the volume. If the atoms forming the neck come from the bulk, sintering is accompanied by

shrinkage and densification while if the atoms source is the surface there is only redistribution of the material without reduction of the distance between the particles. The major mechanisms and the related parameters are listed in Table 2.1 and the corresponding paths are illustrated in Figure 2.2.

Table 2.1 Mass transport mechanisms and related parameters

Mechanism	**Source**	**Sink**	**Parameter**
Lattice diffusion	Grain boundary	Neck	Lattice diffusivity D_l
Grain boundary diffusion	Grain boundary	Neck	Grain boundary diffusivity D_b
Viscous flow	Bulk	Neck	Viscosity η
Surface diffusion	Surface	Neck	Surface diffusivity D_s
Lattice diffusion	Surface	Neck	Lattice diffusivity D_l
Evaporation/condensation	Surface	Neck	Vapor pressure difference Δp
Gas diffusion	Surface	Neck	Gas diffusivity D_g

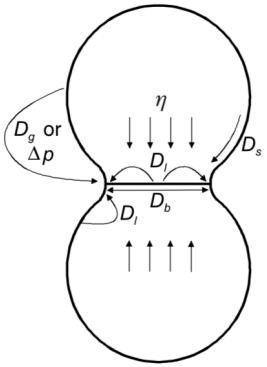

Figure 2.2 Major mass transport paths in sintering (adapted from [5])

The dominant mechanism may depend on several parameters such as particle size, neck radius, temperature and time.

The driving force for the mass flow to the neck is provided by the stress σ expressed by the Laplace equation (Equation 2.2):

$$\sigma = \gamma \left(\frac{1}{R_1} + \frac{1}{R_2}\right) \qquad 2.2$$

where γ is the surface energy and R_1 and R_2 are the principal curvature radii that, in the region of the neck, correspond to the internal and external neck radius and far from the neck are the radius a of the spherical particles.

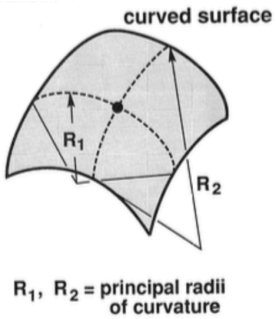

Figure 2.3 Principal curvature radii of a curved surface (adapted from [4])

It follows that, if the neck is small as at the initial stage of sintering, the curvature gradient is quite large while as the neck grows the gradient decreases. In the intermediate stage the gradient is around the cylindrical pores, in the final stage the curvature around the spherical pores drives the sintering. In sintering, the stress related to the interfacial energy that acts over curved surfaces is called sintering stress. The driving force may appear as a difference in bulk pressure ΔP, vacancy concentration ΔC and vapor pressure Δp:

$$\Delta P = P_{particle} - P_{neck} = \gamma \left(\frac{2}{a} + \frac{1}{r} - \frac{1}{X}\right) \approx \frac{\gamma}{r} \qquad 2.3$$

$$\Delta C_v = \Delta C_{v,0} \frac{\Omega_v}{kT} \frac{\gamma}{r} \qquad 2.4$$

$$\Delta p = p_0 \frac{\Omega}{kT} \frac{\gamma}{r} \qquad 2.5$$

where Ω_v is the atomic volume of vacancies and Ω the atomic volume of the solid. The atoms on the surface display an excess of chemical potential $\Delta\mu$ that depends on the sintering stress:

$$\Delta\mu = \Omega\sigma = \Omega\gamma \left(\frac{1}{R_1} + \frac{1}{R_2}\right) \qquad 2.6$$

Among the mass transport mechanisms let's consider the diffusion. The excess of chemical potential on the surface $\Delta\mu$ affects the vacancy concentration *C*

$$\Delta\mu = RT \ln\left(\frac{C}{C_0}\right) \qquad 2.7$$

The gradient of vacancy concentration over a curved surface is given by Kelvin equation

$$\Delta C \cong \frac{\gamma C_0 \Omega}{kT}\left(\frac{1}{R_1} + \frac{1}{R_2}\right) \qquad 2.8$$

where C_0 is the equilibrium concentration that depends on the temperature. On the particle surface the radius of curvature is positive, hence the vacancy concentration is lower than that of equilibrium. On the neck the situation is opposite: the curvature radius is negative, therefore the vacancy concentration is higher than that of equilibrium. The result is that there is a net flux of vacancies from the neck to the surface or equivalently a net flux of atoms in the opposite direction. To explain the sintering rate the Fick first law is applied:

$$J = D\frac{dC}{dx} \qquad 2.9$$

where *J* is the flux of vacancies or atoms, *D* is the diffusivity and *dC* the variation of vacancy concentration along the distance *dx*. Atoms can reach the neck through different paths and the volume of the neck changes according to Equation 2.10

$$\frac{dV}{dt} = JA\Omega \qquad 2.10$$

as a function of the flux of atoms *J* and the area *A* on which they are redistributed. Therefore, the geometrical configuration changes and the new neck curvature affects the flux. In Equation 2.11 the neck size ratio is expressed as a function of sintering time *t* in isothermal conditions

$$\left(\frac{X}{a}\right)^n = \frac{Bt}{(2a)^m} \qquad 2.11$$

where *X* and *a* are the radii respectively of the neck (internal) and the particle and the constants *n*, *m* and *B* depend on the mass transport mechanism (Table 2.2); *B* includes material and geometrical constants.

Table 2.2 Mass transport mechanisms and relative parameters *n*, *m* and *B*

Mechanism	n	m	B
Viscous flow	2	1	$3\gamma/\eta$
Plastic flow	2	1	$9\pi\gamma bD_v/kT$
Evaporation-condensation	3	1	$(3P\gamma/\rho^2)(\pi/2)^{1/2}(M/kT)^{3/2}$
Lattice (volume) diffusion	5	3	$80D_V\gamma\Omega/kT$
Grain boundary diffusion	6	4	$20\delta D_b\gamma\Omega/kT$
Surface diffusion	7	4	$56D_S\gamma\Omega^{4/3}/kT$

where

- γ = surface energy
- η = viscosity
- *b* = Burgers vector
- *k* = Boltzman constant

- T = absolute temperature
- ρ = theoretical density
- δ = grain boundary width
- D_S = surface diffusivity
- D_V = volume diffusivity
- D_b = grain boundary diffusivity
- M = molecular weight
- Ω = atomic volume

Many investigations have been conducted in order to determine the mechanisms of material transport during sintering according to different models and methods [14-18]. Some authors identified the grain boundary diffusion as the principal sintering mechanism [19-21]. Alexander and Balluffi [19] demonstrated that only the pores attached to the grain boundary shrink unlike those within the grains. Exner and Bross [21] analytically addressed the issue of stress distribution and grain boundary diffusion for symmetric and asymmetric necks formed during sintering of irregular particles or irregular arrangements of spherical particles. Kuczynski [22] took into account grain boundary diffusion and volume diffusion as mechanisms of densification during sintering of metallic powders and concluded that the latter is the more probable one. Friedrich and Schatt [23-25], studying the sintering of a copper sphere and plate, observed that the dislocation density in the contact regions increases during the early stage of the process, leading to the formation of dislocation rosette. This phenomenon is due to the local effect of capillary forces. Since the dislocations produced act as additional vacancy sink the result is a self-activation sintering due to an enhanced diffusion controlled flow of material to the neck. In [1,2, 26-32] the mass transport mechanisms responsible for sintering are surface diffusion and grain boundary diffusion, in particular Pan *et al.* [27] simulated the sintering of two spherical particles of

different sizes. Because of the driving force for the atoms movement, several mass transport mechanisms act simultaneously and independently, however only one of them prevail. Ashby [8] developed the sintering diagrams: depending on temperature, particle size and neck size the dominating mechanism for the neck grow rate is indicated. An example related to pure silver spheres sintering is represented in Figure 2.4.

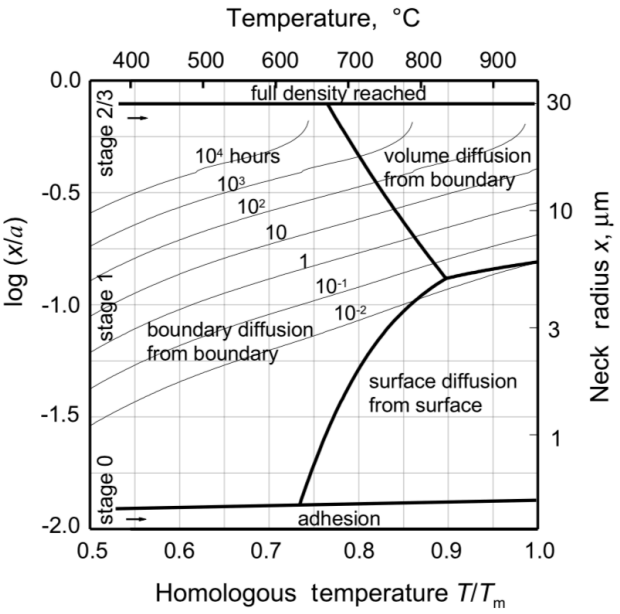

Figure 2.4 Sintering diagram of pure silver spheres of 38 µm radius (adapted from [5])

Along the boundary lines the neck growth rate for two mechanisms is equal. Inaccuracies in the data for the transport coefficients and disagreement between models lead to a spreading of the lines into bands. In practice, the diagrams are useful to understand under which conditions a single mechanism is supposed to be dominant and when only mixed mechanism models can describe the kinetics of the

neck growth. Furthermore, the diagrams provide information about sintering kinetics. In fact, lines at constant sintering time show the neck sizes for those periods of time at various temperatures. The elaboration of experimental isothermal shrinkage curves using the kinetic equation of the classical theory of sintering [4] led to the proposal [33-35] that the large density of structural defects in the deformed contact regions enhances bulk diffusivity, through the dislocation pipe diffusion mechanism. According to Smoluchowski [36] the dislocations may be viewed as cylindrical pipes characterized by a diffusivity D_p larger than that in the lattice D_V, thus the atoms move near them. Both D_V and D_P increase with temperature but, in correspondence of the Curie temperature (T_C) and of the austenitic transformation temperature ($T_{\alpha/\gamma}$), D_P registers a sharp enhancement (Figure 2.5) [37].

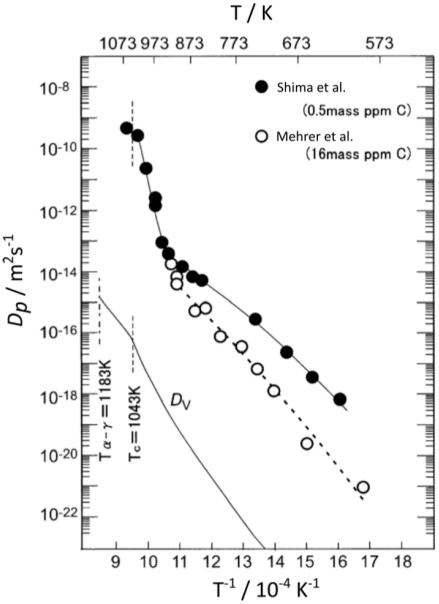

Figure 2.5 Volume and dislocation pipe diffusivity of α-Fe at equilibrium as a function of temperature (adapted from [37])

This phenomenon seems related to the disappearance of the magnetic moment of iron atoms in the pipes approaching T_C [38]. In case of low dislocation density and high temperature sintering the contribution of dislocation pipe diffusion is negligible. On the other hand, when the material is strain hardened and sintering occurs at lower temperatures, this mechanism dominates over volume and grain boundary diffusion because of its lower activation energy. Sintering shrinkage is, therefore, due to bulk diffusivity, and its anisotropy is the consequence of the anisotropic deformation of the particles. Since the axial compaction stress is greater than the radial/transversal one, the microstructure of green parts displays a different extension of the interparticle contacts and density of structural defects in the deformed regions, both being larger in the compaction direction [39]. These two characteristics of the green parts play an important role and define the geometrical activity and the structural activity in sintering, respectively.

2.2 CONTINUUM THEORY OF SINTERING

The first author who studied sintering according to a rheological point of view was Frenkel in 1945, although the model developed can not be considered a continuum mechanics approach. In [40] the coalescence of viscous particles driven by surface tension was studied:

$$-\frac{\partial \gamma}{\partial t} = 2\eta \dot{\varepsilon}^2 V \qquad 2.12$$

γ is the surface tension, t is the time, η the viscosity, ε the shrinkage rate and V the volume. Mackenzie and Shuttleworth [41] amplified these ideas, sintering is described as a uniform compression of a porous medium

characterized by two viscosity moduli that depend on the porosity. The densification of a porous material containing isolated spherical pores was taken into account. Skorohod is the author of a thermodynamically founded rheological theory of sintering [42]. Sintering is seen as a macroscopic process of volume and shape deformation related to the flow of substance within the skeleton of a porous body. The continuum theory of sintering is based on the theories of plastic deformation of porous bodies [43-45] and of nonlinear-viscous deformation of porous bodies [46-48].

Olevsky [49] formulated a phenomenological model of sintering founded on the concept of thermodynamics of irreversible processes. According to this theory the porous material is assumed to be biphasic, formed by the substance (skeleton) and the voids (pores). The skeleton is made by individual particles characterized by a nonlinear-viscous incompressible behavior, the voids are homogeneously dispersed. The general reaction is isotropic. The main constitutive law is Equation 2.13:

$$\sigma_{ij} = \frac{\sigma(W)}{W}\left[\varphi\dot{\varepsilon}_{ij} + \left(\psi - \frac{1}{3}\varphi\right)\dot{e}\delta_{ij}\right] + P_L\delta_{ij} \qquad 2.13$$

where

- σ_{ij} = *ij* components of the stress tensor
- $\dot{\varepsilon}_{ij}$ = *ij* components of the strain rate tensor
- $\sigma(W)$ = effective stress
- W = equivalent effective strain rate
- $\dot{e}$ = volume change rate
- φ = shear modulus, it represents the resistance to the shape change
- ψ = bulk modulus, it represents the resistance to the volume change
- δ_{ij} = Kronecker delta
- P_L = effective Laplace pressure (sintering stress)

σ_{ij} corresponds to the externally applied stress. The ratio $\frac{\sigma(W)}{W}$ represents the generalized viscosity, which is a constitutive property of the fully dense material, and the term $\frac{\sigma(W)}{W}\left[\varphi\dot{\varepsilon}_{ij} + \left(\psi - \frac{1}{3}\varphi\right)\dot{e}\delta_{ij}\right]$ is the material resistance. The product $P_L\delta_{ij}$ is the sintering contribution due to thermodynamics driving force. If $\sigma_{ij}$is equal to zero Equation 2.13 describes free sintering while if the capillary stress P_L is equal to zero Equation 2.13 describes treatment by pressure without sintering. If both σ_{ij} and P_L are $\neq 0$ Equation 2.13 describes sintering under pressure. *σ(W)* is an arbitrary function of *W* that assumes a different form depending on the material behavior (linear viscous, plastic or subjected to a power-law creep).

The porosity *(θ)* may expressed as the ratio between the volume of pores (V_{pores}) and the total volume (V_{total}):

$$\theta = \frac{V_{pores}}{V_{total}} \qquad 2.14$$

Equation 2.13 has to be considered together with the continuity equation (mass conservation)

$$\dot{e} = \frac{\dot{\theta}}{1-\theta} \qquad 2.15$$

The effective properties of a heterophase material depend on the porosity, hence, as demonstrated by Skorohod with a stochastic approach:

$$W = \sqrt{\frac{\varphi\dot{\gamma}^2 + \psi e^2}{1-\theta}} \qquad 2.16$$

$$\varphi = (1-\theta)^2 \qquad 2.17$$

$$\psi = \frac{2}{3}\frac{(1-\theta)^3}{\theta} \qquad 2.18$$

$$P_L = \frac{3}{2}\frac{\gamma}{a}(1-\theta)^2 \qquad 2.19$$

where $\dot{\gamma}^2$ is the shape change rate and a the particle radius. Equation 2.13 describes the sintering behavior as a function of the material parameters such as viscosity and shear and bulk modulus. The effective Laplace pressure (sintering stress) is the driving force of the phenomenon and is the cooperative action of the local capillary stresses mediated over a macroscopic volume. The effect of the microstructure is introduced through the dependence of W, φ, ψ and P_L on the porosity. Hence, the macroscopic evolution of sintering is described considering microstructural characteristics. But the sintering kinetics depends not only on the properties of the powder particles and on their interactions, but also on macroscopic factors such as kinematic constrains, externally applied forces and inhomogeneity of properties in the volume. In this way, the model allows taking into account the friction between sintering body and the furnace surface or the gradient of green density introduced by prior compaction, as an example. This results in solving proper boundary problems.

Several authors investigated the anisotropy of dimensional changes in sintering using the continuum mechanics approach with different geometrical models of the green microstructure in terms of pore and grains. Some authors consider a two dimensional model [29, 50-52] while others a three dimensional model [32,53], [54] is based on a Monte Carlo simulation and [55] on a discrete element method. Olevsky [49] represents the compacted specimen as a body containing oriented ellipsoidal pores (Figure 2.6); anisotropy of shrinkage is the result of the anisotropy of the effective Laplace pressure (the sintering stress) and of viscosity.

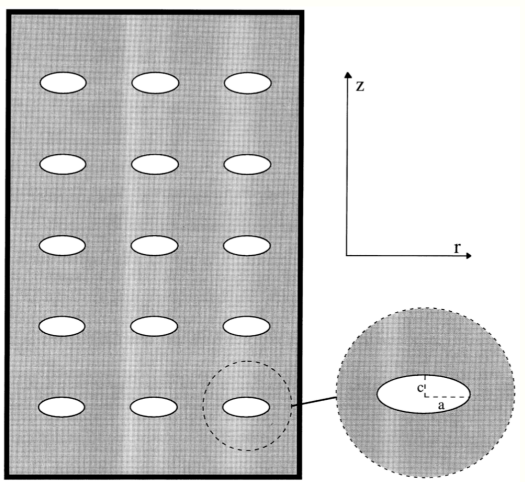

Figure 2.6 Anisotropic porous body (adapted from [49])

Wakai correlates the anisotropic sintering stress [31] and viscosity [32] and the resulting anisotropic shrinkage to the inhomogeneous packing of the particles and to their rearrangement during sintering [30]. An anisotropic constitutive law for sintering in presence of an anisotropic strain or an anisotropic stress field was proposed by Bordia et al. [28]. Zavaliangos *et al*. [29] model the microstructure of the green part as an ordered array of elliptical grains oriented with the mayor axis perpendicular to the compaction direction. Theoretical transversal shrinkage is higher than the longitudinal one, the difference depends on the grain boundary/surface diffusivity ratio. The discrepancy between such a prediction and the experimental observation that longitudinal shrinkage is usually larger than the transversal one was justified with the presence of contact micropores that shrink very fast on sintering, and with the fragmentation of the oxide layer caused by cold compaction that may enhance axial shrinkage.

2.3 REFERENCES

[1] H. Kuroki, Anisotropic springback and shrinkage of iron powder compact, Key Eng Mater. 29 (1989) 162-164.

[2] A. Vagnon, O. Lame, D. Bouvard, M. Di Michiel, D. Bellet, G. Kapelski, Deformation of steel powder compacts during sintering: correlation between macroscopic measurement and in situ microtomography analysis, Acta Mater. 54 (2006), 513-522.

[3] G.C. Kuczynski, Self-diffusion in sintering of metallic particles, AIME TRANS. 185 (1949) 169–178.

[4] R.M. German, Sintering theory and practice, Sinter. Theory Pract. Randall M Ger. Pp 568 ISBN 0-471-05786-X Wiley-VCH January 1996. 1 (1996).

[5] L. Kang, Sintering: Densification, Grain Growth and Microstructure, 2005, Oxford, Elsiever.

[6] R.L. Coble, Sintering Crystalline Solids. I. Intermediate and Final State Diffusion Models, J. Appl. Phys. 32 (1961) 787–792.

[7] F.V. Lenel, H.H. Hausner, I.A. El Shanshoury, J.G. Early, G.S. Ansel, The driving force for shrinkage in copper powder compacts during the early stages of sintering, Powder Metall. 5 (1962) 190–198.

[8] M.F. Ashby, A first report on sintering diagrams, Acta Metall. 22 (1974) 275– 289.

[9] F.V. Lenel, Powder metallurgy: principles and applications, Metal Powder Industry, 1980.

[10] F.B. Swinkels, M.F. Ashby, A second report on sintering diagrams, Acta Metall. 29 (1981) 259–281.

[11] K.S. Hwang, R.M. German, F.V. Lenel, Capillary forces

between spheres during agglomeration and liquid phase sintering, Metall. Trans. A. 18 (1987) 11–17.

[12] H.E. Exner, E. Arzt, Sintering Processes, in: S. Sōmiya, Y. Moriyoshi (Eds.), Sinter. Key Pap., Springer Netherlands, 1990: 157–184.

[13] C. Herring, Surface Tension as a Motivation for Sintering, in: P.J.M. Ball, P.D. Kinderlehrer, P.P. Podio-Guidugli, P.M. Slemrod (Eds.), Fundam. Contrib. Contin. Theory Evol. Phase Interfaces Solids, Springer Berlin Heidelberg, 1999: pp. 33–69.

[14] D. Lynn Johnson, New method of obtaining volume, grain-boundary and surface diffusion coefficients from sintering data, Journal of applied physics 40 (1969) 1

[15] R.M. German, Z.A. Munir, Surface area reduction during isothermal sintering, Journal of the American Ceramic Society 59 (1976) 379-383

[16] R.M. German, J.F. Lathrop, Simulation of spherical powder sintering by surface diffusion, Journal of materials science 13 (1078) 921-929

[17] W.S. Coblenz, J.M. Dynys, R.M. Cannon, R.L. Coble, Initial stage solid state sintering models. A critical analysis and assessment, Materials science research 13 (1980) 141-157

[18] K-S. Hwang, R.M. German, Analysis of initial stage sintering by computer simulation, Materials Science Research (1984) 35-47

[19] B.H. Alexander, R.W. Balluffi, The mechanism of sintering of copper, Acta Metall. 5 (1957) 666–677.

[20] H. Ichinose, G.C. Kuczynski, Role of grain boundaries in sintering, Acta Metall. 10 (1962) 209–213.

[21] H.E. Exner, P. Bross, Material transport rate and stress

distribution during grain boundary diffusion driven by surface tension, Acta Metall. 27 (1979) 1007–1012.

[22] G. C. Kuczynski, The mechanism of densification during sintering of metallic powders, Acta Metall. 4 (1956) 58-61

[23] E. Friedrich, W. Schatt, Sintering of One-Component Model Systems: Nucleation and Movement of Dislocations in Necks, Powder Metall. 23 (1980) 193–197.

[24] E. Friedrich, W. Schatt, High Temperature Plasticity on Solid Phase Sintering, Sci Sinter. 15 (1983) 63–71.

[25] W. Schatt, E. Friedrich, Dislocation-Activated Sintering Processes, in: G.C. Kuczynski, D.P. Uskoković, H.P. III, M.M. Ristić (Eds.), Sintering'85, Springer US, 1987: pp. 133–141.

[26] S.H. Hillman, R.M. German, Constant heating rate analysis of simultaneous sintering mechanisms in alumina, Journal of Materials Science 27 (1992) 2641-2648

[27] W. Luo, J. Pan, Effect of surface diffusion and heating rate on first stage sintering that densifies by grain-boundary diffusion, Journal of the American Ceramic Society 98 (2019) 3483-3489

[28] R.K. Bordia, R. Zuo, O. Guillon et al, Anisotropic constitutive laws for sintering bodies, Acta Mater. 54 (2006) 111–118.

[29] A. Zavaliangos, JM Missiaen, D. Bouvard, Anisotropy in shrinkage during sintering, Sci Sintering. 38 (2006) 13– 25.

[30] F. Wakai, K. Chihara, M. Yoshida, Anisotropic shrinkage due to particle rearrangement in sintering, Acta Mater. 55 (2007) 4553–4566.

[31] F. Wakai, Y. Shinoda, Anisotropic sintering stress for sintering of particles arranged in orthotropic symmetry, Acta Mater. 57 (2009) 3955–3964.

[32] F. Wakai, T. Akatsu, Anisotropic viscosities and shrinkage rate in sintering of particles in a simple orthorhombic structure, Acta Mater.58 (2010) 1921–1929.

[33] A. Molinari, C. Menapace, E. Torresani et al, Working hypothesis for origin of anisotropic sintering shrinkage caused by prior uniaxial cold compaction, Powder Metall. 56(3) (2013) 189–195.

[34] A. Molinari, E. Bisoffi, C. Menapace, et al, Shrinkage kinetics during early stage sintering of cold isostatically compacted iron powder, Powder Metall. 57(1) (2014) 61–69.

[35] A. Molinari, E. Torresani, C. Menapace, et al, The anisotropy of dimensional change on sintering of iron, J Am Ceram Soc. 98(11) (2015) 3431–3437.

[36] R. Smoluchowski, Theory of Grain Boundary Diffusion, Phys. Rev. 87 (1952) 482–487. doi:10.1103/PhysRev.87.482.

[37] Y. Shima, Y. Ishikawa, H. Nitta, Y. Yamazaki, K. Mimura, M. Isshiki, et al., Self-Diffusion along Dislocations in Ultra High Purity Iron, Mater. Trans. 43 (2002) 173–177.

[38] Y. Iijima, Diffusion in high-purity iron: Influence of magnetic transformation on diffusion, J. Phase Equilibria Diffus. 26 (2005) 466–471.

[39] E. Torresani, I. Cristofolini, A. Molinari, Study of the anisotropic microstructure of the uniaxially cold compacted green parts, Adv Powder Metall Part Mater. 3 (2015) 9–18.

[40] J. Frenkel, Viscous flow of crystalline bodies under the action of surface tension., J Phys USSR. 9 (1945) 385–391.

[41] J.K. Mackenzie, R. Shuttleworth, A Phenomenological Theory of Sintering, Proc. Phys. Soc. Sect. B. 62 (1949) 833.

[42] V. V. Skorohod, Rheological basis of the theory of sintering, Naukova Dumka, Kiev, 1972

[43] C.L.D. H. A. Kuhn, Deformation Characteristics and Plasticity Theory of Sintered Powder Metals, Int J Powder Mat. 7 (1971).

[44] R.J. Green, A plasticity theory for porous solids, Int. J. Mech. Sci. 14 (1972) 215–224.

[45] S. Shima, M. Oyane, Plasticity theory for porous metals, Int. J. Mech. Sci. 18 (1976) 285–291.

[46] V.V. Skorokhod, M.B. Shtern, I.F. Martynova, Theory of nonlinearly viscous and plastic behavior of porous materials, Sov. Powder Metall. Met. Ceram. 26 (1987) 621–626.

[47] D.S. Wilkinson, M.F. Ashby, Pressure sintering by power law creep, Acta Metall. 23 (1975) 1277–1285.

[48] J.M. Duva, A constitutive description of nonlinear materials containing voids, Mech. Mater. 5 (1986) 137–144.

[49] E.A. Olevsky, Theory of sintering: from discrete to continuum, Mater. Sci. Eng. R Rep. 23 (1998) 41–100.

[50] W.R. Cannon, P.M. Raj, Evolution of Sintering Anisotropy Using a 2D Finite Difference Method, J. Am. Ceram. Soc. 92 (2009) 1391–1395.

[51] P.M. Raj, A. Odulena, W.R. Cannon, Anisotropic shrinkage during sintering of particle-oriented systems—numerical simulation and experimental studies, Acta Mater. 50 (2002) 2559–2570.

[52] E.A. Olevsky, B. Kushnarev, A. Maximenko, V. Tikare, M. Braginsky, Modelling of anisotropic sintering in crystalline ceramics, Philos. Mag. 85 (2005) 2123–2146.

[53] F. Li, J. Pan, O. Guillon, A. Cocks, Predicting sintering deformation of ceramic film constrained by rigid substrate using anisotropic constitutive law, Acta Mater. 58 (2010) 5980–5988.

[54] V. Tikare, M. Braginsky, E. Olevsky, D.L. Johnson, Numerical Simulation of Anisotropic Shrinkage in a 2D Compact of Elongated Particles, J. Am. Ceram. Soc. 88 (2005) 59–65.

[55] A. Wonisch, O. Guillon, T. Kraft, M. Moseler, H. Riedel, J. Rödel, Stress- induced anisotropy of sintering alumina: Discrete element modelling and experiments, Acta Mater. 55 (2007) 5187–5199.

3. EXPERIMENTAL PROCEDURE

3.1 CHARACTERIZATION OF THE POWDERS

3.1.1 MORPHOLOGY OF THE POWDER PARTICLES

The morphology of the powder particles has been observed through images taken using a Scanning Electron Microscope (SEM) with magnification from 100X to 2500X. Sample preparation is not required, powder particles have been simply stuck on the sample holder. Figure 3.1 shows some examples.

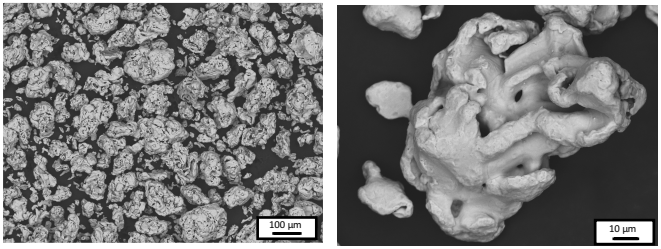

Figure 3.1 SEM images at 100X and 1000X of a sponge iron powder (NC 100.24)

Low magnifications allow a general view of the powder, while high magnifications are suitable to observe the particle morphology.

3.1.2 PARTICLE SIZE DISTRIBUTION

The particle size distribution was obtained thanks to a Malvern Pananalytical Mastersizer 2000 laser diffraction particle analyzer. The powders (without lubricant) were dispersed in a solvent by ultrasounds. An example of a differential and a cumulative curve is represented in Figure 3.2.

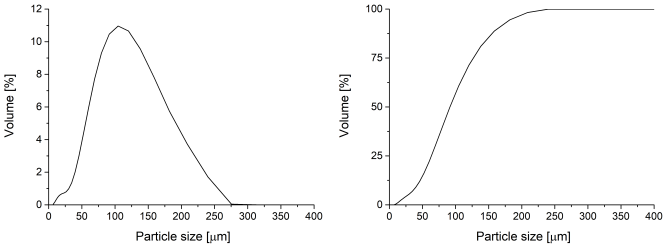

Figure 3.2 Particle size distribution: differential and cumulative curve relative to a sponge iron powder (NC 100.24)

3.1.3 SPECIFIC SURFACE AREA

The specific surface area of the powder particles has been assessed through gas adsorption, according to the IUPAC technical reports [1-2].

The adsorption is the enrichment of molecules, atoms or ions near an interface. If the system is solid/gas, adsorption happens close to the solid surface and outside the solid structure. The adsorbate is the material in the adsorbed state, while the adsorptive is the same component in the fluid phase, therefore it is the adsorbable gas. The solid on which surface the adsorption occurs is the adsorbent. The adsorption space is the space occupied by the adsorbate. There are two kinds of adsorption: physical (physisorption) or chemical (chemisorption). The former occurs whenever an adsorptive is brought into contact with the surface of a solid and the forces involved are the same that are responsible for

the imperfection of real gases, the latter involves intermolecular forces that lead to the formation of chemical bonds. The term adsorption refers to the onward process while desorption denotes the converse process. Adsorption hysteresis arises when the adsorption and desorption curves are not overlapped. The aim is to determine the adsorption isotherm, which is the relation between the amount adsorbed n^a and the equilibrium pressure of the gas at a constant temperature. When a quantity n of gas is introduced, the system is composed by the solid (adsorbent), the gas (adsorptive) and the adsorption space V^a, which is the volume occupied by n^a. The estimation of n^a depends on V^a, that is unknown. Gibbs model allows the assessment of an intermediate quantity, the surface excess amount n^σ, under the following hypothesis:

- Bidimensional adsorption, hence $V^a = 0$
- Adsorption over an imaginary surface (Gibbs Dividing Surface, GDS) that limits the volume available for the gas phase (V^g)

The amount of gas n^g in equilibrium with the adsorbent may be calculated thanks to the gas laws.

$$n^\sigma = n - n^g \qquad 3.1$$

n^σ is the quantity measured experimentally. In case of adsorption of vapors under 0,1 MPa n^σ coincides with n^a, since GDS is very close to the adsorbent surface. For adsorption measurements at higher pressures n^σ has to be converted into the corresponding n^a. In the simplest case, when GDS coincides with the actual adsorbing surface [3], n^a is given by

$$n^a = n^\sigma + c^g V^a \qquad 3.2$$

The surface of a solid may be defined at different levels:

- The Van der Waals surface, at atomic scale, is formed by the external part of the Van der Waals spheres of the atoms of the surface
- The Connolly surface is traced by the bottom of a spherical probe molecule rolling over the Van der Waal surface
- The r-distance surface is at a distance r from the Connolly surface.

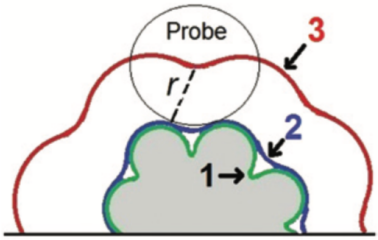

Figure 3.3 Surface of a solid: 1- van der Waals, 2- Connolly, probe-accessible, 3- accessible r-distance (adapted from [2])

The Connolly surface is the probe accessible surface and it is that measured through physisorption.

3.1.3.1 ACQUISITION OF THE PHYSISORPTION ISOTHERMS

The physisorption isotherms have been obtained by means of a static manometric method with Nitrogen at 77 K and pressure below 1 bar as probe gas. The sample, which is the adsorbent, lays into a confined, calibrated volume maintained at constant temperature. The first step is the removal of the physisorbed species from its surface through controlled outgassing at high temperature. Then, a dosed quantity of gas is admitted and, as the adsorption takes

place, the pressure falls until an equilibrium is reached. The amount of gas adsorbed at the equilibrium pressure is the difference between the amount of gas admitted and the amount of gas required to fill the space around the adsorbent, which is the dead space. This process is repeated in order to construct the curve point by point. The knowledge of the dead space is crucial. It may be determined by subtracting the volume of the adsorbent from the confined volume obtained through a pre-calibration. Figure 3.4 shows an example of physisorption curve.

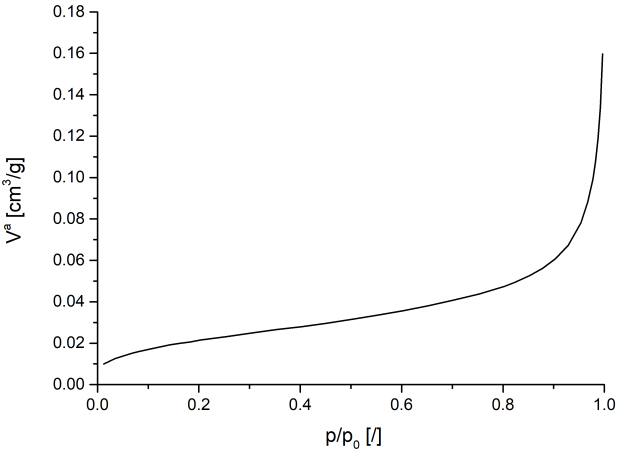

Figure 3.4 Physisorption isotherm relative to a sponge iron powder (NC 100.24)

The physisorption isotherms are classified according to IUPAC recommendations.

3.1.3.2 ASSESSMENT OF THE SURFACE AREA

The specific surface area may be determined through the Brunauer-Emmett-Teller (BET) method [4-5]. To be precise, what calculated is the probe accessible area which is the effective area available for the adsorption of the specific adsorptive. The method consists in two steps:

- Transformation of the physisorption isotherm into a "BET-plot" in order to determine the BET monolayer capacity n^m
- Calculation of the BET area from n^m, knowing the molecular cross-sectional area σ occupied by the adsorbate molecule in the complete monolayer

The BET-plot is amount adsorbed vs relative pressure and in Figure 3.5 is reported an example.

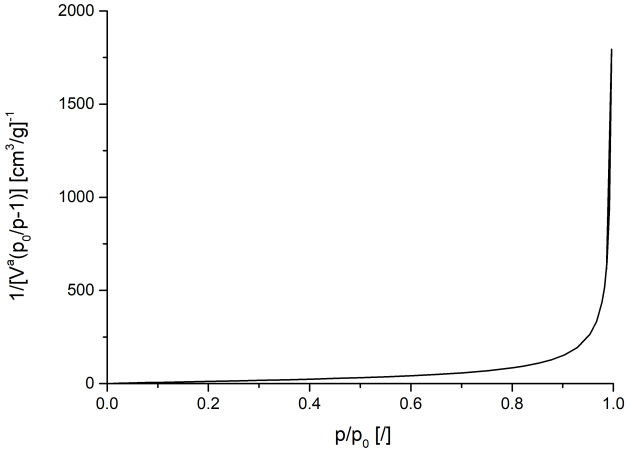

Figure 3.5 BET plot relative to a sponge iron powder (NC 100.24)

n^m is the amount of gas adsorbed sufficient to cover the surface with a complete monolayer of molecules. To calculate it, the linear relation between $p/[n^a(p_0-p)]$ and p/p_0 when p/p_0 is within 0.05 and 0.3 may be exploited. The BET equation is applied in the linear form (Equation 3.3)

$$\frac{p}{n^a\,(p_0-p)} = \frac{1}{n^m C} + \frac{C-1}{n^m C}\left(\frac{p}{p_0}\right) \qquad 3.3$$

The parameter C is exponentially related to the energy of monolayer adsorption. If it is at least 80, the knee of the

isotherm is sharp and the point corresponding to the physisorption over a monolayer is well defined. Once gained n^m, the BET specific area $a_s(BET)$ may be calculated through Equation 3.4.

$$a_s(BET) = \frac{n^m \, L \, \sigma}{m} \qquad 3.4$$

L is the Avogadro constant, σ is the molecular cross-sectional area and m the mass of the adsorbent (sample). In case of Nitrogen, the product $L\sigma$ is 4.35.

3.2 PRODUCTION OF THE GREEN PARTS

By means of uniaxial cold compaction with a laboratory manual press, cylindrical samples with both diameter and height 6 mm have been produced.
The materials considered were:

- Atomized iron powder ASC 100.29 batch I with 0.8%wt LubeE $\rightarrow$ ASC I
- Atomized iron powder ASC 100.29 batch II with 0.8%wt LubeE $\rightarrow$ ASC II
- Sponge iron powder NC 100.24 with 0.8%wt LubeE $\rightarrow$ NC
- Austenitic stainless steel AISI 316L particle size ϕ < 45 μm with 1%wt Amidewax
- Austenitic stainless steel AISI 316L ϕ > 90 μm with 1%wt Amidewax

Concerning the green density:

- ASC I: 6.5 g/cm^3, 6.7 g/cm^3, 6.9 g/cm^3, 7.1 g/cm^3 and 7.3 g/cm^3

- ASC II: 6.5 g/cm^3, 6.9 g/cm^3 and 7.3 g/cm^3
- NC: 6.9 g/cm^3
- Austenitic stainless steel AISI 316L ϕ < 45 μm: 6.2 g/cm^3, 6.4 g/cm^3 and 6.6 g/cm^3
- Austenitic stainless steel AISI 316L ϕ > 90 μm: 6.2 g/cm^3, 6.4 g/cm^3 and 6.6 g/cm^3

The corresponding compacting pressures were gained from the curves of the density vs applied pressure shown in Figure 3.6 in case of iron powders and in Figure 3.7 in case of stainless steel powders.

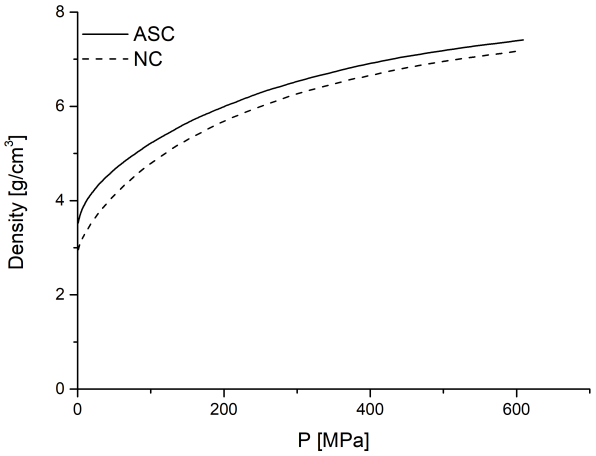

Figure 3.6 Iron: density vs applied pressure

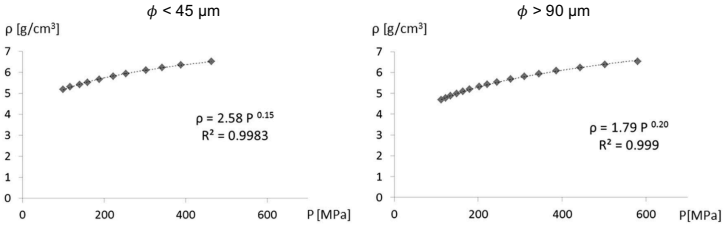

Figure 3.7 AISI 316L: density vs applied pressure in case of ϕ < 45 μm (left) and ϕ > 90 μm (right) (adapted from [6])

3.3 MICROSTRUCTURAL CHARACTERIZATION OF THE GREEN PART

The microstructural characterization has been carried out on the following green samples:

-ASC I: samples at density 6.5 g/cm^3, 6.9 g/cm^3 and 7.3 g/cm^3
-NC sample at density 6.9 g/cm^3
-AISI 316L ϕ < 45 μm sample at green density 6.5 g/cm^3
-AISI 316L ϕ > 90 μm sample at green density 6.5 g/cm^3

The cylindrical samples were cut along the longitudinal direction and mounted in a cold cured epoxy resin to allow the metallographic preparation. An initial grinding was necessary to remove the superficial layer of resin and make the surface smooth. To this purpose a set of silica carbide papers (sandpaper) was used. To observe the real structure of the material the porosity should be opened using nylon polishing cloths and the following abrasives:

- 3 μm diamond paste
- 1 μm diamond paste

In the end, a slight etching with Nital 2% helped to highlight the contact zones between the powder particles. During these steps the samples were handled gently to avoid the detachment of the powder particles. Images of the material structure were taken using a SEM (ASC I and NC) or an Optical Microscope (OM) (AISI 316L) with a magnification between 200X and 400X, the vertical direction in the micrographs corresponds to the longitudinal direction of the samples, which is the direction parallel to compaction. The contact lengths between the powder particles, which are the diameters of the contact areas assumed circular, were

measured by means of an open source image analysis software: ImageJ®.

3.3.1 MEASUREMENT OF THE INTERNAL RADIUS OF THE NECK

Figure 3.8 shows, in sake of example, the microstructure of an ASC sample at 6.9 g/cm^3 green density:

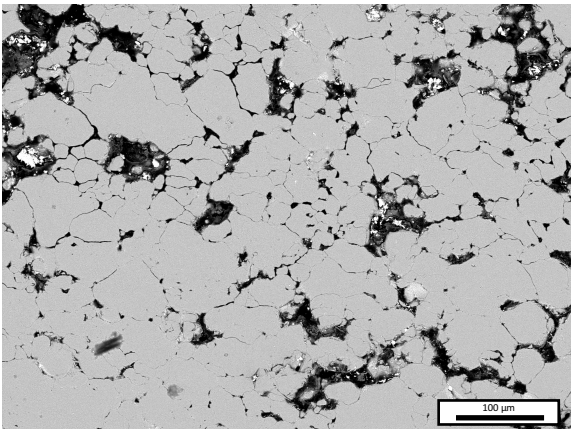

Figure 3.8 Microstructure of a 6.9 g/cm^3 green density sample (ASC)

With respect to the compaction direction, which is the vertical direction in the micrographs, we may distinguish three kinds of contacts (Figure 3.9):

- longitudinal $2X_L$: perpendicular to the compaction direction, they only contribute to the longitudinal shrinkage
- transversal $2X_T$: parallel to the compaction direction, they only contribute to the transversal shrinkage
- inclined $2X_I$: inclined to the compaction direction, they contribute both to the longitudinal and the transversal shrinkage in a quantity that depend on their orientation

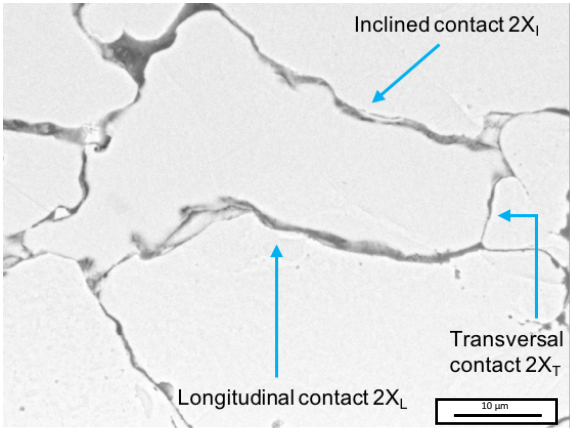

Figure 3.9 Longitudinal ($2X_L$), transversal ($2X_T$) and inclined ($2X_I$) contacts

Since the shrinkage kinetic model proposed assumes that each particle has two longitudinal contacts and four transversal contacts, the inclined contacts were decomposed into the two main directions by means of simple trigonometric relationships (Equation 3.5 and 3.6).

$$2X_L = 2X_I \sin\beta \qquad 3.5$$

$$2X_T = 2X_I \cos\beta \qquad 3.6$$

β is the angle between the contact and the longitudinal direction. The contact length measured corresponds to the internal diameter of the neck at the green state $2X_{0,\,green}$. Fifty particles were taken into account and the distribution of the lengths of the longitudinal contacts $2X_L$ and of the transversal contacts $2X_T$ were determined. The median of the distributions was taken as representative of the internal neck diameter along the two main directions and the corresponding radii may be easily calculated. The metallographic plane intersects the powder particles and the

contact areas at a statistically variable distance from the centers and with a statistically variable inclination respect to the vertical and horizontal directions. The result is that the contact lengths measured have to be corrected by means of a proper coefficient to obtain the actual dimensions.

3.3.1.1 CORRECTION COEFFICIENT

To determine the correction coefficient for the contact lengths, a bcc cluster of spherical particles extracted from a uniaxially cold compacted specimen was considered. The particles are partially overlapped to simulate that they are in contact over a surface (Figure 3.10). The anisotropic deformation of the green part has been introduced through a closer packing along the vertical direction than in the horizontal direction. Different ratios between the diameter of the contact area and the particle size allow the account for the different packing conditions and so different green density.

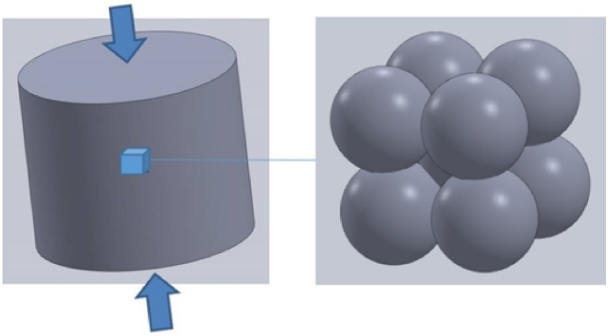

Figure 3.10 Bcc cluster of powder particles extracted from a cold compacted specimen (adapted from [7])

Assuming that the vertical direction is that of cold compaction, the cluster was sectioned by planes (Figure 3.11):

- Translated respect to the plane passing through the centers of the particles
- Rotated around the vertical axes
- Both translated and rotated

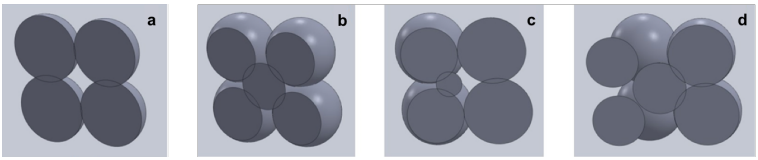

Figure 3.11 Longitudinal section through the centers (a), translated longitudinal section (b), rotated around the vertical axes longitudinal section (c) and translated and rotated longitudinal section (d)

No rotation along the horizontal axes has been considered, since the metallographic specimens were cut longitudinally. The length of the segments representing the diameters of the contact areas was determined in an analytical way and, in addition, diameters were measured on the sections for some combinations of translation and rotation. The ratio between the diameter of the interparticle area on the sections and the actual diameter are plotted as a function of the normalized translation distance and of the rotation angle (Figure 3.12) for longitudinal, transversal and inclined contacts (Figure 3.13):

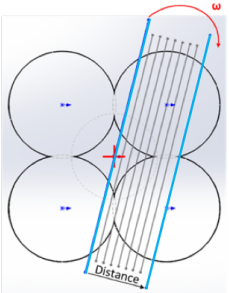

Figure 3.12 Translation distance and rotation angle (adapted from [7])

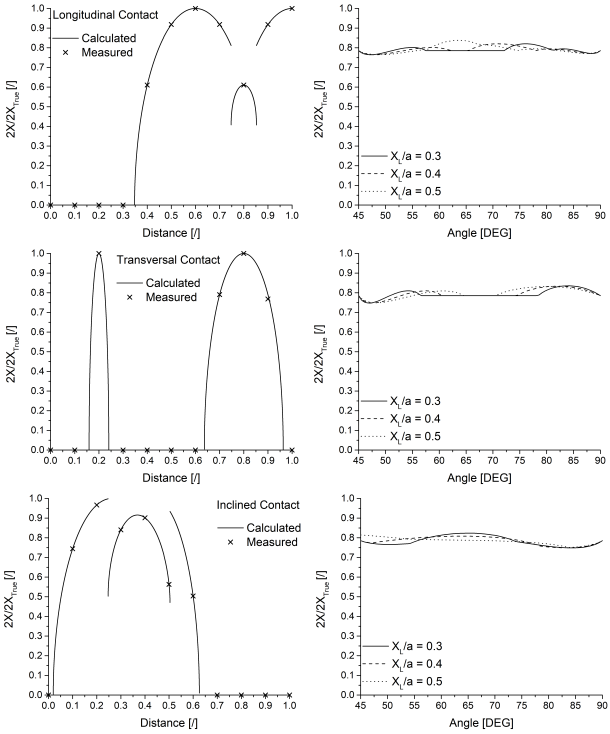

Figure 3.13 Ratio between the diameter on the sections and the actual diameter of the contact area as a function of the relative distance and as a function of the rotation angle for longitudinal, transversal and inclined contacts. a is the radius of the powder particles (adapted from [7])

The rotation of the intersection plane causes an almost constant underestimation of the contact lengths, while the translation distance strongly affects $2X/2X_{True}$. The mean value between the measured and real diameters is 0.79, hence the contact length measured by means of image analysis were corrected accordingly.

3.4 MEASUREMENT OF THE DIMENSIONAL CHANGES

In order to measure the dimensional changes in sintering and evaluate their anisotropy, the specimens were delubed and subjected to dilatometry tests.

3.4.1 DELUBRICATION

The delubrication conditions have been chosen depending on the material. Ferrous samples were delubed in a laboratory furnace at 550 °C in Argon/Hydrogen atmosphere. Both the heating and the cooling rate was 4.5 °C/min and the temperature was kept constant for one hour. Stainless steel samples were delubed in an industrial furnace at 600 °C Argon/Hydrogen atmosphere.

3.4.2 DILATOMETRY TESTS

The dimensional variations in sintering were determined using a Linseis L75 Platinum Series dilatometer. The measuring system, composed by a tube closed at one end and a push rod, is in alumina (Figure 3.14).

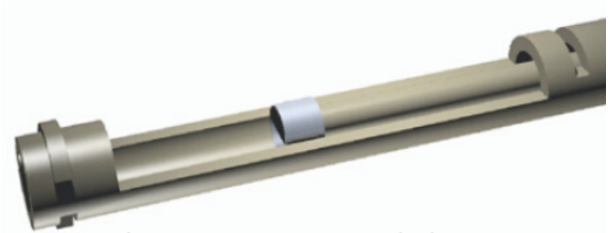

Figure 3.14 Schematic representation of the measuring system: tube and push rod

The sample is inside the tube, leaning on the closing surface and in contact with the push rod which is attached to the linear variable differential transformer (LVDT). The thermocouple is in contact with the sample. Once that the sample and the thermocouple have been positioned, the measuring system is put inside the furnace. A proper sample holder, a sort of tube with two pistons, allows the test on the loose powders.
Half of the specimens were tested in the longitudinal direction (variations of the height), half were tested in the transversal direction (variations of the diameter) to evaluate the anisotropy of the dimensional variations.

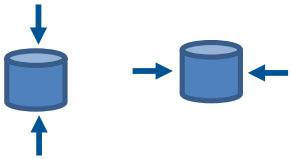

Figure 3.15 Longitudinal and transversal tests

Tests on iron specimens (ASC I and NC) were carried out in Argon backfilling (static atmosphere) and the thermal cycle was:

1- Heating (rate 10 °C/min) from RT to 1100 °C
2- Heating (rate 1 °C/min) from 1100 °C to 1120 °C (sintering temperature)
3- Isothermal holding (60 min)
4- Cooling (rate 10 °C/min) from 1120 °C to RT

For the specimens ASC II, the heating rate was between 5 °C/min and 30 °C/min. In case of AISI 316L the tests were carried out in Argon/Hydrogen flow and the thermal cycle was:

1- Heating (rate 10 °C/min) from RT to 1240 °C

2- Heating (rate 1 °C/min) from 1240 °C to 1250 °C (sintering temperature)
3- Isothermal holding (60 min)
4- Cooling (rate 10 °C/min) from 1250 °C to RT

3.5 REFERENCES

[1] K. S. W. Sing, D. H. Everett, R. A. W. Haul, L. Moscou, R. A. Pieroti, J. Rouquerol, T. Siemieniewska, Reporting physisorption data for gas/solid systems with special reference to the determination of surface area and porosity, Pure Appl. Chem. 57(4) (1985) 603-619.

[2] M. Thommes, K. Kaneko, A. V. Neimark, J.P.Olivier, F. Rodriguez-Reinoso, J. Rouquerol K. S. W. Sing, Physisorption of gases, with special reference to the evaluation of surface area and pore size distribution (IUPAC Technical Report), Pure Appl. Chem. 87 (9-19) (2015) 1051-1069.

[3] J. Rouquerol, F. Rouquerol, K. S. W. Sing, P. Llewellyn, G. Maurin, Adsorption by Powders and Porous Solids: Principles, Methodology and Applications, Academic Press (2014).

[4] S. Brunauer, P.H. Emmett, E. Teller, Adsorption of gases in multimolecolar layers, J. Am. Chem. Soc. 60(2) (1938) 309-319.

.

[5] S. Lowell, J. Shields, M. A. Thomas, M. Thommes, Characterization of Porous Solids and Powders: Surface Area, Porosity and Density, Springer, 2004.

[6] I. Cristofolini, G. Pederzini, A. Rambelli, A. Molinari, Densification and deformation during uniaxial cold

compaction of stainless steel powder with different particle size, Powder Metall. 59 (1) (2016) 73-84

[7] S. Baselli, E. Torresani, M. Zago, I. Cristofolini, A. Molinari, Sintering shrinkage of uniaxial cold compacted iron. Part 2: Influence of the microstructure on the anisothermal and isothermal shrinkage of uniaxial cold compacted iron, Powder Metall. 61(4) (2018) 276-284.

4. KINETIC MODEL FOR THE ISOTHERMAL SHRINKAGE

In the classical theory of sintering the powder particles are assumed to be rigid spheres in contact on a point, hence the geometrical modifications due to the deformation of the powder particles during cold compaction are totally neglected [1-2]. The shrinkage kinetic equation which derives from these hypothesis is the following:

$$\frac{\Delta l}{l_0} = K t^n \qquad 4.1$$

The parameters *K* and *n* are function of the mass transport mechanism responsible for shrinkage. In case of volume diffusion $K = \left(\frac{80\, D_a\, \gamma\, \Omega}{2^5\, k\, T\, (2a)^3}\right)^{0.4}$ and $n = 0.4$. D_a is the diffusion coefficient, γ the surface tension, Ω the atomic volume, *k* the Boltzmann constant, *T* the absolute temperature and *a* the radius of the powder particles. The model shown in Figure 4.1 allows the consideration of the deformation of the particles.

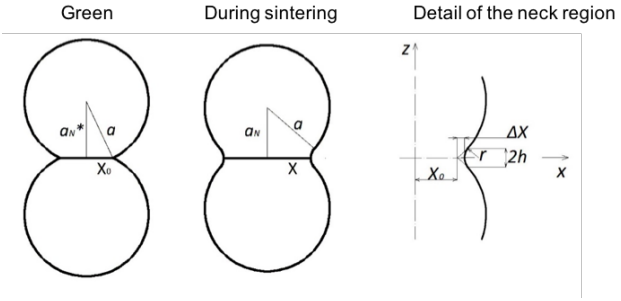

Figure 4.1 Geometrical model of prior cold compacted particles and its evolution during sintering (adapted from [3])

In the green part, because of the deformation occurred during cold compaction, two powder particles with the same radius *a* are in contact over a surface. This area is circular and characterized by the radius X_0. a_N* is the half distance between the centres of the particles and is related to the particle radius and to X_0 through Equation 4.2

$$a_N^* = \sqrt{(a^2 - X_0^2)} \qquad 4.2$$

During sintering the internal radius of the neck increases by the quantity ΔX and its length X is correlated to X_0 by Equation 4.3

$$X = X_0 + \Delta X \qquad 4.3$$

The half-height *h* of the neck is correlated to the decrease of the distance between the centres of the particles by Equation 4.4

$$h = a_N^* - a_N \qquad 4.4$$

The flux of atoms from the grain boundary of the neck, which corresponds to the contact area, to the external surface of the neck through the area of the neck A_N leads to the

increase in the volume of the neck V_N which causes the sintering shrinkage. The dependence of h, V_N, A_N and the external radius of the neck r from X_0, ΔX and a may be calculated from the geometrical relations in the region of the neck, as described in the paragraph 4.1.

4.1 THE GEOMETRICAL RELATIONS IN THE NECK REGION

The geometrical model of two particles in contact over a circular surface and a detail of the neck region are represented in Figure 4.2.

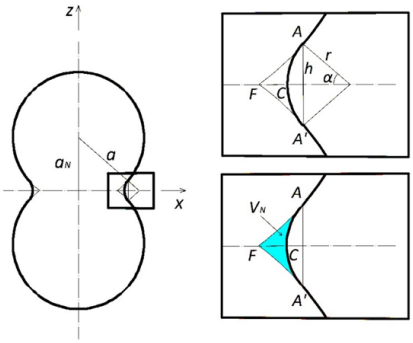

Figure 4.2 Detail of the neck region (adapted from [3])

The neck volume V_N is the difference between the volume V_T and the volume V_S. The former is the volume of the solid generated by the rotation of the geometrical figure AA'F (AF and A'F are approximated by straight segments) around the z axis while the latter is the volume of the solid generated by the rotation of the geometrical figure AA'C around the same axis. Both V_T and V_S are calculated through the Pappo-Guldino theorem.

$$V_T = h\left[X + r - r\ \cos\alpha - \sqrt{(a^2 - a_n^2)}\right]\left\{\sqrt{(a^2 - a_n^2)} + \frac{2}{3}\left[X + r\ (1 - \cos\alpha) - \sqrt{(a^2 - a_n^2)}\right]\right\} 2\pi \quad 4.5$$

$$V_S = [\alpha\, r^2 - h\, r\ \cos\alpha]\left[X + r - \frac{2\, r\ (\sin\alpha)^3}{3\ (\alpha - \sin\alpha\cos\alpha)}\right] 2\pi \quad 4.6$$

The neck volume V_N is

$$V_N = 2\pi\left\{h\ \left[X + r - r\ \cos\alpha - \sqrt{(a^2 - a_n^2)}\right]\left\{\sqrt{(a^2 - a_n^2)} + \frac{2}{3}\left[X + r\ (1 - \cos\alpha) - \sqrt{(a^2 - a_n^2)}\right]\right\} - [\alpha\, r^2 - h\, r\ \cos\alpha]\left[X + r - \frac{2\, r\ (\sin\alpha)^3}{3\ (\alpha - \sin\alpha\cos\alpha)}\right]\right\} \quad 4.7$$

The neck area A_N is given by Equation 4.8

$$A_N = 2r\ \alpha\ \left[X + r - \frac{r\ \sin\alpha}{\alpha}\right] 2\pi \quad 4.8$$

The external curvature radius r of the neck is given by Equation 4.9

$$r = \frac{X^2 - a^2 + a_N^2}{2\ (a - X)} = \frac{X^2 - a^2 + (a_{N^*} - h)^2}{2\ (a - X)} \quad 4.9$$

Since

$$sin\,\alpha = \frac{a_N}{a + r} = \frac{a_{N^*} - h}{a + r} \quad 4.10$$

$$sin\,\alpha = \frac{h}{r} \quad 4.11$$

r and h result from the solution of the system given by Equations 4.9 and 4.12

$$\frac{a_N^* - h}{a + r} = \frac{h}{r} \qquad 4.12$$

The above equations may be used to calculate the volume, the area, the half-height and the external curvature radius of the neck as a function of the increase of the internal neck radius, for any value of X_0 and a. In Figure 4.3 are reported, in sake of example, the mentioned parameters as a function of ΔX and X_0 when the particle radius is 50 μm.

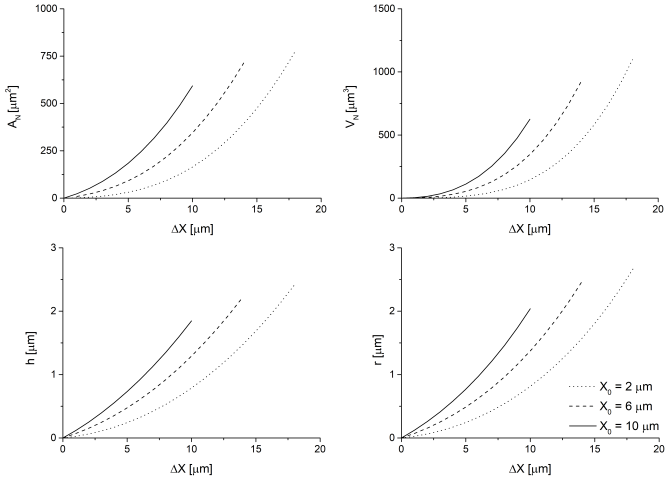

Figure 4.3 Area, volume, half-height and external radius of the neck as a function of ΔX for different X_0 from 2 μm to 10 μm in case of a = 50 μm (adapted from [3])

V_N, A_N, h and r increase with ΔX. In addition, for a constant neck growth ΔX, all the parameters increase on increasing the initial contact area between the powder particles. The external neck radius r determines the driving force of sintering, since $\Delta G = \gamma / r$ (γ is the surface tension). When ΔX is 0, therefore in the green state, r is independent from X_0

and so from the initial interparticle contact area. This means that the sintering driving force for uniaxially cold compacted parts is isotropic, since *r* is reasonably close to zero in the green state. This result confirms what was assumed in [4].
The Equations 4.7, 4.8, 4.9 and 4.12 are too complex to be introduced in an analytical shrinkage kinetic equation, so the curves of Figure 4.3 have been approximated by a power law. Figure 4.4 shows *h* vs ΔX, as an example:

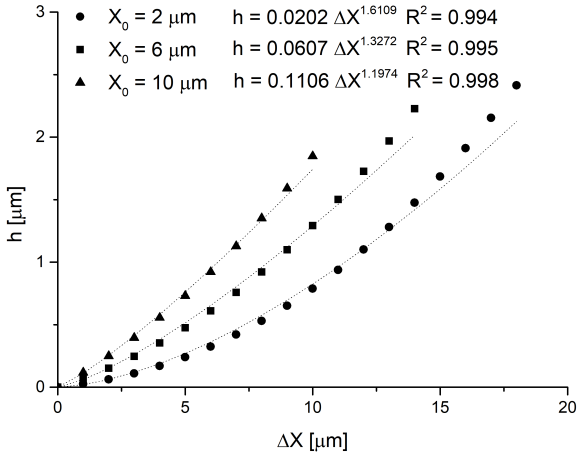

Figure 4.4 *h* as a function of ΔX for different X_0 (a = 50 μm) (adapted from [3])

The parameters *b* and *c* in the fitting Equation 4.13

$$h = b\,\Delta X^{c} \qquad 4.13$$

depend on X_0, as shown in Figure 4.5 relevant to a = 50 μm.

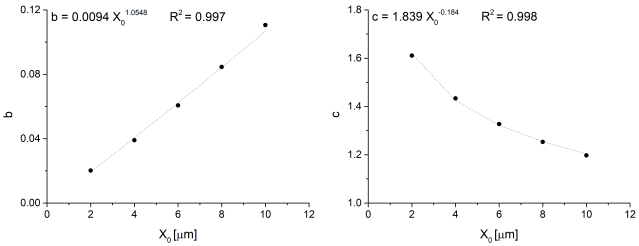

Figure 4.5 *b* and *c* as a function of X_0 (adapted from [3])

Such a dependence is expressed by the Equations 4.14 and 4.15

$$b = d\, X_0^e \qquad 4.14$$

$$c = f\, X_0^g \qquad 4.15$$

d and *f* depend on *a*, while *e* and *g* are constant as highlighted by Figure 4.6.

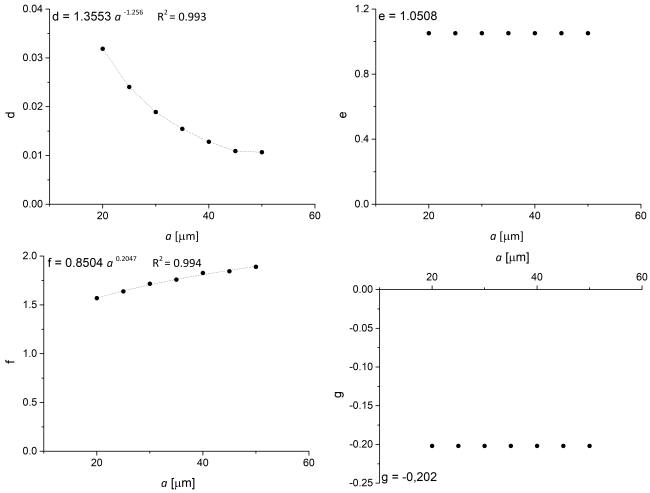

Figure 4.6 The parameters of Equation 4.14 and 4.15 as a function of the particle radius *a* (adapted from [3])

Combining all the correlations, the final equation giving the dependence of *h* on *a* and X_0 is

$$h = 1.3553\, a^{-1.256}\, X_0^{1.0508} \Delta X^{0.8504\, a^{0.2047} X_0^{-0.202}} = B\Delta X^n \quad 4.16$$

With the same procedure, Equation 4.17, 4.18 and 4.19 were obtained for V_N, A_N and *r*, respectively

$$V_N = 41.407\, a^{-1.822}\, X_0^{0.7467\, a^{0.247}}\ \Delta X^{1.7558\, a^{0.1792}\ X_0^{-0.19}} = C\Delta X^p \quad 4.17$$

$$A_N = 479.15\, a^{-1.943}\, X_0^{0.7124\, a^{0.2555}}\ \Delta X^{0.9305\, a^{0.2907}\ X_0^{-0.31}} = D\Delta X^q \quad 4.18$$

$$r = 2.0268\, a^{-1.384}\, X_0^{1.0789}\, \Delta X^{0.8698\, a^{0.2044}\, X_0^{-0.201}} = A\Delta X^k \quad 4.19$$

The linear shrinkage between the two particles in Figure 4.1 is correlated to *h* by Equation 4.20

$$\frac{\Delta l}{l_0} = \frac{a_n - a_n^*}{a_n^*} = \frac{(a_n^* - h) - a_n^*}{a_n^*} = -\frac{h}{a_n^*} = -\frac{h}{\sqrt{(a^2 - X_0^2)}} \quad 4.20$$

Combining Equation 4.20 and 4.16, the dependence of the linear shrinkage between two particles on the neck growth ΔX, on the particle size *a* and on the initial radius of the contact area X_0 is expressed by Equation 4.21

$$\frac{\Delta l}{l_0} = -\frac{B\Delta X^n}{\sqrt{(a^2 - X_0^2)}} \quad 4.21$$

Figure 4.7 shows the linear shrinkage between the two particles as a function of ΔX and X_0 for a constant particle

size a (left) and as a function of ΔX and a for a constant X_0 (right).

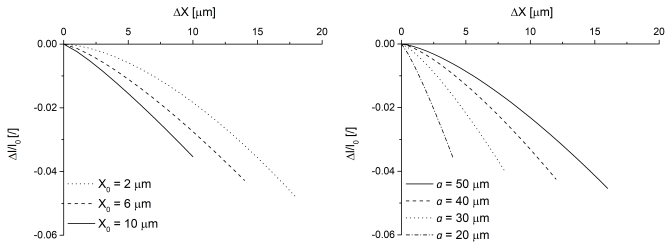

Figure 4.7 Linear shrinkage as a function of ΔX and X_0 for a constant particle size (left) and as a function of ΔX and a for a constant X_0 (right) (adapted from [3])

The linear shrinkage is increased by the increase of X_0 and the decrease of a because of geometrical reasons.

4.2 THE SHRINKAGE KINETIC EQUATION

The increase in the neck volume per time unit is equal to the flux of atoms to the neck surface

$$\frac{dV_N}{dt} = -JA_N\Omega \qquad 4.22$$

The atomic flux is given by

$$J = -D_v \frac{\partial C}{\partial X} \approx -D_v \frac{\Delta C}{\Delta X} \qquad 4.23$$

where D_v is the vacancy diffusivity and $\Delta C/\Delta X$ is the gradient of vacancies concentration C along distance ΔX. Since it was demonstrated that, in cold compacted green parts, the structural defectiveness in the deformed contact regions enhances the mass transport through the lattice [5-7] thanks to the dislocation pipe diffusion [8], the equation is

developed for volume diffusivity as transport mechanism responsible for sintering. Introducing

$$\Delta C \approx \frac{\gamma C_0 \Omega}{kTr} \qquad 4.24$$

where γ is the surface tension, C_0 is the equilibrium concentration of vacancies, Ω is the atomic volume, k the Boltzmann constant, T the absolute temperature and r the external radius of the neck surface, Equation 4.22 may be integrated as

$$\int_0^{\Delta\bar{X}} \Delta X^{p-t+k}\, d(\Delta X) = \int_0^t D_v \frac{\gamma C_0 \Omega^2}{kT} \frac{D}{ACp}\, dt \qquad 4.25$$

and analytically solved in

$$\Delta X = \left[D_v \frac{\gamma C_0 \Omega^2}{k T} \frac{D\,(p-q+k+1)}{A\,C\,p}\, t \right]^{\frac{1}{(p-q+k+1)}} \qquad 4.26$$

Combining Equation 4.21 with Equation 4.26 the shrinkage kinetic equation 4.27 is obtained

$$\frac{\Delta l}{l_0} = -\frac{B}{a_N^*} \left[D_v \frac{\gamma C_0 \Omega^2}{k T} \frac{D\,(p-q+k+1)}{A\,C\,p}\, t \right]^{\frac{n}{(p-q+k+1)}} \qquad 4.27$$

That may be modified as Equation 4.28 introducing the bulk diffusivity $D_a=D_vC_0\Omega$:

$$\frac{\Delta l}{l_0} = -\frac{B}{a_N^*} \left[D_a \frac{\gamma \Omega}{k T} \frac{D\,(p-t+k+1)}{A\,C\,p}\, t \right]^{\frac{n}{(p-t+k+1)}} \qquad 4.28$$

All the parameters resulting from the geometrical relationships may be grouped in the parameters G and e

$$G = \frac{B}{a_N^*} \left[\frac{D\,(p-q+k+1)}{A\,C\,p} \right]^{\frac{n}{(p-q+k+1)}} \qquad 4.29$$

$$e = \frac{n}{p-q+k+1} \qquad 4.30$$

And the final equation is

$$\frac{\Delta l}{l_0} = -G \left[D_a \frac{\gamma\,\Omega}{k\,T}\, t \right]^e \qquad 4.31$$

G and *e* are still functions of the geometrical characteristics of the system

$$G \approx \left(2.6202\, a^{-2.113}\right) X_0 + \left(0.5142\, a^{-1.137}\right) \qquad 4.32$$

$$e \approx \left(0.3117\, a^{0.1321}\right) X_0^{-0.132} \qquad 4.33$$

as shown by Figure 4.8.

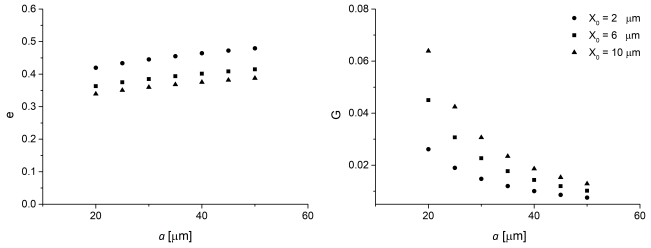

Figure 4.8 The dependence on a and X0 of the parameters *G* and *e* of the shrinkage kinetic equation (adapted from [3])

To predict the shrinkage the coordination number should be introduced in Equation 4.31. Since it has been assumed that each particle has two contacts in the direction along which shrinkage is calculated, $N_C = 2$. The shrinkage kinetic law of a cold compacted iron is therefore Equation 4.34.

$$\frac{\Delta l}{l_0} = -2G \left[D_a \frac{\gamma\,\Omega}{k\,T}\, t \right]^e \qquad 4.34$$

Figure 4.9 shows, as an example, the theoretical shrinkage at 1120°C of a pure iron powder having a particle radius of 30 μm as a function of X_0 (left), and as a function of particle size with constant X_0=4 μm (right).

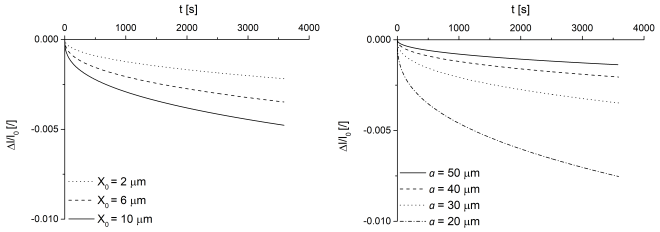

Figure 4.9 Shrinkage at 1120 °C vs the isothermal holding time as a function of X_0 (a = 30 μm) and as a function of a (X_0 = 4μm) (adapted from [3])

Once fixed the isothermal holding time, shrinkage increases on increasing the internal neck radius. This phenomenon represents the geometrical activity in sintering of prior cold compacted powders. In addition, for the same isothermal time, shrinkage increases on decreasing the particle size.

To summarize, the proposed model accounts for the geometrical activity by means of the radius of the contact area between the particles and allows the estimation of the structural activity indirectly, by knowing the experimental shrinkage.

4.3 REFERENCES

[1] R.M. German, Sintering theory and practice, Sinter. Theory Pract. Randall M Ger. Pp 568 ISBN 0-471-05786-X Wiley-VCH January 1996. 1 (1996).

[2] L. Kang, Sintering: Densification, Grain Growth and Microstructure, 2005, Oxford, Elsiever.

[3] S. Baselli, A. Molinari, Sintering shrinkage of uniaxial cold compacted iron: a new shrinkage kinetic equation accounting for the microstructure of the green parts, Powder Metall. 62(1) (2019) 1-7.

[4] A. Molinari, E. Torresani, Preliminary study to determine the sintering stress from microstructural analysis of green parts, Powder Metall. 58(5) (2015) 323-327.

[5] A. Molinari, S. Amirabdollahian, I. Cristofolini, M. Federici, Influence of powder deformation on anisotropy of sintering shrinkage, Adv Powder Metall Part Mater. 1 (2016) 45-52.

[6] A. Molinari, E. Bisoffi, C. Menapace, J. Torralba, Shrinkage kinetics during early stage sintering of cold isostatically compacted iron powder, Powder Metall. 57(1) (2014) 61-69.

[7] A. Molinari, C. Menapace, E. Torresani, I. Cristofolini, M. Larsson, Working hypothesis for origin of anisotropic sintering shrinkage caused by prior uniaxial cold compaction, Powder Metall. 56(3) (2013) 189-195.

[8] Y. Shima, Y. Ishikawa, H. Nitta, Y. Yamazaki, K. Mimura, M. Isshiki, Y. Iijima, Self-Diffusion along dislocations in ultra high purity iron, Mater Trans. 43(2) (2002) 173-177.

5. RESULTS

As anticipated in [1], cold compaction causes structural changes that influence sintering shrinkage. Because of the plastic deformation the powder particles are in contact over a surface, therefore the geometrical relationships in the region of the neck are affected by such a condition [2]. Moreover, the contact areas (which are the grain boundary of the neck) are the source of atoms diffusing towards the neck. The effect on the sintering shrinkage of the presence of interparticle contacts is called geometrical activity. The density of structural defects (mainly dislocations) in the deformed contact regions is higher than that in the starting powder. The result is an increase of the bulk diffusivity [3-5] through the dislocation pipe diffusion mechanism [6], which is particularly active approaching the Curie temperature T_C. The effect on the sintering shrinkage of the presence of a non equilibrium density of structural defects is the structural activity. The results will be interpreted by taking into account these concepts.

In uniaxial cold compaction the axial compaction stress is greater than the radial (transversal) one, causing an inhomogeneous deformation. The powder particles are flattened in the compaction plane thus both the interparticle contacts and the density of structural defects in the deformed regions are larger in the contacts perpendicular to the compaction direction [7].

5.1 IRON

5.1.1 ANALYSIS OF THE DIMENSIONAL VARIATIONS IN SINTERING THROUGH DILATOMETRY TESTS

To measure the dimensional variations in sintering, dilatometry tests were carried out as described in Chapter 3. Figure 5.1 shows a longitudinal and a transversal curve relevant to 7.1 g/cm^3 green density, as an example.

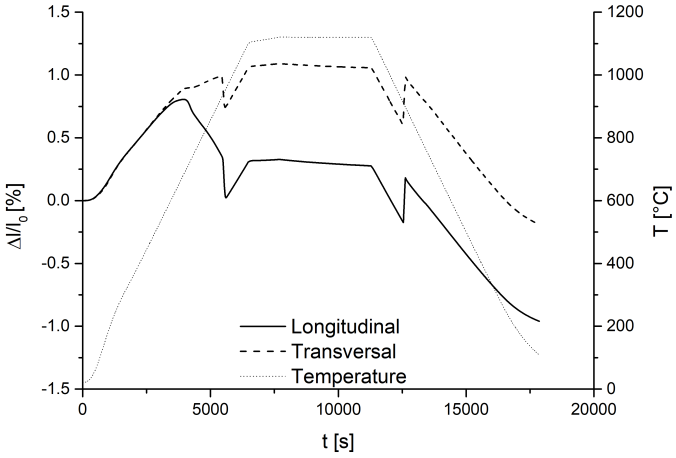

Figure 5.1 Longitudinal and transversal dilatometry curves (green density 7.1 g/cm^3)

It may be immediately observed that the shrinkage is different along the two directions, being higher in that parallel to compaction. A detail of the heating step is highlighted in Figure 5.2.

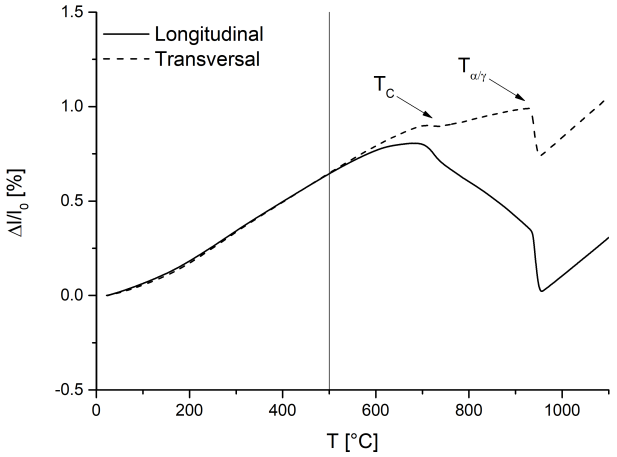

Figure 5.2 Detail of the heating step, longitudinal and transversal curve (green density 7.1 g/cm^3)

On heating, the curves display a linear behavior with a slope that is comparable to the thermal expansion coefficient of α-Fe. From 500 °C there is a progressive decrease in the slope, with different intensity along the two directions. Between 500 °C and the transformation temperature from bcc to fcc iron $T_{\alpha/\gamma}$ the dimensional variations are the sum of two contributes: the thermal expansion and the sintering shrinkage. The shrinkage that occurs during the heating step is distinctly anisotropic. The longitudinal curve shows a maximum just before T_C followed by a sharp contraction that continues until $T_{\alpha/\gamma}$. This means that the contribute of the shrinkage overcomes that of the thermal expansion, resulting in a net contraction. The transversal curve is characterized by a very slight contraction across T_C, afterwards the expansion continues with a slope lower that that at the beginning of the heating step. The shrinkage is active, but not enough to prevail respect to the thermal expansion. After $T_{\alpha/\gamma}$, the curves run parallel with the slope of γ-Fe.

Moving back to Figure 5.1, during the isothermal holding the longitudinal shrinkage is slightly higher than the transversal one.

Ultimately, the sintering shrinkage is due to an anisothermal and an isothermal component, both anisotropic. The anisothermal shrinkage initiate at relatively low temperature (about 500°C) during the heating ramp. The isothermal shrinkage occurs during the holding at the sintering temperature (1120 °C). There is no indication of shrinkage of γ-Fe on heating.

5.1.2 EFFECT OF THE GREEN DENSITY

5.1.2.1 GEOMETRICAL ACTIVITY OF THE GREEN PART

The extension of the interparticle contact areas is not taken into account by the classical sintering theory to model the kinetic of the sintering shrinkage [8-9]. However, these surfaces are the source of the atoms that diffuse to form the neck, so their extension affects the sintering shrinkage. Through the theoretical model explained in Chapter 4 has been demonstrated that larger is a contact, more intense will be the flux of atoms, causing an increase of the shrinkage.

The geometrical activity of the green part may be estimated by measuring the contact lengths between the powder particles, as explained in Chapter 3. Figure 5.3 shows the microstructure of the green compacts of density 6.5 g/cm^3, 6.9 g/cm^3 and 7.3 g/cm^3.

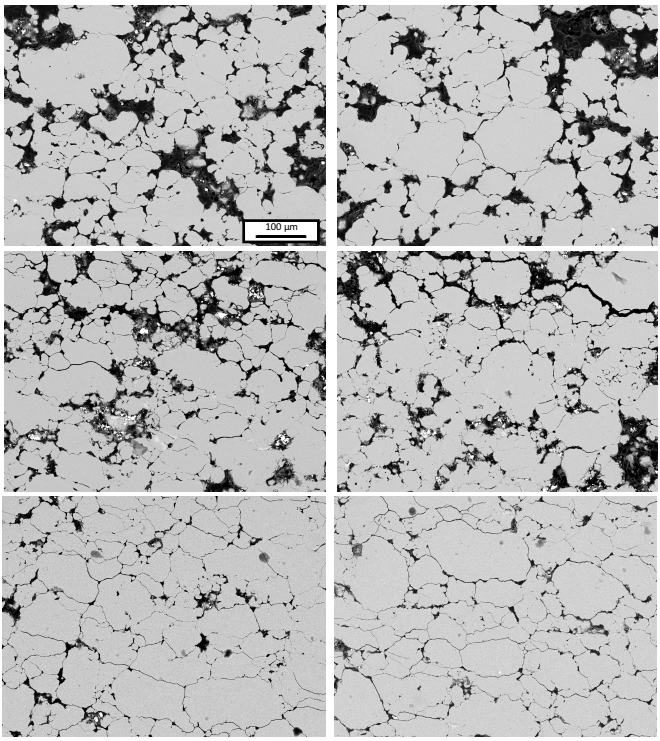

Figure 5.3 SEM images (200X, marker in the first image) of the samples of green density 6.5 g/cm^3 (top), 6.9 g/cm^3 (middle) and 7.3 g/cm^3 (bottom)

By increasing the green density, the powder particles appear more deformed and packed.

To obtain the actual dimension of the contact lengths, data gained by means of image analysis were corrected with a proper coefficient ($2X/2_{True}$ = 0.79) since the metallographic plane does not cut the particles and the contact regions through their centers. The distribution of the diameters of the contact areas in the compaction plane ($2X_L$) and in the compaction direction ($2X_T$) are shown in Figure 5.4.

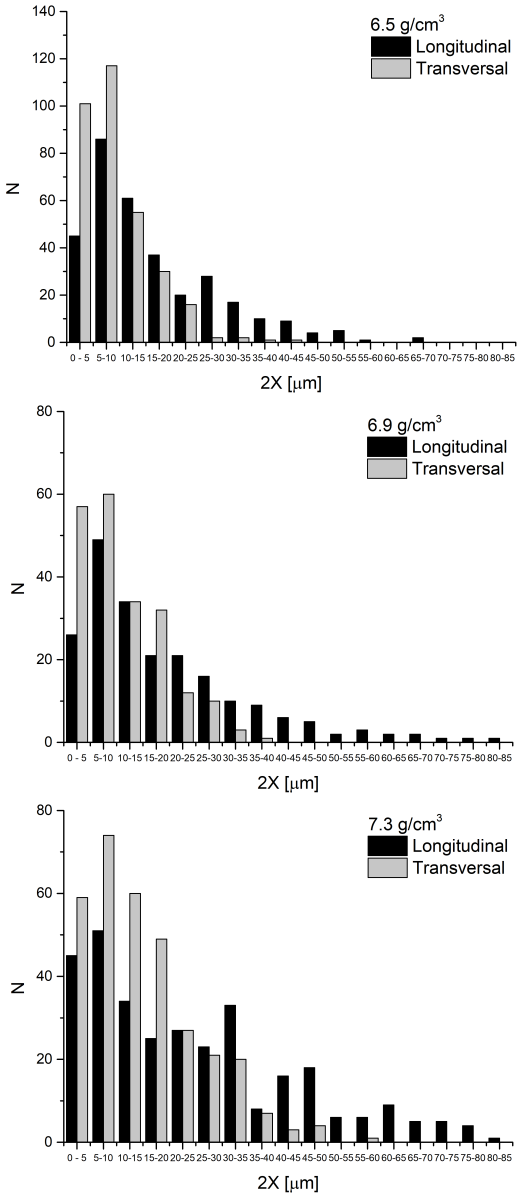

Figure 5.4 Distribution of the contact lengths $2X_L$ and $2X_T$ in case of green density 6.5 g/cm^3 (top), 6.9 g/cm^3 (middle) and 7.3 g/cm^3(bottom)

The distributions show that the contacts perpendicular to the compaction direction are larger than those parallel to it, so the geometrical activity of green parts is anisotropic. Since the former contribute to the longitudinal shrinkage, while the latter contribute to the transversal shrinkage, an anisotropic shrinkage is expected. By increasing the green density, both $2X_L$ and $2X_T$ shift to higher values. In addition, $2X_L$ is characterized by a distribution that is wider than that of $2X_T$. Since the shrinkage kinetic law (Equation 4.34) accounts for the geometrical activity through the radius of the contact area between the powder particles, in this and in the next paragraphs the radius rather than the diameter will be considered. In Table 5.1 are reported the median values of the radii of the contact areas and the ratio X_L/X_T for each green density.

Table 5.1 Median values of the radii of the contact areas and ratio X_L/X_T for each green density

Green density [g/cm^3]	X_L [μm]	X_T [μm]	X_L/X_T [/]
6.5	6.18	3.75	1.6
6.9	6.96	4.46	1.6
7.3	8.47	5.30	1.6

Both X_L and X_T increase by increasing the green density and their ratio remains constant (1.6). Figure 5.5 shows that data may be fitted by a straight line with a good agreement (R^2_{XL} = 0.97 and R^2_{XT} = 0.99).

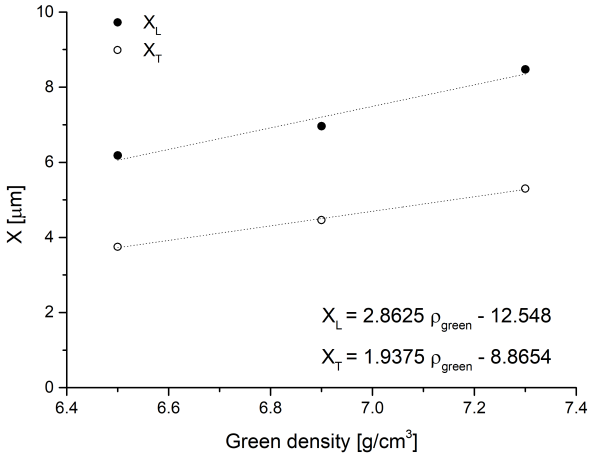

Figure 5.5 Median values of X_L and X_T as a function of green density

This indicate that the geometrical activity increases on increasing the green density.

5.1.2.2 SINTERING SHRINKAGE

To investigate the effect of the green density on the kinetic of the sintering shrinkage and its anisotropy, tests were carried out in the longitudinal and transversal direction on samples with different density. In Figure 5.6 are reported the mean longitudinal and transversal curves for each green density ranging from 6.5 g/cm^3 and 7.3 g/cm^3.

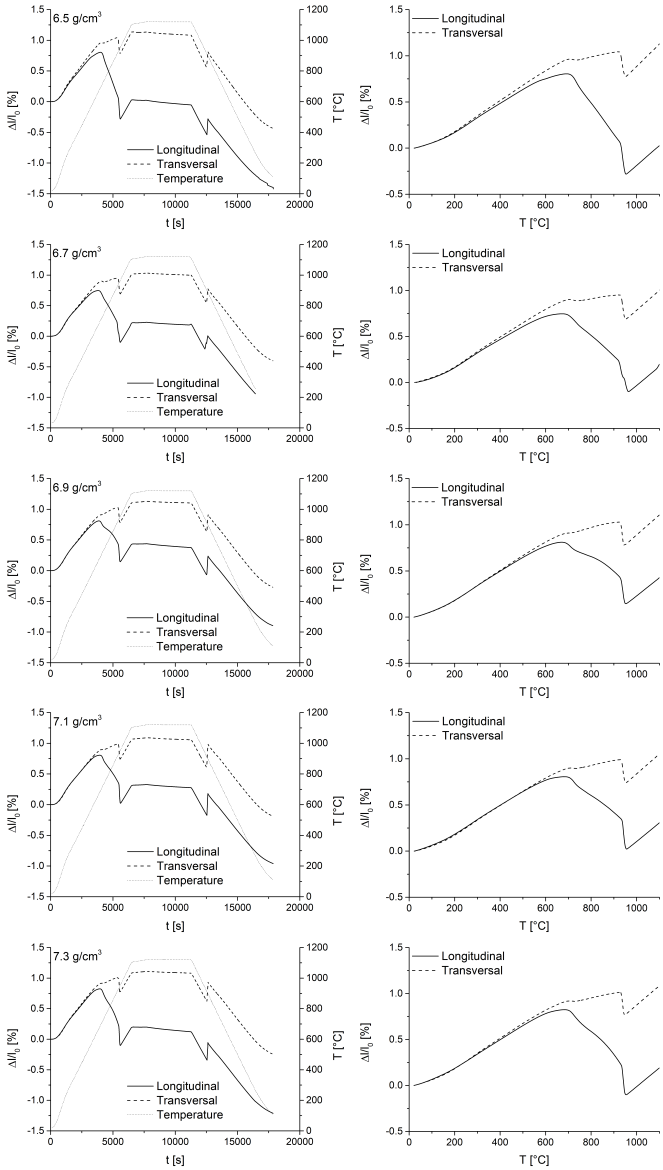

Figure 5.6 Longitudinal and transversal dilatometry curves of samples at green density 6.5 g/cm^3, 6.7 g/cm,^{3} 6.9 g/cm^3, 7.1 g/cm^3 and 7.3 g/cm^3

Between 300 °C and 500 °C all the dilatometry curves display a linear behavior so they have been linearly interpolated in this range of temperatures. The coefficient of thermal expansion corresponds to the slope of the fitting line. The thermal expansion coefficient of bcc iron is 12.2 10^{-6} K^{-1} at 100 °C and increases up to 14.6 10^{-6} K^{-1} at 800 °C [10]. The results of the elaboration of the curves are listed in Table 5.2.

Table 5.2 Thermal expansion coefficient

Green density [g/cm^3]	Thermal Expansion Coefficient [10^{-6} K^{-1}]	
	Longitudinal	Transversal
6.5	15.2	15.8
6.7	14.2	15.6
6.9	15.3	15.8
7.1	15.1	15.5
7.3	15.5	15.7

The coefficients calculated are comparable with the thermal expansion coefficient of α-Fe, hence, below 500 °C, there is neither shrinkage nor anisotropy. This because the diffusive mechanisms responsible for shrinkage are not active.

The anisothermal shrinkage may be determined as the difference between the extrapolation of the line of the thermal expansion (300 °C – 500 °C) and the experimental curve at $T_{\alpha/\gamma}$, as shown in Figure 5.7.

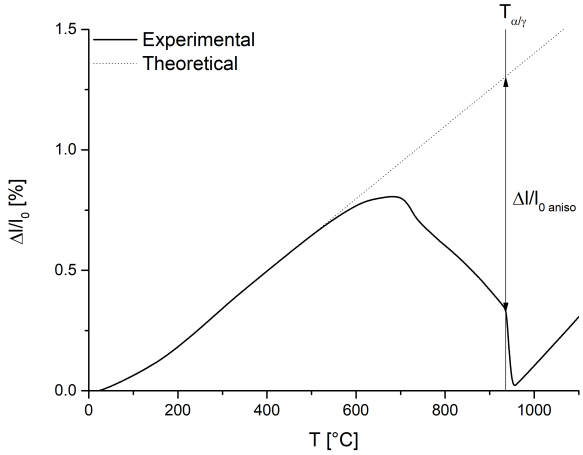

Figure 5.7 Anisothermal shrinkage

Figure 5.8 compares the thermal expansion line and the experimental curve, for each direction and green density, from which have been calculated the results listed in Table 5.3.

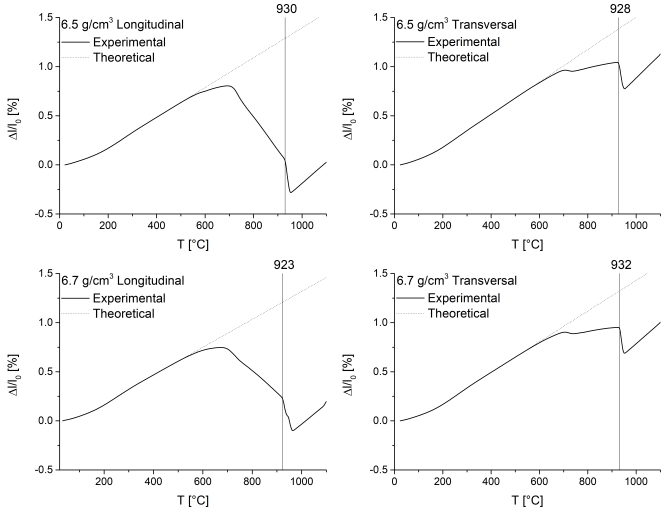

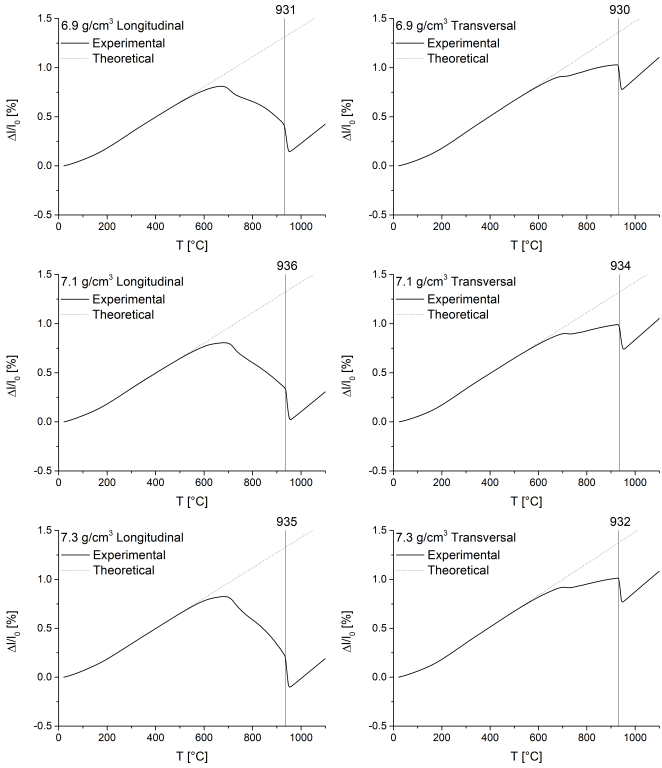

Figure 5.8 Comparison between the line of the thermal expansion and the experimental curve for the longitudinal and transversal direction (green density from 6.5 g/cm^3 to 7.3 g/cm^3)

Table 5.3 $T_{shrinkage}$, $T_{\alpha/\gamma}$ and $\Delta l/l_{0\ aniso}$ in the longitudinal and transversal direction for the five green density

Longitudinal			
Green density [g/cm^3]	**$T_{shrinkage}$ [°C]**	**$T_{\alpha/\gamma}$ [°C]**	**$\Delta l/l_{0\ aniso}$ [%]**
6.5	510	930	-1.16 $\pm$ 0.04
6.7	520	923	-1.01 $\pm$ 0.10
6.9	510	931	-0.87 $\pm$ 0.11
7.1	520	936	-0.95 $\pm$ 0.10
7.3	520	935	-1.09 $\pm$ 0.00
Transversal			
Green density [g/cm^3]	**$T_{shrinkage}$ [°C]**	**$T_{\alpha/\gamma}$ [°C]**	**$\Delta l/l_{0\ aniso}$ [%]**
6.5	570	928	-0.34 $\pm$ 0.00
6.7	550	932	-0.36 $\pm$ 0.00
6.9	550	930	-0.32 $\pm$ 0.02
7.1	550	934	-0.33 $\pm$ 0.03
7.3	530	932	-0.36 $\pm$ 0.00

$T_{shrinkage}$ is the temperature at which the experimental curve deviates from the linearity given by the thermal expansion and it corresponds to the temperature of beginning of shrinkage. Along the longitudinal direction the shrinkage starts at lower temperature and with higher intensity. The dimensional variations in this direction depend on contact areas that are larger and with a higher density of structural defects on increasing green density.

The anisothermal shrinkage is plotted in Figure 5.9 as a function of green density.

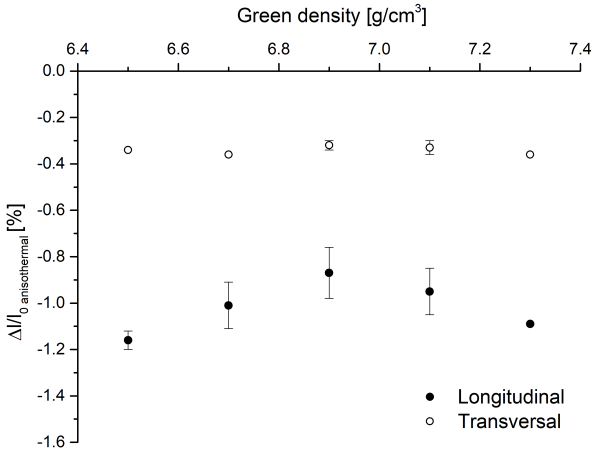

Figure 5.9 Longitudinal and transversal anisothermal shrinkage vs green density

The anisothermal shrinkage is clearly anisotropic, being higher along the longitudinal direction than along the transversal direction. In both directions the anisothermal shrinkage is minimum in case of 6.9 g/cm^3 green density. Moreover, at this density, it is minimum the difference of the shrinkages in the two directions. In the longitudinal direction the dependence on the green density is evident. Data may be interpolated with good correlation (R^2 = 0.95) by a polynomial equation (grade 2) which shows a maximum at green density 6.93 g/cm^3 (Figure 5.10).

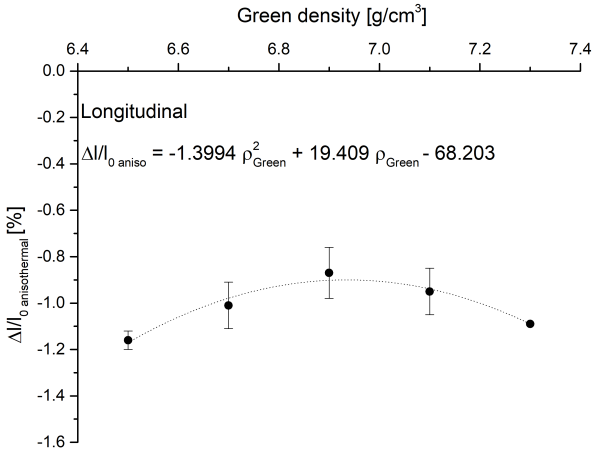

Figure 5.10 Longitudinal anisothermal shrinkage as a function of green density and fitting equation

This result may be explained by taking into account that the sintering shrinkage is affected both by the driving force of sintering and by the prior cold compaction and their effects display an opposite trend depending on the green density. In fact, on increasing the green density, the thermodynamic driving force, that is related to the surface area, decreases while the structural and geometrical activity promoted by cold compaction increase because of a more intense plastic deformation. In the transversal direction the effect of the green density is less evident.

The anisotropy of the anisothermal shrinkage may be evaluated through the parameter K, defined as the ratio between the shrinkage along the longitudinal direction and the shrinkage along the transversal direction. When K is equal to 1 the behavior is isotropic. Results are reported in Figure 5.11 as a function of green density.

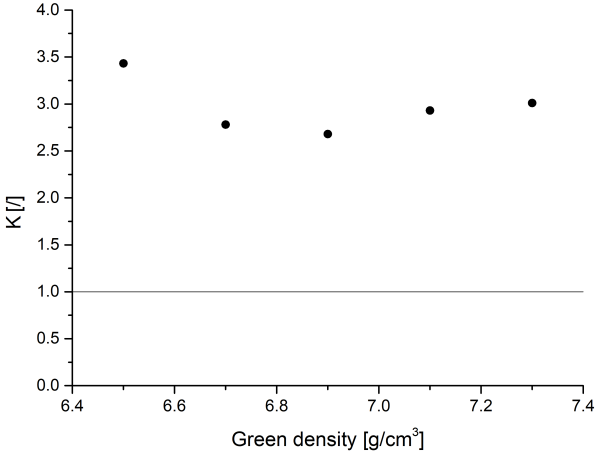

Figure 5.11 Coefficient of anisotropy K vs green density

The anisotropy of the anisothermal shrinkage may be attributed to the inhomogeneous deformation introduced by prior uniaxial cold compaction which causes an anisotropy both in the geometrical and in the structural activity. Indeed, the microstructure of the green parts is anisotropic, characterized by larger interparticle contact areas in the compaction plane as shown in the previous paragraph. In addition, the dislocation density in the deformed contacts perpendicular to the compaction direction is higher than that in the contacts parallel to it.

We may distinguish two components of the anisothermal shrinkage: the anisothermal shrinkage that compensate the thermal expansion ($\Delta l/l_{0\ aniso,\ thermal\ exp}$) and the net anisothermal shrinkage ($\Delta l/l_{0\ aniso,\ net}$). At $T_{\alpha/\gamma}$, $\Delta l/l_{0\ aniso,\ thermal\ exp}$ is the difference between the theoretical thermal expansion and the maximum of the experimental curve before T_C while $\Delta l/l_{0\ aniso,\ net}$ is the difference between the maximum and the experimental curve, as shown in Figure 5.12.

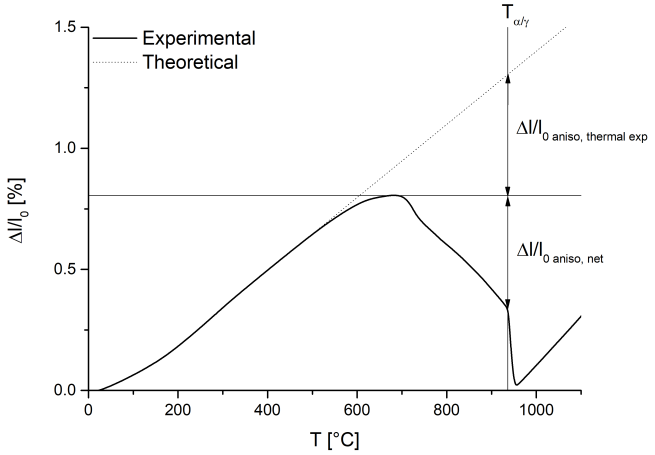

Figure 5.12 The anisothermal shrinkage that compensate the thermal expansion ($\Delta l/l_{0\ aniso,\ thermal\ exp}$) and the net anisothermal shrinkage ($\Delta l/l_{0\ aniso,\ net}$)

Results obtained from the 10 mean curves (longitudinal and transversal direction, 5 green density) are reported in Figure 5.13.

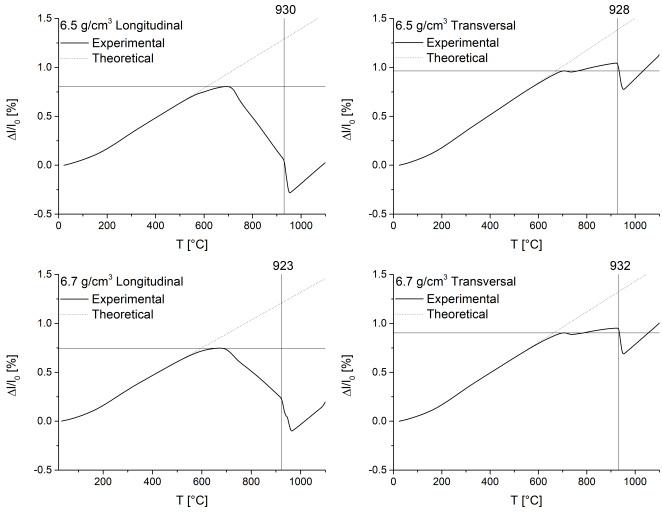

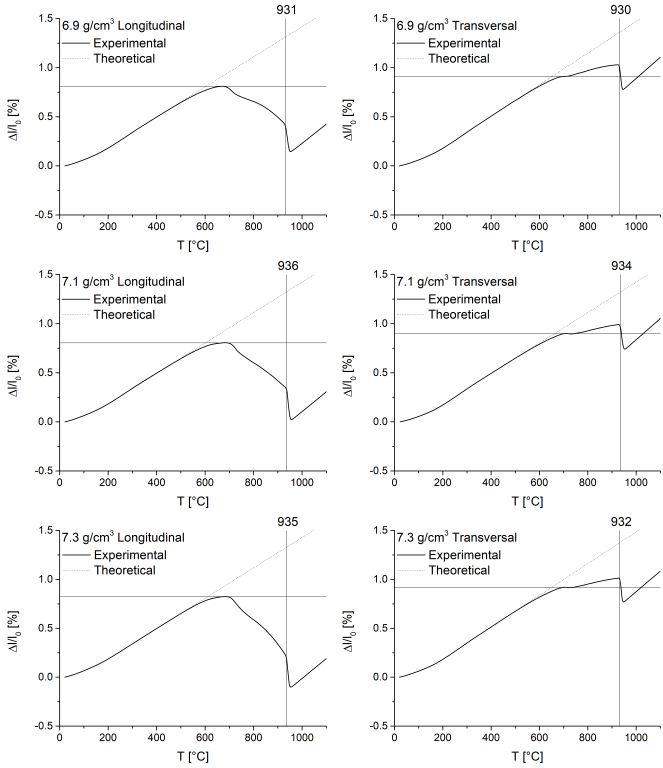

Figure 5.13 $\Delta l/l_{0\ aniso,\ thermal\ exp}$ and $\Delta l/l_{0\ aniso,\ net}$ in the longitudinal and transversal direction (green density from 6.5 g/cm^3 to 7.3 g/cm^3)

At $T_{\alpha/\gamma}$ the sample, in the longitudinal direction, displays an actual shrinkage. In the transversal direction the shrinkage is less intense, it does not prevail over the thermal expansion and the result is that the expansion during heating is mitigated by the shrinkage. Since the net anisothermal shrinkage is equal to zero for the transversal direction, in Table 5.4 and Figure 5.14 data are reported only for the longitudinal one.

Table 5.4 Anisothermal shrinkage in the longitudinal direction

Longitudinal			
Green density [g/cm^3]	**$\Delta l/l_{0\ aniso,\ thermal\ exp}$ [%]**	**$\Delta l/l_{0\ aniso,\ net}$ [%]**	**$\Delta l/l_{0\ aniso}$ [%]**
6.5	-0.48 ± 0.03	-0.68 ± 0.10	-1.16 ± 0.04
6.7	-0.48 ± 0.03	-0.54 ± 0.09	-1.01 ± 0.10
6.9	-0.49 ± 0.03	-0.38 ± 0.08	-0.87 ± 0.11
7.1	-0.50 ± 0.02	-0.46 ± 0.11	-0.95 ± 0.10
7.3	-0.50 ± 0.01	-0.59 ± 0.01	-1.09 ± 0.00

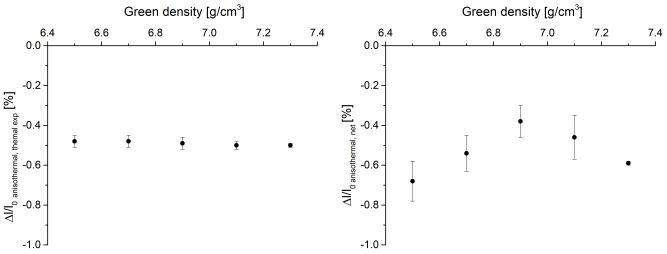

Figure 5.14 Longitudinal direction: $\Delta l/l_{0\ aniso,\ thermal\ exp}$ as a function of green density (left) and $\Delta l/l_{0\ aniso,\ net}$ as a function of green density (right)

$\Delta l/l_{0\ aniso,\ thermal\ exp}$ is constant, independent from the green density, as expected. $\Delta l/l_{0\ aniso,\ net}$ decreases on increasing the green density until a minimum is reached at 6.93 g/cm^3 and then starts growing again. The reason of this trend has been already explained.

After the shrinkage related to the α/γ transformation, the longitudinal and the transversal curves are linear and almost parallel. The slopes of the interpolation lines, which correspond to the thermal expansion coefficient, are listed Table 5.5.

Table 5.5 Thermal expansion coefficient

Green density [g/cm^3]	Thermal Expansion Coefficient [10^{-6} K^{-1}]	
	Longitudinal	Transversal
6.5	21.5	21.4
6.7	20.5	21.5
6.9	19.6	21.6
7.1	20.1	21.5
7.3	20.4	21.1

The thermal expansion coefficients gained from the dilatometry curves in the γ-field are comparable to that of fcc pure iron that is 20.6 10^{-6} K^{-1} [11], so there is no shrinkage of γ-Fe on heating. This because the structural defectiveness introduced by cold compaction is eliminated by the recrystallization of the material during the α/γ transformation. Furthermore, the self-diffusion coefficient of γ-Fe is lower than that of α-Fe [10].

During the isothermal holding at the sintering temperature a shrinkage is registered, as may be observed in Figure 5.15.

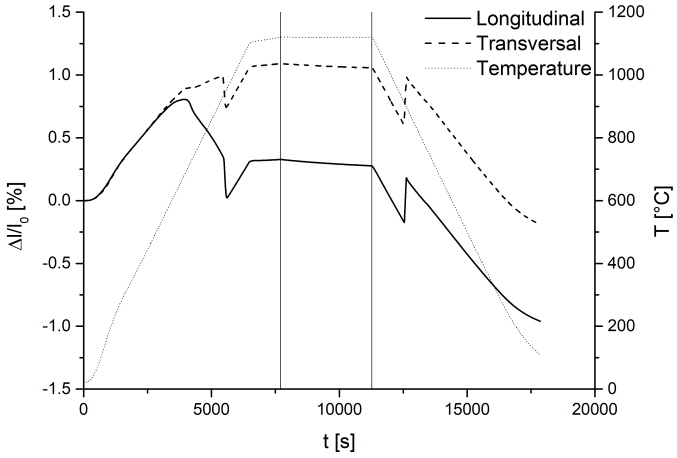

Figure 5.15 Longitudinal and transversal dilatometry curves: the isothermal holding is highlighted

In Figure 5.16 is plotted the isothermal shrinkage in the longitudinal and in the transversal direction as a function of time for the five green densities that have been considered and in Table 5.6 are listed the results.

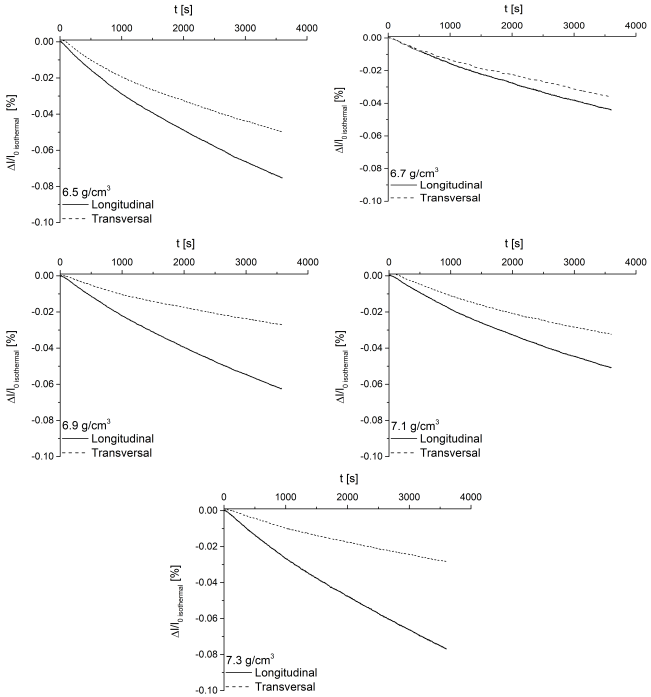

Figure 5.16 Isothermal shrinkage in the longitudinal and transversal direction as a function of time

Table 5.6 Isothermal shrinkage

Green density [g/cm^3]	$\Delta l/l_{0\ iso}$ [%]	
	Longitudinal	Transversal
6.5	-0.08 ± 0.01	-0.05 ± 0.00
6.7	-0.04 ± 0.00	-0.03 ± 0.00
6.9	-0.06 ± 0.01	-0.03 ± 0.00
7.1	-0.05 ± 0.00	-0.03 ± 0.00
7.3	-0.08 ± 0.01	-0.03 ± 0.00

The shrinkage in the longitudinal direction is higher than the shrinkage in the transversal direction. Figure 5.17 allows the evaluation of the dependence of the isothermal shrinkage on the green density.

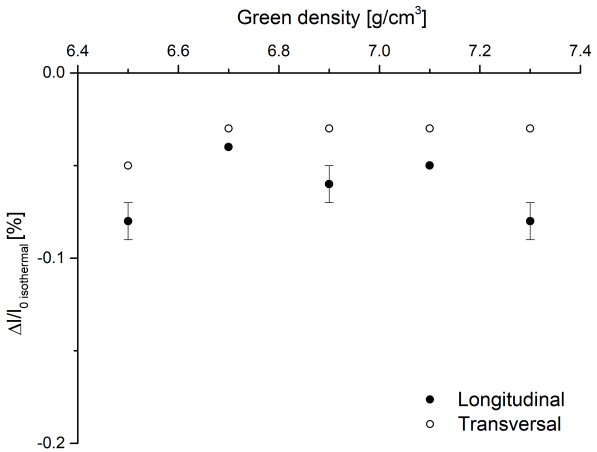

Figure 5.17 Longitudinal and transversal isothermal shrinkage vs green density

As anticipated, even the isothermal shrinkage is anisotropic. In addition, it seems that there is no an obvious effect of the green density.

The anisotropy of the isothermal shrinkage was evaluated through the ratio K between the longitudinal and the transversal shrinkage. Figure 5.18 shows the result vs green density.

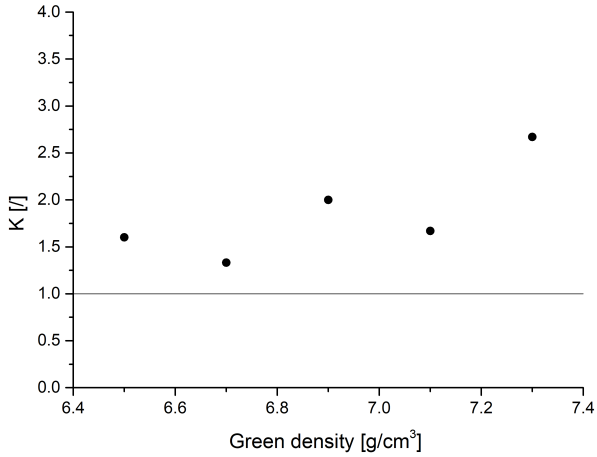

Figure 5.18 Coefficient of anisotropy K vs green density

By comparing Figure 5.11 and Figure 5.18 it is evident that the anisotropy of the isothermal shrinkage is lower than that of the anisothermal one. The anisotropy of the anisothermal shrinkage is a direct consequence of the uniaxial cold compaction that introduces a pronounced anisotropy both in the structural and in the geometrical activity. The recrystallization of the material during the α/γ transformation causes the elimination of the structural defectiveness related to the previous cold compaction. Hence, the anisotropy of the isothermal shrinkage may be imputed to the different extension of the contact areas in the two directions at the sintering temperature.

In Figure 5.19, the isothermal shrinkage is compared to the anisothermal one for each green density and both the directions.

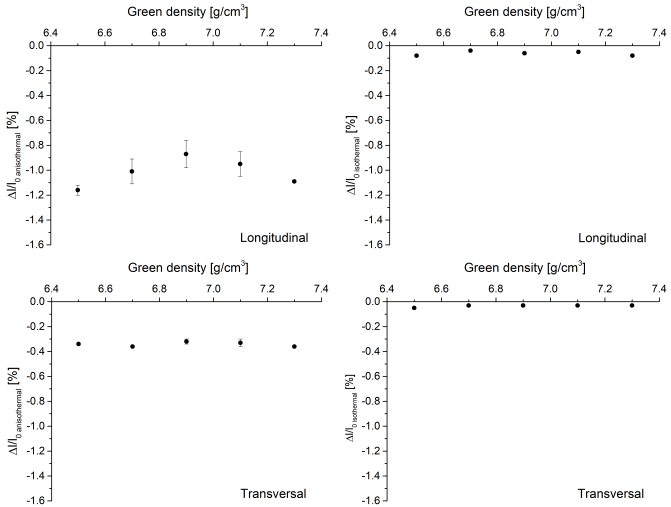

Figure 5.19 Anisothermal and isothermal shrinkages as a function of green density

The anisothermal shrinkage is about 20 times the isothermal shrinkage in the longitudinal direction and 10 times the isothermal shrinkage in the transversal direction for each green density. From the comparison of the slope of the experimental curve with the thermal expansion coefficients of α-Fe and γ-Fe we deduced that the anisothermal shrinkage takes place in the α-field. The isothermal shrinkage takes place in γ-field, at 1120 °C. The anisothermal shrinkage is higher than the isothermal since the self-diffusion coefficient in the fcc lattice is smaller than that in the bcc lattice. In addition, the structural defectiveness introduced by cold compaction is present and pronounced in the α-field and negligible in the in γ-field because of the recrystallization of the material during the phase transformation. The dislocations affect and enhance the bulk diffusivity by means of the dislocation pipe diffusion mechanism [6], which is particularly active approaching the T_C, when the bcc Fe undergoes the transition of the magnetic behavior from

ferromagnetic to paramagnetic, because of the effect of the magnetic dipole on the atomic flow in the pipes.

Since the difference between the isothermal shrinkages at different green density is small in both the directions, it is reasonable to mediate them to obtain a unique longitudinal isothermal shrinkage and a unique transversal isothermal shrinkage. The approximation introduced does not have an important effect on the prediction of the shrinkage because the contribute of the isothermal part is negligible compared to that of the anisothermal part. Figure 5.20 shows the mean isothermal longitudinal and transversal shrinkage and Table 5.7 reports the values reached after an hour of isothermal holding.

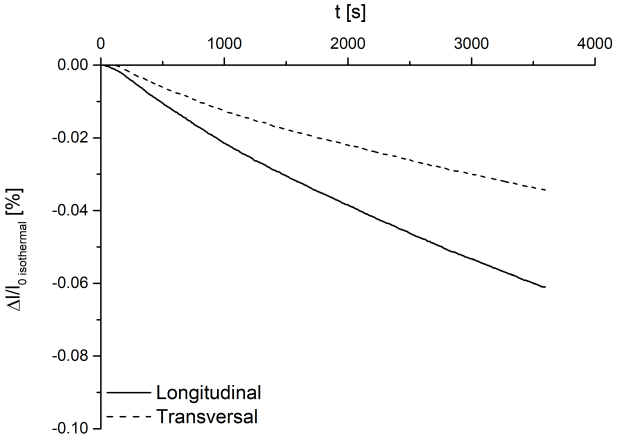

Figure 5.20 Mean longitudinal shrinkage and mean transversal shrinkage as a function of isothermal holding time

Table 5.7 Average isothermal shrinkage in the longitudinal and transversal direction

$\Delta I/I_{0\,iso}$ [%]	
Longitudinal	**Transversal**
-0.06 ± 0.01	-0.03 ± 0.01

The total sintering shrinkage, which is the sum of the anisothermal shrinkage and the isothermal shrinkage, is reported in Figure 5.21 as a function of green density.

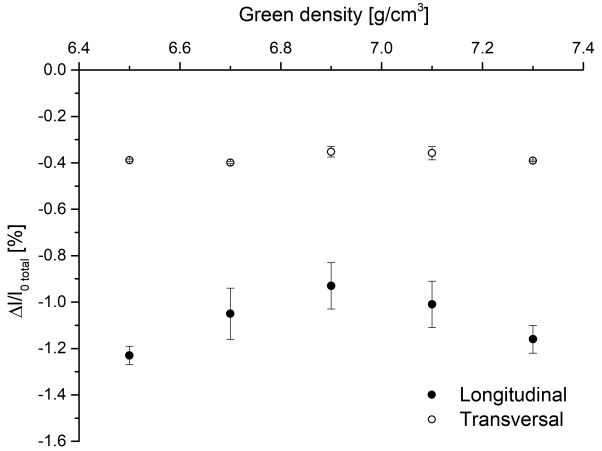

Figure 5.21 Total shrinkage as a function of the green density in the longitudinal and transversal direction

The trend as a function of the green density and the anisotropy are clearly dictated by the anisothermal shrinkage, as expected.

5.1.2.3 GEOMETRICAL ACTIVITY AT THE SINTERING TEMPERATURE

In a previous paragraph, the geometrical activity of the green parts as a function of the green density was estimated by measuring the interparticle contact lengths, which are the diameters of the contact areas. From the dilatometry curves it may be observed that a shrinkage occurs during the heating ramp. The anisothermal shrinkage is a consequence of an increase in the internal neck radius of the powder particles of α-Fe above 500 °C. It follows that the geometrical activity is affected by this phenomenon. Since

no shrinkage is registered in γ-Fe on heating, the geometrical activity at 1120 °C is that present at $T_{\alpha/\gamma}$.The internal neck radius at the sintering temperature is therefore given by two contributes: the internal neck radius of the green part $X_{0,\ green}$ and the increase in the internal neck radius on heating ΔX_{aniso}:

$$X_{0,1120\,°C} = X_{0,green} + \Delta X_{aniso} \qquad 5.1$$

$X_{0,\ green}$ are calculated from the fitting equation (Figure 5.5) for the longitudinal and transversal direction:

$$X_L = 2.8625\ \rho_{green} - 12.548 \qquad 5.2$$

$$X_T = 1.9375\ \rho_{green} - 8.8654 \qquad 5.3$$

$\Delta X_{\ aniso}$ may be calculated through Equation 4.21, which express the shrinkage as a function of the increase of the internal neck radius ΔX and the geometrical parameters of the system a and $X_{0,\ green}$ (directly or through the parameters B and n (Equation 4.16). The anisothermal shrinkage is due to the growth of two necks in the considered direction, so only half of it is taken into account.

$$\Delta X_{aniso} = \left[-\frac{1}{2} \left(\frac{\Delta l}{l_0}\right)_{aniso} \frac{\sqrt{a^2 - X_0^2}}{B} \right]^{\frac{1}{n}} \qquad 5.4$$

The increase in the internal neck radius ΔX_{aniso} and the neck radius at 1120 °C $X_{0,\ 1120\ °C}$ are reported in Table 5.8 and Figure 5. 22 for all the green density and both the directions. They were calculated considering the median particle size which corresponds to a = 37 μm.

Table 5.8 $X_{0,\ green}$, $\Delta l/l_{0\ aniso}$, ΔX_{aniso} and $X_{0,\ 1120\ °C}$ in the longitudinal and transversal direction

Longitudinal				
Green density [g/cm^3]	X_L [μm]	$\Delta l/l_{0\ aniso}$ [%]	ΔX_{aniso} [μm]	$X_{L,\ 1120\ °C}$ [μm]
6.5	6.06	-1.16	1.88	7.94
6.7	6.63	-1.01	1.57	8.20
6.9	7.20	-0.87	1.30	8.50
7.1	7.78	-0.95	1.31	9.09
7.3	8.35	-1.09	1.38	9.73
Transversal				
Green density [g/cm^3]	X_T [μm]	$\Delta l/l_{0\ aniso}$ [%]	ΔX_{aniso} [μm]	$X_{T,\ 1120\ °C}$ [μm]
6.5	3.73	-0.34	1.05	4.78
6.7	4.12	-0.36	1.03	5.15
6.9	4.50	-0.32	0.88	5.38
7.1	4.89	-0.33	0.82	5.71
7.3	5.28	-0.36	0.83	6.11

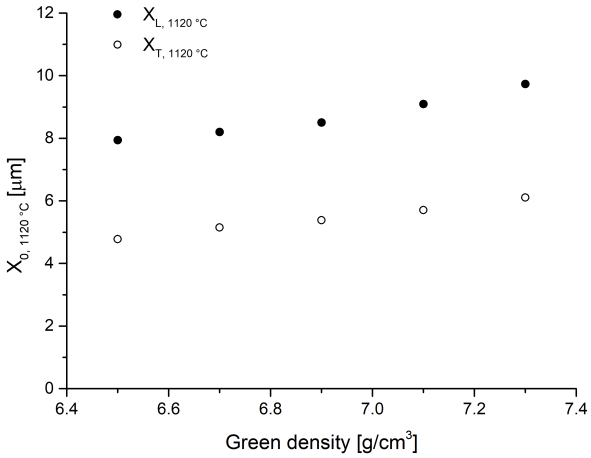

Figure 5.22 $X_{L,\ 1120\ °C}$ and $X_{T,\ 1120°C}$ as a function of green density

Even at the sintering temperature the geometrical activity increases with the increase of the green density and its anisotropic character is maintained, being the contacts that contribute to the longitudinal shrinkage larger than those contribute to the transversal one.

The structural activity due to prior cold compaction has a direct effect on the anisothermal shrinkage and, although it is eliminated during the α/γ transformation, has an indirect effect on the isothermal shrinkage by means of the increase in the geometrical activity on heating. The anisotropy of the isothermal shrinkage depends only on the anisotropy of the geometrical activity.

5.1.2.4 THEORETICAL ISOTHERMAL SHRINKAGE

Once that the internal radius of the neck at the sintering temperature $X_{0,1120°C}$ has been calculated, it is possible to determine the isothermal shrinkage for a holding time of 60 minutes through Equation 4.34. In Table 5.9 are listed the parameters that have been considered. The bulk diffusivity

D_a of γ-Fe [10] pertains to an equilibrium density of structural defects.

Table 5.9 Parameters considered for the calculation the theoretical isothermal shrinkages

a = 37 μm	$\Omega = 1.18\ 10^{-29}\ m^3$
$D_a = 8.85\ 10^{-16}\ m^2/s$	$k = 1.38\ 10^{-23}$ J/K
γ = 2,5 J/m^2	T = 1393 K

Results are shown in Figure 5.23, compared to the experimental shrinkage measured by dilatometry and to the theoretical shrinkage determined neglecting the anisothermal growth of the internal neck radius.

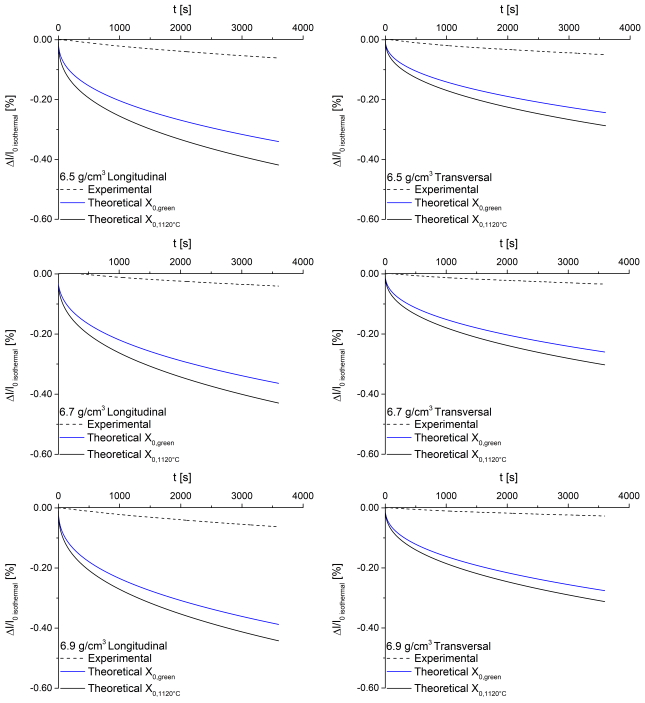

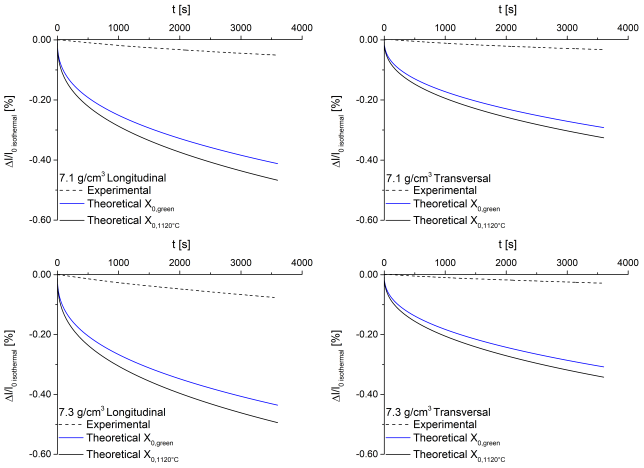

Figure 5.23 Comparison between experimental and theoretical isothermal shrinkage

The anisotropy of the sintering shrinkage is correctly predicted by the model. In addition, the anisothermal neck growth enhances the isothermal shrinkage. Nevertheless, there is a discrepancy between theoretical and experimental results, the shrinkages are overestimated. The difference between theoretical and experimental shrinkages may be attributed to the approximations introduced both in the development and in the application of the model. Concerning the development of the model, r, h, V_N and A_N were approximated. In addition, have been taken into account powder particles of the same dimension, neglecting the particle size distribution that characterizes the powder used for the validation of the model. About the application of the model, the bulk diffusivity in the iron powder may be different from that of pure iron because of the presence of impurities such as Si, Mn and interstitials. Moreover, by introducing a volume diffusion coefficient constant in time the effect of self-activation of sintering is neglected. The use of the median value of the particle size distribution is reasonable, but simplistic.

5.1.2.5 STRUCTURAL ACTIVITY

The effective diffusivity as a function of isothermal sintering time may be determined from the experimental curve through the shrinkage kinetic equation

$$D_{eff} = \left(\frac{-\frac{\Delta l}{l_0}}{2G}\right)^{\frac{1}{e}} \left(\frac{\gamma\Omega}{kT}\, t\right)^{-1} \qquad 5.5$$

The bulk diffusivity is affected by the structural defectiveness, as highlighted in Equation 5.6

$$D_{eff} = D_a \left(1 + \pi r_p^2 \rho_d \frac{D_p}{D_a}\right) \qquad 5.6$$

Where D_a is the diffusivity in presence of an equilibrium density of dislocations (annealed material), r_p is the radius of the pipe (5 10^{-10} m), ρ_d is the dislocation density and D_p is the pipe diffusivity. In [1] was demonstrated that, during sintering at 640 °C, D_{eff} is greater in the longitudinal direction than in the transversal direction, as it was expected, since dislocation density is larger in the longitudinal contacts than in the transversal ones, due to a larger deformation during cold compaction. This reflects the trend of the structural activity of the green part, since 640 °C is a temperature low enough to avoid any modifications of the structural defectiveness. Recrystallization temperature of commercially pure iron is higher, any recovery might occur, that does not modify dislocation density significantly.

Figure 5.24 shows D_{eff} calculated accounting for the mean isothermal shrinkage (Table 5.7) and the mean internal neck radius at 1120 °C ($X_{L,\ 1120\ °C}$ = 8.69 μm, $X_{T,\ 1120\ °C}$ = 5.43 μm) in each direction as a function of time. A similar result has been obtained taking into account the isothermal shrinkage at

each green density (Table 5.6) and the corresponding $X_{0,1120\,°C}$ (Table 5.8) and averaging the curves in the longitudinal and transversal direction.

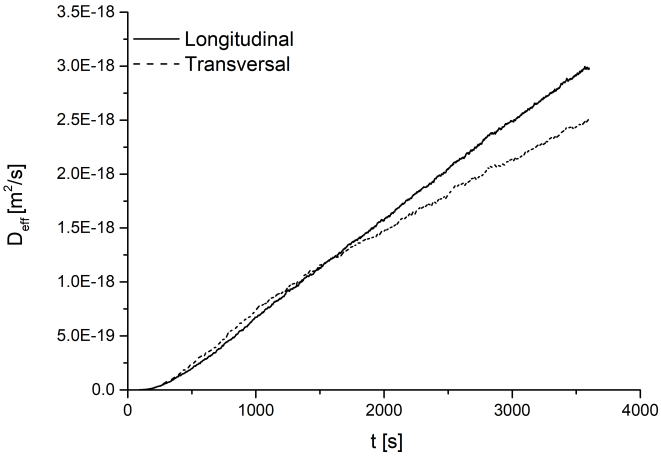

Figure 5.24 Effective diffusion coefficient at 1120 °C along the two directions

There is not an appreciable difference in D_{eff} depending on the direction, except for the final part of the isothermal holding. Therefore the structural activity at 1120 °C may be considered isotropic and the average value can be used. It follows that the anisotropy of the isothermal shrinkage depends on the anisotropy of the geometrical activity at the sintering temperature. The mean effective diffusion coefficient as a function of time is represented in Figure 5.25.

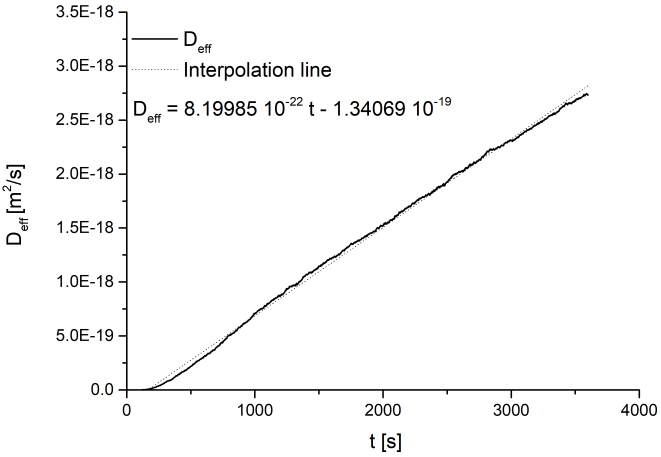

Figure 5.25 Mean diffusion coefficient at 1120 °C

The curve increases with the sintering time and may be interpolated with a linear equation with good agreement (R^2 = 0.99). In previous works [3-5], the trend of D_{eff} as a function of time was discussed on the basis of the self-activation theory of sintering proposed by Friedrich and Schatt [12-14]. During isothermal sintering, dislocation density first increases due to the organization of structural defects emitted during the transformation of the interparticle surface in grain boundary, then decreases due to recrystallization activated by the achievement of a critical dislocation density. The effective diffusivity varies accordingly. The trend in Figure 5.25 is consistent with this theory, the curve does not display the maximum because the critical density of structural defects has not been reached yet.

5.1.3 EFFECT OF THE POWDER MORPHOLOGY

5.1.3.1 CHARACTERIZATION OF THE POWDERS

To have a general view of the morphology of the powder particles, SEM images at low magnification of the loose powders ASC and NC were taken (Figure 5.26).

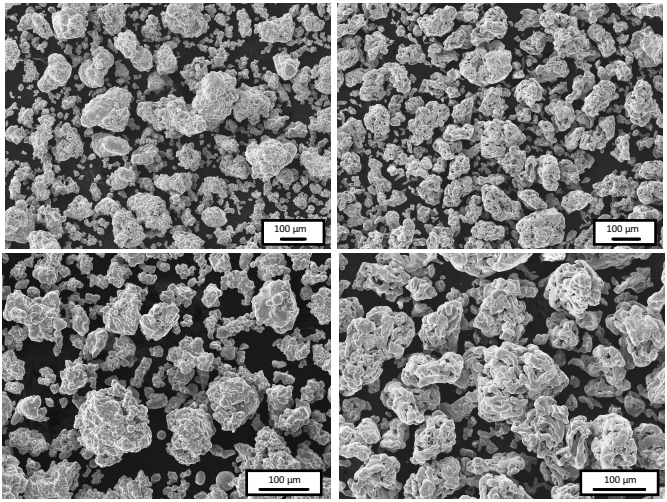

Figure 5.26 ASC powder (left) and NC powder (right)

Both the particles of ASC powder and the particles of NC powder have an irregular shape. ASC seems to have a wider dimensional and shapes distribution than NC, which shows the typical morphology of sponge iron.

To assess the dimensional distribution of the powder particles, tests were carried out with a laser diffraction particle analyzer, as explained in Chapter 3. The results are shown in Figure 5.27, differential and cumulative curve.

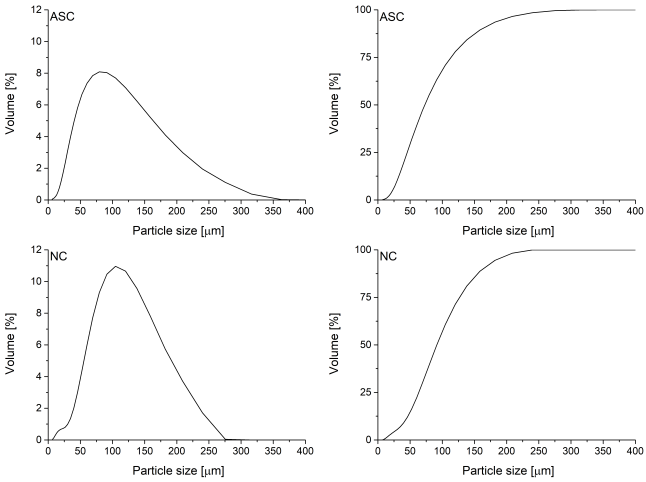

Figure 5.27 Particle size distribution: differential and cumulative curves of ASC (top) and NC (bottom) powders

The analysis confirms that the particle size distribution is wider for ASC than for NC. In Table 5.10 are reported the median and the mode.

Table 5.10 Median particle size and mode of the two powders

Powder	Median particle size [μm]	Mode [μm]
ASC	73	79
NC	92	105

Nitrogen physisorption tests allowed the estimation of the specific surface area. The first step consists in the acquisition of the physisorption isotherms (Figure 5.28).

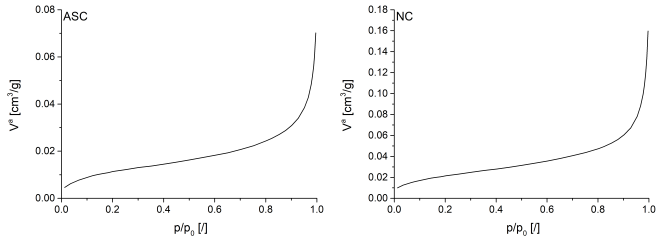

Figure 5.28 Physisorption isotherms: ASC powder (left) and NC powder (right)

According to [15-16] both the curves may be classified as type II, characteristic of non porous or macroporous adsorbents. The desorption curve is overlapped to the adsorption one (no hysteresis cycle is present), hence the curves are type II*a*.

The BET method was used to calculate the specific surface area of the powder particles, so the physisorption isotherms were transformed into BET graphs as shown in Figure 5.29.

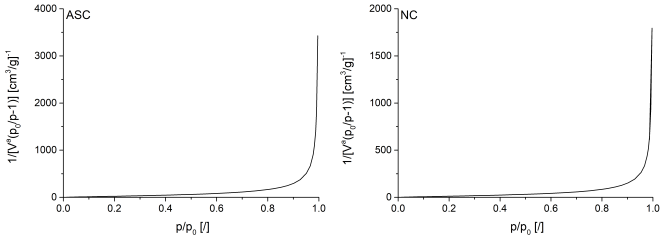

Figure 5.29 BET plot: ASC powder (left) and NC powder (right)

The BET equation is usually applied in the linear form (Equation 5.6)

$$\frac{1}{V^a\left(\frac{p_0}{p}-1\right)} = \frac{1}{V^m C} + \frac{C-1}{V^m C}\left(\frac{p}{p_0}\right) \qquad 5.7$$

The relation between $1/[V^a(p_0/p-1)]$ and p/p_0 is linear in the range of p/p_0 between 0.05 and 0.3, therefore the curves

were interpolated to gain the parameters V^m and C (Figure 5.30, Table 5.11).

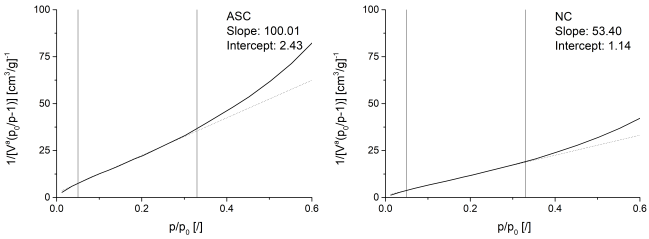

Figure 5.30 Detail of the BET plot: ASC powder (left) and NC powder (right)

Table 5.11 Amount adsorbed and parameter *C*

Powder	V^m [cm^3/g]	*C*
ASC	0.009762	42.128310
NC	0.018335	47.995124

Equation 5.7 allows the calculation of the BET specific area a_s of the adsorbent of mass *m*

$$a_S\,(BET) = \frac{V^m L\,\sigma}{m} \qquad 5.7$$

L is the Avogadro constant and σ is the molecular cross-sectional area. In case of adsorption of Nitrogen, the product $L\sigma$ is equal to 4.35. Results are reported in Table 5.12.

Table 5.12 Specific surface area

Powder	a_s [m^2/g]
ASC	0.0425 ± 0.0005
NC	0.0798 ± 0.0006

The specific surface area of NC powder is almost double than that of ASC powder, as expected.

5.1.4.2 GEOMETRICAL ACTIVITY OF THE GREEN PART

Figure 5.31 shows a comparison between the microstructure of an ASC and a NC sample, both at 6.9 g/cm^3 green density.

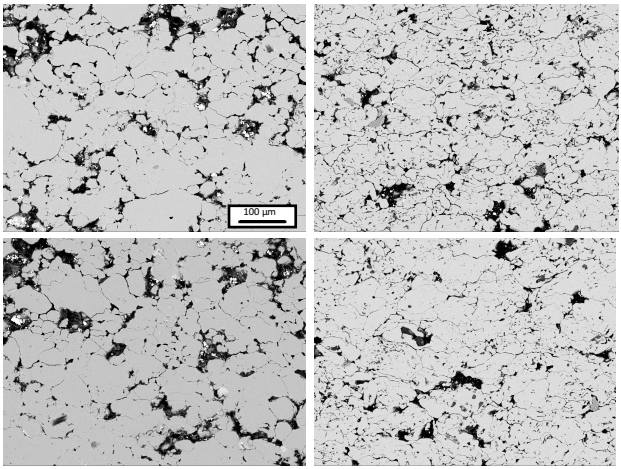

Figure 5.31 SEM micrographs (200X, marker in the first image) of an ASC sample (left) and a NC sample (right), both at green density 6.9 g/cm^3

In both the samples the powder particles appear anisotropically deformed, as expected, because of the uniaxial cold compaction. In addition, it is evident that it is quite tricky to clearly distinguish the particles in case of sponge iron. For this reason, the contacts of only about ten NC particles were measured in order to estimate the geometrical activity of the green part, according to Chapter 3 procedure. Table 5.13 reports the medians X of the radii of the circular interparticle contact surfaces. The measures are multiplied by the coefficient 1.27 ($2X/2X_{True}$ = 0.79) to account for the underestimation of the lengths obtained through image analysis due to the translation and rotation of the metallographic plane respect to the plane passing through the centers of the particles and of the contact areas.

Table 5.13 Median values of the radii of the contact areas

Powder	X_L [μm]	X_T [μm]
ASC	6.96	4.46
NC	6.65	4.34

The geometrical activity is anisotropic, since the contacts that contribute to the longitudinal shrinkage ($2X_L$) are larger than those contribute to the transversal one ($2X_T$). The former lay in the compaction plane, while the latter are parallel to the compaction direction. The medians of the contact lengths for NC are similar to those obtained with ASC. Thus, there is no difference in terms of geometrical activity between ASC and NC samples at the same green density.

5.1.4.3 SINTERING SHRINKAGE

To study the effect of the morphology of the powders on the kinetic of the sintering shrinkage, tests were carried out on samples at the same green density (6.9 g/cm^3) obtained with two iron powders (ASC I and NC) with different characteristics, as highlighted in the previous paragraphs. To assess the anisotropy of the shrinkage, of half of the samples were measured the variations in height (longitudinal curves) and of the remaining half were collected the variation in the diameter (transversal curves).

In Figure 5.32 are shown the longitudinal and transversal dimensional changes as a function of time and the corresponding detail of the heating step as a function of the temperature for both the powders.

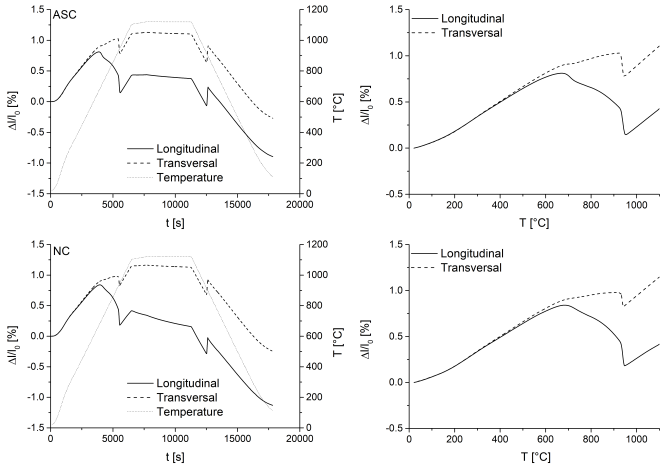

Figure 5.32 Longitudinal and transversal dilatometry curves of samples at 6.9 g/cm^3 green density ASC powder (top) and NC powder (bottom*)*

On heating may be identified two sections in which the curves display a linear trend: between 300 °C and 500 °C and above $T_{\alpha/\gamma}$. In these intervals of temperature, data were interpolated and the thermal expansion coefficients obtained were compared to those of α-Fe and γ-Fe, respectively, for an indication about the presence of shrinkage. In Table 5.14 are reported the results.

Table 5.14 Thermal expansion coefficient

Powder	**α-Fe Thermal Expansion Coefficient [10^{-6} K^{-1}]**		
	Longitudinal	**Transversal**	**Reference (400 °C)**
ASC	15.3	15.8	13.8
NC	15.2	15.9	13.8
Powder	**γ-Fe Thermal Expansion Coefficient [10^{-6} K^{-1}]**		
Powder	**Longitudinal**	**Transversal**	**Reference**
ASC	19.6	21.6	20.6
NC	20.0	20.5	20.6

For each direction and powder, in both the ranges of temperature, the experimental thermal expansion coefficient does not show an important deviation respect to the literature value, therefore there is no indication of shrinkage of α-Fe below 500 °C and of γ-Fe on heating.

The shrinkage on heating occurs in the α-field above 500 °C and increases on increasing the temperature until the α/γ transformation. At the $T_{\alpha/\gamma}$ it is the difference between the line of the thermal expansion determined experimentally (300 °C - 500 °C) and the dilatometry curve. Part of the anisothermal shrinkage compensate the thermal expansion ($\Delta l/l_{0\ aniso,\ thermal\ exp}$), the remaining part is the net shrinkage (($\Delta l/l_{0\ aniso,\ net}$). The former corresponds to the difference between the interpolation line and the maximum of the experimental curve, while the latter is from the maximum until the dilatometry curve, as highlighted in Figure 5.33.

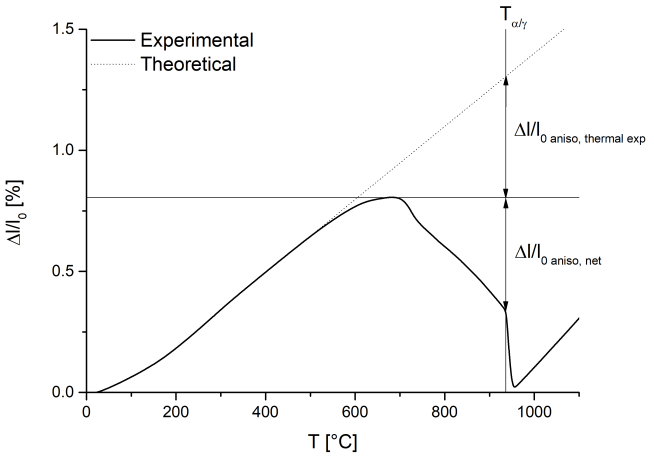

Figure 5.33 Anisothermal shrinkage at the $T_{\alpha/\gamma}$

In Figure 5.34 is highlighted the anisothermal shrinkage for each iron powder and direction, in Table 5.15 are reassumed the results.

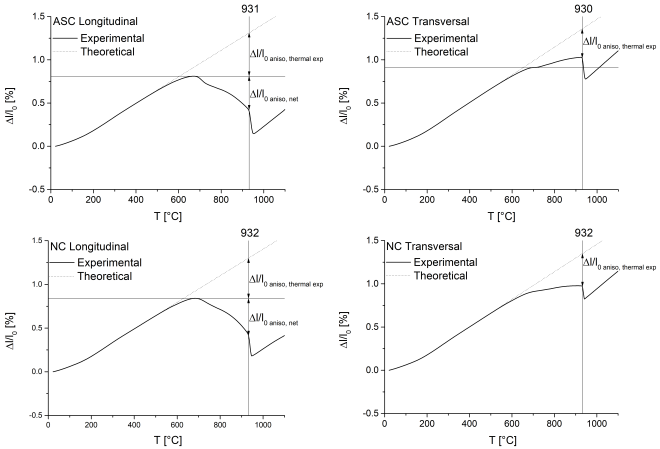

Figure 5.34 Anisothermal shrinkage that compensate the thermal expansion and net in the longitudinal and transversal direction, ASC powder (top) and NC powder (bottom)

Table 5.15 $T_{shrinkage}$, $T_{\alpha/\gamma}$ and anisothermal shrinkage

Longitudinal					
Powder	**$T_{shrinkage}$ [°C]**	**$T_{\alpha/\gamma}$ [°C]**	**$\Delta l/l_{0\ anis}$ [%]**	**$\Delta l/l_{0\ aniso,\ thermal\ exp}$ [%]**	**$\Delta l/l_{0\ aniso,\ net}$ [%]**
ASC	510	931	-0.87 ± 0.11	-0.49 ± 0.03	-0.38 ± 0.08
NC	520	932	-0.88 ± 0.08	-0.48 ± 0.02	-0.40 ± 0.07
Transversal					
Powder	**$T_{shrinkage}$ [°C]**	**$T_{\alpha/\gamma}$ [°C]**	**$\Delta l/l_{0\ aniso}$ [%]**	**$\Delta l/l_{0\ aniso,\ thermal\ exp}$ [%]**	**$\Delta l/l_{0\ aniso,\ net}$ [%]**
ASC	550	930	-0.32 ± 0.02	-0.32 ± 0.02	/
NC	540	932	-0.33 ± 0.02	-0.33 ± 0.02	/

The anisothermal shrinkage initiate slightly before along the longitudinal direction respect to the transversal one, without differences between the two powders. In addition, it is anisotropic as it is higher in the longitudinal direction than in the transversal direction because of the prior uniaxial cold compaction that introduces an anisotropy both in the geometrical and in the structural activity. The results are similar for both the atomized and the sponge iron, for each direction. This means that, when the effect of the deformation prevails, the morphology of the powder does not influence the shrinkage. As already observed in case of ASC, even NC shows a net shrinkage in the longitudinal direction while in the transversal direction the thermal expansion is only partially compensated by the shrinkage.

The sintering shrinkage is the sum of the anisothermal and isothermal shrinkage. Concerning the isothermal shrinkage,

it occurs when the temperature is kept constant, in this case at 1120 °C. In Figure 5.35 is represented the longitudinal and transversal shrinkage as a function of the isothermal holding time and in Table 5.16 are listed the results.

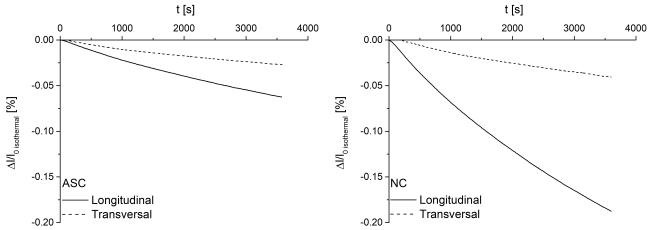

Figure 5.35 Isothermal shrinkage at 1120 °C along the longitudinal and transversal direction as a function of time

Table 5.16 Isothermal shrinkage

Longitudinal	
Powder	**$\Delta l/l_{0\ iso}$ [%]**
ASC	-0.06 ± 0.01
NC	-0.19 ± 0.03
Transversal	
Powder	**$\Delta l/l_{0\ iso}$ [%]**
ASC	-0.03 ± 0.00
NC	-0.05 ± 0.00

Both for ASC and NC, the isothermal shrinkages are significantly lower than the corresponding anisothermal in each direction. The shrinkage at the sintering temperature is still anisotropic, since in the longitudinal direction is higher than in the transversal one and this is particularly evident for sponge iron. The anisotropy is due to the anisotropic geometrical activity. By considering the same direction respect to cold compaction, the isothermal shrinkage is larger for NC than for ASC.

To investigate how the specific surface area of the powders influences the shrinkage removing the effect of the prior cold compaction, dilatometry tests were conducted directly on the tapped powder (Figure 5.36).

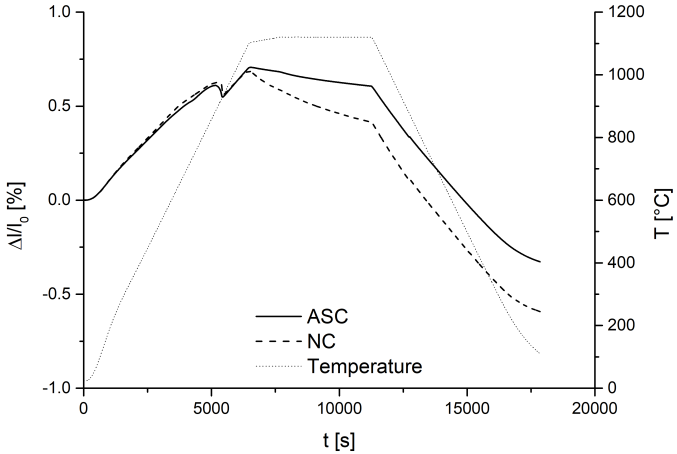

Figure 5.36 Dilatometry curves of ASC and NC powder

These results cannot be compared with those obtained by cold compacted samples because of the different test configuration. The curves do not display a shrinkage on heating, except that related to the austenitic transformation. This confirms that the anisothermal shrinkage is affected by prior cold compaction. In fact, in case of powders that have not been compacted, neither geometrical nor structural activity are present.

In Table 5.17 are reported the isothermal shrinkages at 1120 °C of ASC and NC.

Table 5.17 Isothermal shrinkages relevant to the two tapped powders

Powder	$\Delta l/l_{0\ iso}$ [%]
ASC	-0.08
NC	-0.17

The isothermal shrinkage is significantly higher for NC powder than for ASC powder. This depends on the specific surface area that affects the thermodynamic driving force, since $\Delta G = \gamma \Delta S$ (γ is the surface tension of the material).
The shape of the particles and the porosity inside them are part of the morphological aspects. Their effect is manifest after cold compaction and is particularly pronounced in the longitudinal direction. The shape of the particles may affect the micropores in the contact zones. They are elongated pores, perpendicular to the compaction direction that form because of micro damages during the unloading and the ejection of the part. According to Vagnon *et al.* [17], the pores at the contact interfaces represent a preferential route for the lubricant flow in delubrication resulting in an axial swelling. When sintering starts, these pores get closed rapidly leading to an enhanced shrinkage in the longitudinal direction. The internal pores are characteristic of the sponge powders. They are flattened during uniaxial cold compaction and the contact points act as sites where "internal necks" that contribute to the longitudinal shrinkage may form.

To summarize, the excess of the specific surface area causes a general increase in the isothermal shrinkage, independently from the direction. On the other hand, the shape of the particles and the porosity inside them affect and enhance the shrinkage in the longitudinal direction.

5.2 AISI 316L

The austenitic stainless steel does not display the transition from ferromagnetic to paramagnetic behavior. Therefore, the enhancement of the bulk diffusivity due to the dislocation pipe diffusion mechanism is poor. The low

volume diffusivity of materials with fcc structure requires reaching high sintering temperatures so that shrinkage can occur. At 1000 °C recrystallization of AISI 316L takes place, hence the dislocation density in the contact regions decreases. For the reasons above mentioned, the effect on the sintering shrinkage of the structural activity introduced by prior cold compaction is expected to be modest. It follows that the shrinkage is affected by the geometrical activity and by the thermodynamic driving force. The former is introduced by uniaxial cold compaction that causes plastic deformation of the particles while the latter is related to the specific surface area of the powders, since $\Delta G = \gamma \Delta S$.

To evaluate the dependence of the sintering shrinkage of such a material on the driving force related only to the particle size excluding others morphological aspects, two powders, one with particles larger than 90 μm and the other with particles smaller than 45 μm, have been considered. Dilatometry tests were carried out in the longitudinal and in the transversal direction on samples at green density 6.2 g/cm^3, 6.4 g/cm^3 and 6.6 g/cm^3.

Figure 5.37 shows the dilatometry diagrams relevant to the heating and the isothermal holding. During the cooling step only the thermal contraction occurs, so it is not reported.

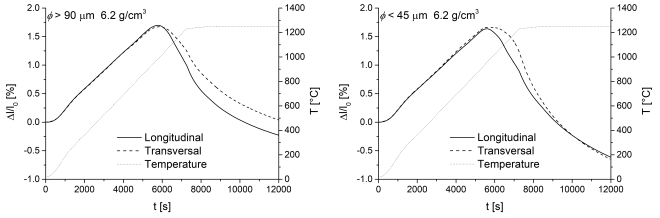

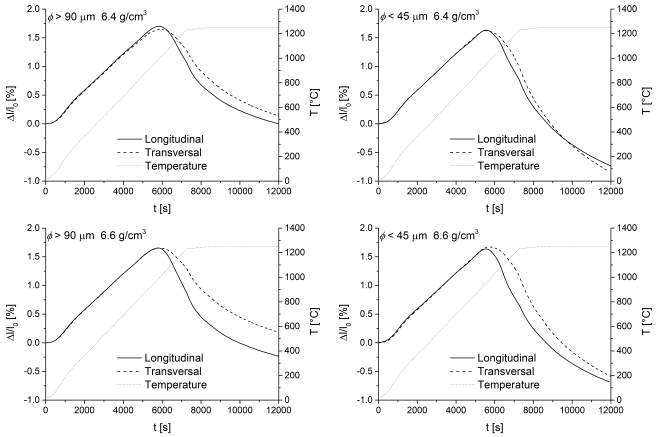

Figure 5.37 Longitudinal and transversal dilatometry curves (heating and isothermal holding) for ϕ > 90 μm (left) and ϕ < 45 μm (right) and green density between 6.2 g/cm^3 and 6.6 g/cm^3

5.2.1 ANISOTHERMAL SHRINKAGE

In Figure 5.38 are reported, for sake of exemplification, the dimensional changes in the longitudinal direction as a function of the temperature in case of ϕ > 90 μm and green density 6.4 g/cm^3.

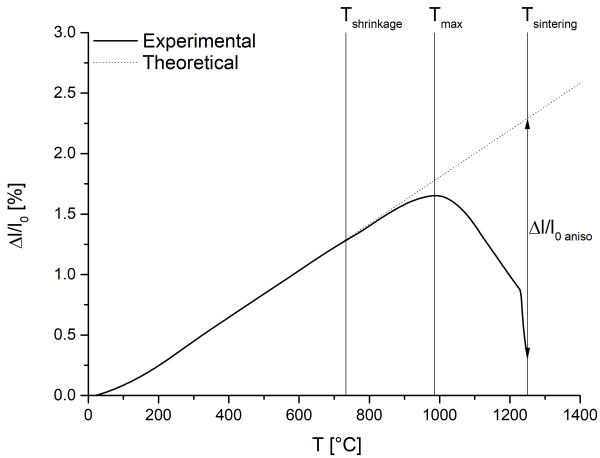

Figure 5.38 Dimensional changes on heating as a function of temperature and theoretical thermal expansion

On heating, the studied material does not undergo phase transformations that might overshadow significant details of the curve. From room temperature, excluding some deviations below 300 °C due to the thermal inertia of the system, the trend is linear and dictated by the thermal expansion. Above 700 °C, the expansion rate starts to decrease attesting the activation of transport phenomena that cause shrinkage. Until 900 °C the contribute of the shrinkage is negligible, then increases rapidly exceeding the thermal expansion and resulting in a maximum of the curve followed by a net contraction. The sharp shrinkage registered between 1230 °C and 1250 °C is related to the decrease of the heating rate from 10 °C/min to 1 °C/min, as explained in Chapter 3.

Henceforward, the anisothermal shrinkage up to 1250 °C will be taken into account and the data are listed, together with the temperature of the maximum of the curve T_{max}, in Table 5.18.

Table 5.18 Anisothermal shrinkage and temperature of the maximum of the curve

ϕ > 90 μm				
Green density [g/cm^3]	**Longitudinal**		**Transversal**	
	$\Delta l/l_{0\ aniso}$ [%]	**T_{max} [°C]**	**$\Delta l/l_{0\ aniso}$ [%]**	**T_{max} [°C]**
6.2	-1.92 ± 0.04	984	-1.59 ± 0.04	998
6.4	-1.77 ± 0.04	994	-1.53 ± 0.03	1010
6.6	-1.97 ± 0.01	986	-1.49 ± 0.05	995
ϕ < 45 μm				
Green density [g/cm^3]	**Longitudinal**		**Transversal**	
	$\Delta l/l_{0\ aniso}$ [%]	**T_{max} [°C]**	**$\Delta l/l_{0\ aniso}$ [%]**	**T_{max} [°C]**
6.2	-2.17 ± 0.02	954	-2.20 ± 0.10	964
6.4	-2.21 ± 0.07	948	-2.06 ± 0.09	959
6.6	-2.19 ± 0.04	952	-1.90 ± 0.04	973

T_{max} is not affected by the green density and, by considering the same direction, is lower for the powder with particles smaller than 45 μm (Figure 5.39). This means that the shrinkage predominates over the thermal expansion at a lower temperature for fine powders than for coarse powders, because of their larger driving force related to the specific surface area $\Delta G = \gamma \Delta S$.

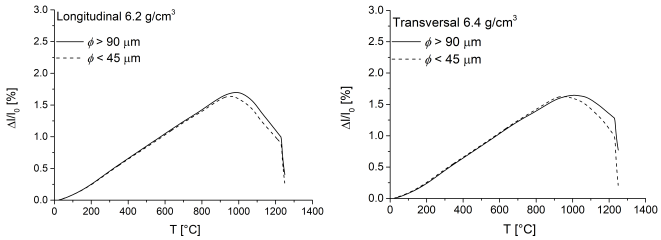

Figure 5.39 Comparison between the relative change in length as a function of temperature of the two powders in the longitudinal direction in case of green density 6.2 g/cm^3 (left) and in the transversal direction in case of green density 6.4 g/cm^3 (right)

For each powder and green density, the maximum of the curve is shifted to a lower temperature for the longitudinal direction because of the enhancement of the shrinkage due to the higher geometrical activity (Figure 5.40).

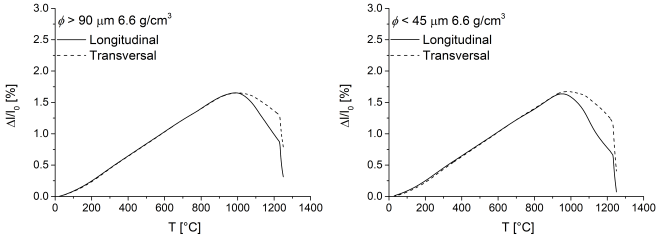

Figure 5.40 Relative change in length vs temperature in the longitudinal and transversal direction for the green density 6.6 g/cm^3 in case of ϕ > 90 μm (left) and ϕ < 45 μm (right)

To verify the anisotropy of the geometrical activity of the green parts, contact lengths between the powder particles have been measured in specimens made by the powders ϕ > 90 μm and ϕ < 45 μm and green density 6.5 g/cm^3. Samples preparation, acquisition of the images and their elaboration and the correction of the results to account for the error introduced by the procedure were carried out as explained in Chapter 3. Figure 5.41 relates to OM images of the two samples.

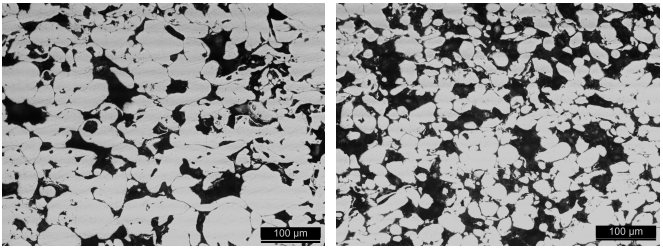

Figure 5.41 OM micrographs (200X) of the sample ϕ > 90 μm (left) and ϕ < 45 μm (right)

The radii of the contact areas in the direction perpendicular (X_L) and parallel (X_T) to compaction are reported in Table 5.19. They are responsible for the longitudinal and the transversal shrinkage, respectively.

Table 5.19 Median values of the radii of the contact areas

Powder	X_L [μm]	X_T [μm]
ϕ > 90 μm	7.4	5.3
ϕ < 45 μm	4.4	3.0

This result confirms the anisotropic character of the geometrical activity introduced by prior cold compaction. The contact areas that contribute to the axial shrinkage are larger than those contribute to the radial one, thus an increase of the longitudinal shrinkage occur.

In Figure 5.42 the anisothermal shrinkages in the longitudinal and in the transversal direction are represented vs green density for the powder with particles larger than 90 μm (left) and smaller than 45 μm (right).

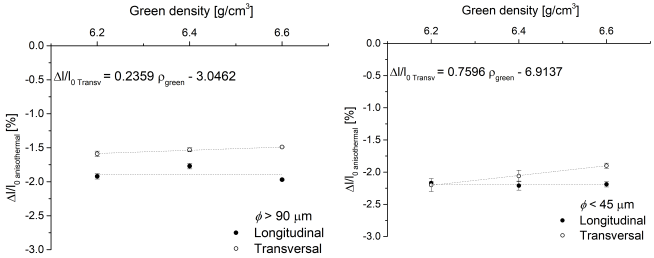

Figure 5.42 Anisothermal shrinkage vs green density in the longitudinal and transversal direction: ϕ > 90 μm (left) and ϕ < 45 μm (right)

Concerning the powder ϕ > 90 μm, on increasing the green density, the longitudinal shrinkage does not show a trend, the difference between the three values is small and they

are, on average, around -1.89 % while the transversal shrinkage slightly and linearly (R^2 = 0.98) decreases. About the powder ϕ < 45 μm, the shrinkage in the longitudinal direction is constant and, on average, equal to -2.19 %. The shrinkage in the transversal direction decreases on increasing the green density in a more decisive way than for powder ϕ > 90 μm and the data may be linearly interpolated with good agreement (R^2 = 0.99). In general, the dependence of the anisothermal shrinkages on the green density is poor. In the longitudinal direction they are practically constants and their value depends on the powder. In the transversal direction they tend to decrease on increasing the green density less evidently for the coarse powder and more decisively for the fine powder. For both the powders and all densities, except for ϕ < 45 μm and density 6.2 g/cm^3, the longitudinal shrinkage is higher than the transversal one.

The anisotropy of the anisothermal shrinkage is evaluated through the parameter $K = \Delta l/l_{0\ aniso\ Long} / \Delta l/l_{0\ aniso\ Transv}$ (Figure 5.43) that assumes the value 1 in case of isotropic behavior.

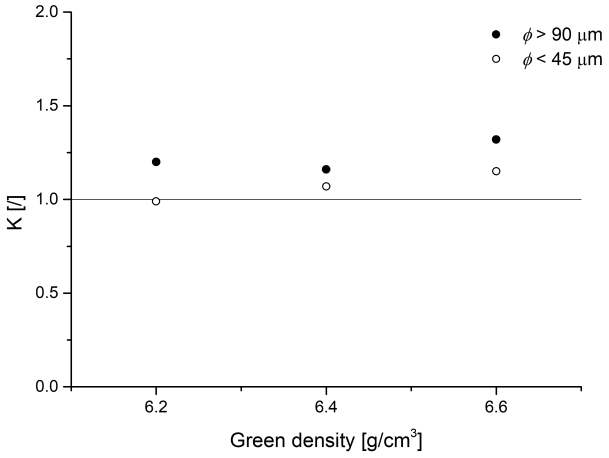

Figure 5.43 Anisotropy of the anisothermal shrinkage

The anisotropy is weak and is always greater for ϕ > 90 μm than for ϕ < 45 μm. On increasing the green density, the finer powder moves from isotropy to an increasingly anisotropic behavior. The anisotropy of the anisothermal shrinkage may be exclusively imputed to anisotropic geometrical activity introduced by uniaxial cold compaction whose effect is more evident for coarse powders, since they have a lower driving force related to the excess of specific surface area than fine powders.

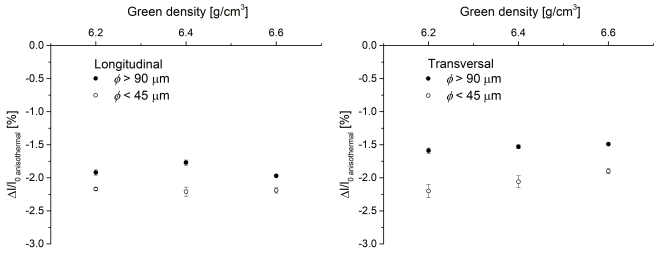

Figure 5.44 Anisothermal shrinkage as a function of the green density in the longitudinal direction (left) and in the transversal direction (right)

From the comparison of the dimensional variations in the same direction (Figure 5.44) it may be observed that the small size of the powder particles enhances the shrinkage because of a higher thermodynamic driving force. Moreover, the increase is particularly pronounced in the transversal direction. This behavior has not been interpreted yet and will be object of future investigations.

Above T_{max}, the shrinkage overcomes the thermal expansion. From the theoretical $\Delta l/l_0$ at 1250 °C to the maximum of the curve, the anisothermal shrinkage compensate the thermal expansion ($\Delta l/l_{0\ aniso,\ thermal\ exp}$). Between the $\Delta l/l_0$ corresponding to the maximum and the actual $\Delta l/l_0$ at the sintering temperature, the anisothermal shrinkage is net

($\Delta l/l_{0\ aniso,\ net}$). $\Delta l/l_{0\ aniso,\ thermal\ exp}$ and $\Delta l/l_{0\ aniso,\ net}$ are shown in Figure 5.45.

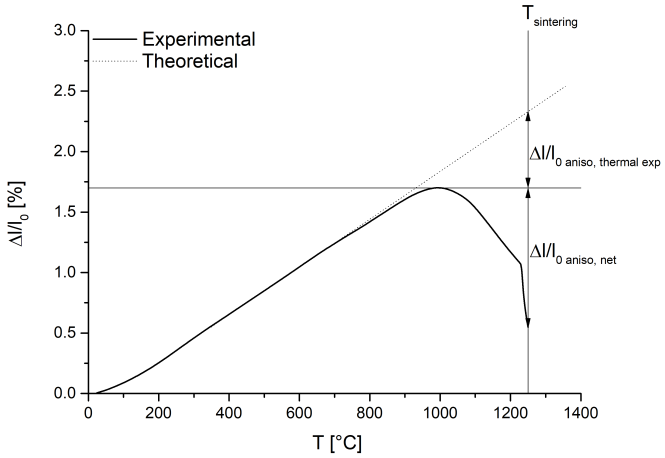

Figure 5.45 The anisothermal shrinkage that compensate the thermal expansion ($\Delta l/l_{0\ aniso,\ thermal\ exp}$) and the net anisothermal shrinkage ($\Delta l/l_{0\ aniso,\ net}$)

The results relevant to both the powders and directions and all the green density taken into consideration are reported in Table 5.20 and graphically represented in Figure 5.46.

Table 5.20 Anisothermal shrinkage

ϕ > 90 μm			
Longitudinal			
Green density [g/cm^3]	**$\Delta l/l_{0\ aniso,\ thermal\ exp}$ [%]**	**$\Delta l/l_{0\ aniso,\ net}$ [%]**	**$\Delta l/l_{0\ aniso}$ [%]**
6.2	-0.62 ± 0,03	-1.30 ± 0.04	-1.92 ± 0.04
6.4	-0.62 ± 0,02	-1.15 ± 0.04	-1.77 ± 0.04
6.6	-0.63 ± 0,01	-1.34 ± 0.01	-1.97 ± 0.01
Transversal			
Green density [g/cm^3]	**$\Delta l/l_{0\ aniso,\ thermal\ exp}$ [%]**	**$\Delta l/l_{0\ aniso,\ net}$ [%]**	**$\Delta l/l_{0\ aniso}$ [%]**
6.2	-0.64 ± 0.04	-0.95 ± 0.02	-1.59 ± 0.04
6.4	-0.65 ± 0.03	-0.88 ± 0.02	-1.53 ± 0.03
6.6	-0.64 ± 0.05	-0.85 ± 0.02	-1.49 ± 0.05
ϕ < 45 μm			
Longitudinal			
Green density [g/cm^3]	**$\Delta l/l_{0\ aniso,\ thermal\ exp}$ [%]**	**$\Delta l/l_{0\ aniso,\ net}$ [%]**	**$\Delta l/l_{0\ aniso}$ [%]**
6.2	-0.64 ± 0.01	-1.53 ± 0.02	-2.17 ± 0.02
6.4	-0.68 ± 0.03	-1.53 ± 0.07	-2.21 ± 0.07
6.6	-0.63 ± 0.02	-1.56 ± 0.04	-2.19 ± 0.04
Transversal			
Green density [g/cm^3]	**$\Delta l/l_{0\ aniso,\ thermal\ exp}$ [%]**	**$\Delta l/l_{0\ aniso,\ net}$ [%]**	**$\Delta l/l_{0\ aniso}$ [%]**
6.2	-0.69 ± 0.03	-1.51 ± 0.10	-2.20 ± 0.10
6.4	-0.68 ± 0.01	-1.38 ± 0.09	-2.06 ± 0.09
6.6	-0.63 ± 0.02	-1.25 ± 0.04	-1.90 ± 0.04

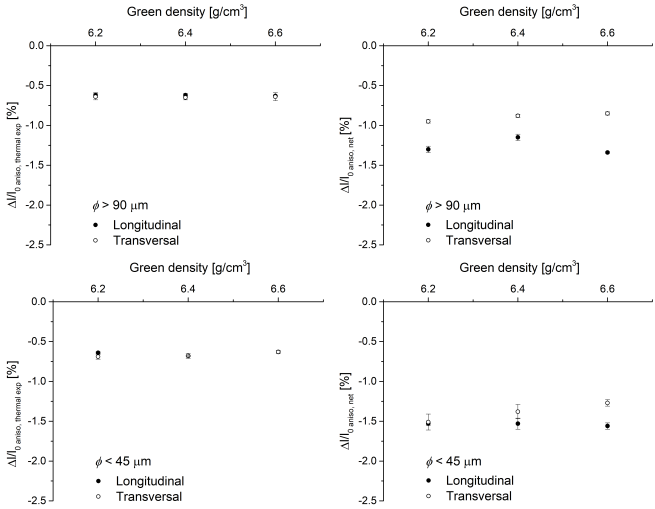

Figure 5.46 $\Delta l/l_{0\ aniso,\ thermal\ exp}$ and $\Delta l/l_{0\ aniso,\ net}$ as a function of the green density in case of ϕ > 90 μm (top) and ϕ < 45 μm (bottom)

As already observed for iron, $\Delta l/l_{0\ aniso,\ thermal\ exp}$ is independent of powder, density and direction and, for AISI 316L, equal to -0.65 %, on average. $\Delta l/l_{0\ aniso,\ net}$ has the same trend shown in Figure 5.42, simply moved to lower values by 0.65 %.

5.2.2 ISOTHERMAL SHRINKAGE

The isothermal shrinkage occurs during the permanence at 1250 °C for one hour, as highlighted in Figure 5.47 in case of ϕ > 90 μm and green density 6.4 g/cm^3.

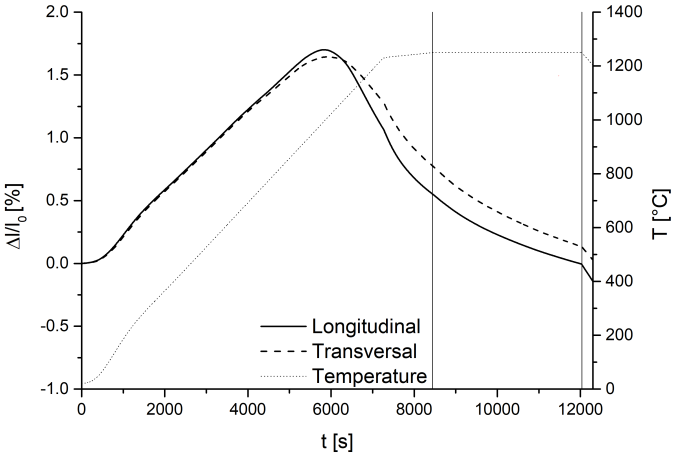

Figure 5.47 Longitudinal and transversal dilatometry curve: the isothermal holding is highlighted

The isothermal dimensional variations as a function of holding time in the longitudinal and transversal direction for the two powders and the three green density considered are represented in Figure 5.48 and listed in Table 5.21.

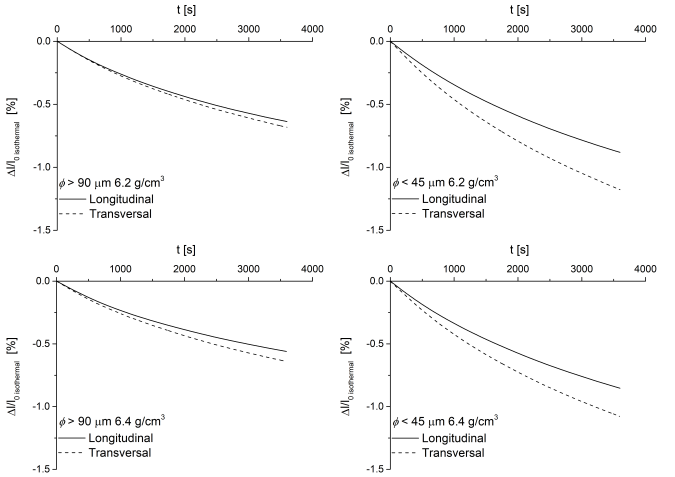

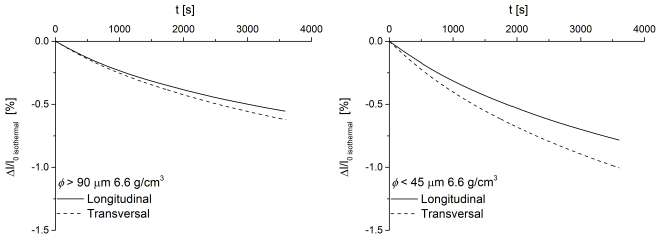

Figure 5.48 Isothermal shrinkage in the longitudinal and transversal direction as a function of time

Table 5.21 Isothermal shrinkage

ϕ > 90 μm		
Green density [g/cm^3]	**$\Delta I/I_{0\ isothermal}$ [%]**	
	Longitudinal	**Transversal**
6.2	-0.63 ± 0.01	-0.69 ± 0.01
6.4	-0.56 ± 0.03	-0.64 ± 0.02
6.6	-0.56 ± 0.02	-0.62 ± 0.06
ϕ < 45 μm		
Green density [g/cm^3]	**$\Delta I/I_{0\ isothermal}$ [%]**	
	Longitudinal	**Transversal**
6.2	-0.88 ± 0.02	-1.18 ± 0.02
6.4	-0.85 ± 0.02	-1.08 ± 0.01
6.6	-0.78 ± 0.02	-1.01 ± 0.01

Unlike what has been observed for iron, the isothermal transversal shrinkage is higher than the isothermal longitudinal shrinkage.

In order to evaluate the dependence of the shrinkage on the green density, data of Table 5.21 are graphically represented in Figure 5.49.

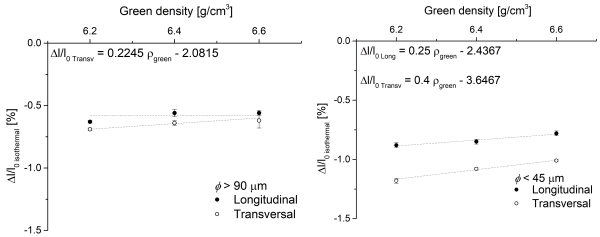

Figure 5.49 Isothermal shrinkage vs green density in the longitudinal and transversal direction: ϕ > 90 μm (left) and ϕ < 45 μm (right)

The isothermal shrinkages are lower but comparable than the corresponding anisothermals. In case of coarse powder, the longitudinal shrinkage is constant (-0.58 %) and the transversal shrinkage decreases linearly (R^2 = 0.94) on increasing the green density. For the fine powder, the shrinkage both in the longitudinal and in the transversal direction decrease linearly (R^2_{Long} = 0.90 R^2_{Transv} = 0.97) on increasing the green density. The transversal shrinkage exceeds the longitudinal shrinkage for both the powders and all the green density.

Figure 5.50 shows the anisotropy of the isothermal shrinkage expressed as the ratio K between the longitudinal and the transversal shrinkage as a function of green density.

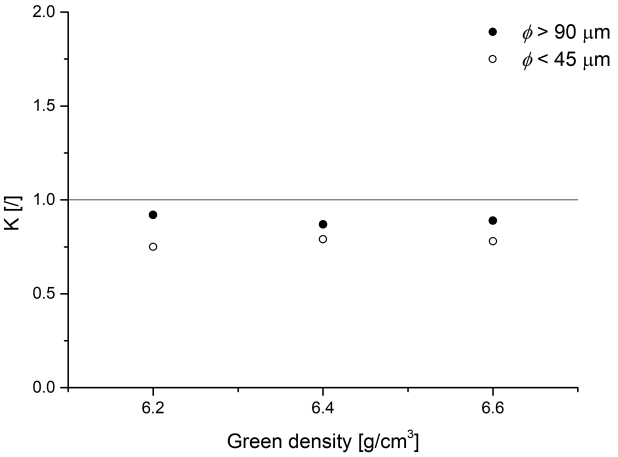

Figure 5.50 Anisotropy of the isothermal shrinkage

K is < 1 for all the powders and green density since the longitudinal shrinkage is lower than the transversal one. The anisotropy is more pronounced for the fine powder, which undergoes higher shrinkages due to its greater driving force. The inversion of the anisotropy in case of high shrinkages has already been observed by Cristofolini *et al.* [18], even though in this paper what made the shrinkages change was a different sintering temperature. The motivation of this trend will be explained in the next paragraph.

In Figure 5.51 are compared the isothermal longitudinal shrinkages (left) and the isothermal transversal shrinkages (right) registered for $\phi > 90$ μm and $\phi < 45$ μm.

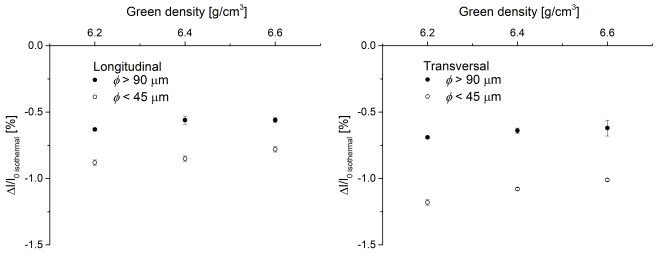

Figure 5.51 Longitudinal shrinkages as a function of green density (left) and transversal shrinkages as a function of green density (right) registered after an hour of isothermal holding

The thermodynamic driving force, that is related to the excess of surface area, enhances the isothermal shrinkages as well and, once again, the effect is more evident in the transversal direction.

5.2.3 SINTERING SHRINKAGE

The sum of the shrinkage registered on heating and the shrinkage that occurs during the isothermal holding gives the total sintering shrinkage. The results relevant to the two powders are shown in Figure 5.52.

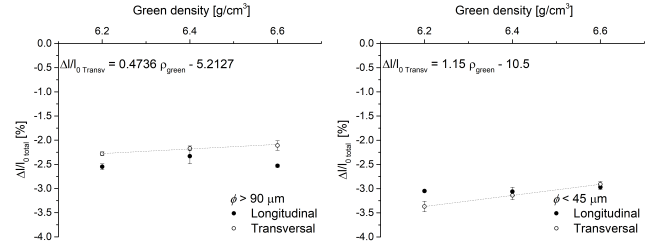

Figure 5.52 Total shrinkage vs green density in the longitudinal and transversal direction: ϕ > 90 μm (left) and ϕ < 45 μm (right)

Regarding the dimensional variations in the longitudinal direction, in case of ϕ > 90 μm, they first decrease and then increase. This behavior may be due to the opposite effect, on

increasing the green density, of the driving force (decreases) and of the geometrical activity (increases). The longitudinal shrinkage registered for the fine powder is constant. The parabolic trend of the shrinkages is evident only for the coarse powder and in the longitudinal direction because of the low ΔG and high geometrical activity.
In the transversal direction, the shrinkages decrease on increasing the green density less evidently for coarse powder and more decisively for the fine powder and in both cases the trend is linear (R^2_{coarse} = 0,95 and R^2_{fine} = 1).

Figure 5.53 allows the evaluation of the anisotropy of the sintering shrinkage as a function of the green density for the two considered powders.

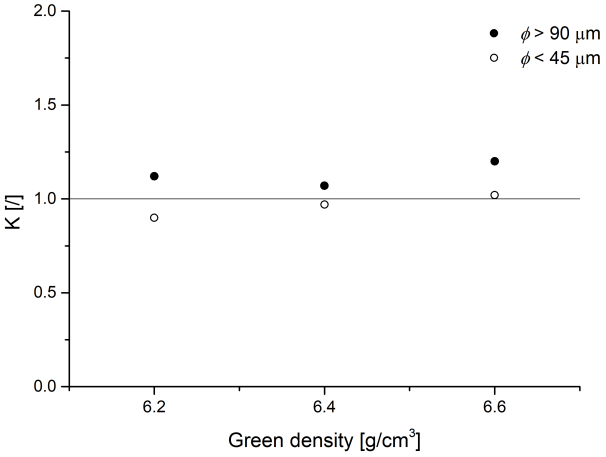

Figure 5.53 Anisotropy of the sintering shrinkage

In general, the anisotropy is very low. For the powder with particles larger than 90 μm, that is the powder that undergoes lower shrinkages, the ratio between the longitudinal and the transversal shrinkage is > 1. For the

powder with particles smaller than 45 μm the ratio is < 1 for 6.2 g/cm^3 and tends to 1 on increasing the green density.

Figure 5.54. highlights the relationship between the volumetric shrinkage and the anisotropy K. $\Delta V/V_0$ is calculated on the base of the sum of net anisothermal shrinkage and the isothermal shrinkage, since the anisothermal shrinkage that compensate the thermal expansion is recovered during cooling.

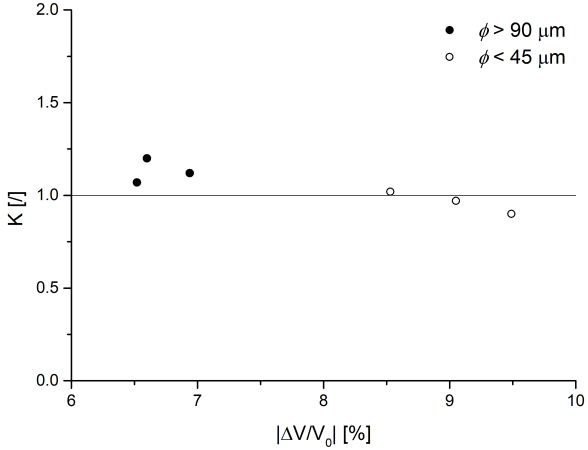

Figure 5.54 Anisotropy as a function of the volumetric shrinkage

In case of low volumetric shrinkages (ϕ > 90 μm), the anisotropy is in favor of the longitudinal shrinkage. On increasing $\Delta V/V_0$, the anisotropy parameter decreases, tends to 1 to then have an anisotropy in favor of the transversal shrinkage. To explain this trend it is advisable to see the shrinkage in terms of particles packing. On increasing the longitudinal shrinkage increases the packing of the particles in the compaction plane while the transversal shrinkage causes an increase of the packing in the direction parallel to compaction. In this context, full density coincides to a 100 % packing. When the shrinkages are low, as in the case of iron,

structural and geometrical activity act and, being greater in the compaction plane, lead to a longitudinal shrinkage higher than the transversal one. If the shrinkages are high, because of a high sintering temperature or in case of very fine powders, the full packing is approached. To reach the packing of 100 %, in the transversal direction is necessary an higher shrinkage than in the longitudinal direction since the initial contact areas are less extended, therefore there is an inversion of the anisotropy.
This result is in agreement with what predicted by the models that estimate the achievement of the theoretical density, such as [19-22].

5.3 COMPARISON BETWEEN IRON AND AISI 316L

Uniaxial cold compaction produces an anisotropic deformation of the powder particles and an inhomogeneous strain hardening of the material in the contact areas. On heating, iron starts to shrink just above 500 °C while to have shrinkage in stainless steel it is necessary to exceed 700 °C. This happens because, having AISI 316L a fcc structure, displays a low diffusivity so a high sintering temperature is required to have shrinkage and the recrystallization of the material leads to a decrease in the density of dislocations in the contact surfaces. Moreover, the increase of the bulk diffusivity thanks to the dislocation pipe diffusion on approaching the Curie temperature is strong for iron and absent in stainless steel because of its paramagnetic behavior. As a consequence, the anisothermal shrinkage for iron is affected by both the structural and the geometrical activity and for AISI 316L is mainly related to the geometrical activity. The higher anisotropy of the anisothermal shrinkage of iron respect to stainless steel is due to the contribute of

the structural activity, which is substantially absent for AISI 316L.

Concerning the isothermal shrinkages, both for iron and AISI 316L they are lower than the corresponding anisothermals. In particular, for the former material, they are 1/20 of the anisothermals for the longitudinal direction and 1/10 for the transversal one while for the latter material they are comparable. Even the isothermal shrinkages are anisotropic, but to a lesser extent then the anisothermals. In both cases the anisotropy may be imputed to the anisotropic geometrical activity at the sintering temperature. In case of iron, the dimensional variations in the longitudinal direction are greater than those in the transversal one. For the austenitic stainless steel, when the shrinkages are low the longitudinal shrinkage is higher than the transversal shrinkage but in case of high shrinkages behaviour is opposite. From the comparison of the total sintering shrinkage of the two materials appear that iron undergoes lower shrinkages than the austenitic stainless steel. In addition, the effect of green density is more pronounced for iron, as expected, because of the higher contribute of the structural activity.

5.4 REFERENCES

[1] S. Baselli, E. Torresani, M. Zago, I. Cristofolini, A. Molinari, Sintering shrinkage of uniaxial cold compacted iron. Part 2: Influence of the microstructure on the anisothermal and isothermal shrinkage of uniaxial cold compacted iron, Powder Metall. 61(4) (2018) 276-284.

[2] S. Baselli, A. Molinari, Sintering shrinkage of uniaxial cold compacted iron: a new shrinkage kinetic equation

accounting for the microstructure of the green parts, Powder Metall. 62(1) (2019) 1-7.

[3] A. Molinari, E. Bisoffi, C. Menapace, J. Torralba, Shrinkage kinetics during early stage sintering of cold isostatically compacted iron powder, Powder Metall. 57(1) (2014) 61-69.

[4] A. Molinari, C. Menapace, E. Torresani, I. Cristofolini, M. Larsson, Working hypothesis for origin of anisotropic sintering shrinkage caused by prior uniaxial cold compaction, Powder Metall. 56(3) (2013) 189-195.

[5] A. Molinari, E. Torresani, C. Menapace, M. Larsson, The Anisotropy of Dimensional Change on Sintering of Iron, J. Am. Ceram. Soc.98 (11) (2015) 3431-3437.

[6] Y. Shima, Y. Ishikawa, H. Nitta, Y. Yamazaki, K. Mimura, M. Isshiki, Y. Iijima, Self-Diffusion along dislocations in ultra high purity iron, Mater Trans. 43(2) (2002) 173-177.

[7] E.Torresani, I. Cristofolini, A. Molinari, Study of the anisotropic microstructure of the uniaxially cold compacted green parts, Adv. Powder Metall. Part. Mater. 3 (2015) 9-18.

[8] R.M. German, Sintering theory and practice, Sinter. Theory Pract. Randall M Ger. Pp 568 ISBN 0-471-05786-X Wiley-VCH January 1996. 1 (1996).

[9] L. Kang, Sintering: Densification, Grain Growth and Microstructure, 2005, Oxford, Elsiever.

[10] E.A. Brandes, G.B. Brook, C.J. Smithells, Smithells metals reference book, Butterworth-Heinemann, 1998.

[11] A.S. Podder, I. Lonardelli, A. Molinari, H.K.D.H. Bhadeshia, Thermal stability of retained austenite in bainitic steel: an in situ study, Proc R Soc A. 467 (2011) 3141–3156.

[12] E. Friedrich, W. Schatt, Sintering of One-Component Model Systems: Nucleation and Movement of Dislocations in Necks, Powder Metall. 23 (1980) 193–197.

[13] E. Friedrich, W. Schatt, High Temperature Plasticity on Solid Phase Sintering, Sci Sinter. 15 (1983) 63–71.

[14] W. Schatt, E. Friedrich, Dislocation-Activated Sintering Processes, in: G.C. Kuczynski, D.P. Uskoković, H.P. III, M.M. Ristić (Eds.), Sintering'85, Springer US, 1987: pp. 133–141.

[15] K. S. W. Sing, D. H. Everett, R. A. W. Haul, L. Moscou, R. A. Pieroti, J. Rouquerol, T. Siemieniewska, Reporting physisorption data for gas/solid systems with special reference to the determination of surface area and porosity, Pure Appl. Chem. 57(4) (1985) 603-619.

[16] M. Thommes, K. Kaneko, A. V. Neimark, J.P.Olivier, F. Rodriguez-Reinoso, J. Rouquerol K. S. W. Sing, Physisorption of gases, with special reference to the evaluation of surface area and pore size distribution (IUPAC Technical Report), Pure Appl. Chem. 87 (9-19) (2015) 1051-1069.

[17] Vagnon A, Lame O, Bouvard D, Di Michiel M, Bellet D, Kapelski G. Deformation of steel powder compacts during sintering: correlation between macroscopic measurement and in situ microtomography analysis. Acta Mater. 2006; 54:513-522.

[18] I. Cristofolini, F. Selber, C. Menapace, M. Pilla, A. Molinari, S. Libardi,

Anisotropy of Dimensional Variation and its Effect on Precision of Sintered Parts
Proceedings, EURO PM2012 Congress & Exhibition, Basel 16-19 September 2012, ed. EPMA, Shrewsbury (UK), vol. 1, pp. 519-524

[19] R.K. Bordia, R. Zuo, O. Guillon et al, Anisotropic constitutive laws for sintering bodies, Acta Mater. 54 (2006) 111–118.

[20] F. Wakai, K. Chihara, M. Yoshida, Anisotropic shrinkage due to particle rearrangement in sintering, Acta Mater. 55 (2007) 4553–4566.

[21] F. Wakai, Y. Shinoda, Anisotropic sintering stress for sintering of particles arranged in orthotropic symmetry, Acta Mater. 57 (2009) 3955–3964.

[22] F. Wakai, T. Akatsu, Anisotropic viscosities and shrinkage rate in sintering of particles in a simple orthorhombic structure, Acta Mater.58 (2010) 1921–1929.

6. PRELIMINARY ANALYSIS OF THE ANISOTHERMAL SHRINKAGE

Sintering shrinkage is due to the contribute of the anisothermal shrinkage and the contribute of the isothermal shrinkage. Studying the dimensional variations to validate the model for the isothermal shrinkage it has been observed that the anisothermal one is higher than the isothermal. Moreover, in the model, it is taken into consideration to calculate the geometrical activity at the sintering temperature. To understand which parameters affect it and to have full knowledge of the data considered, a preliminary study of the anisothermal shrinkage has been carried out. In this regard, the effect of the heating rate was investigated. Samples made by atomized iron powder (ASC II) at 6.5 g/cm^3, 6.9 g/cm^3 and 7.3 g/cm^3 were tested in the longitudinal direction at heating rate of 5 °C/min, 10 °C/min, 20 °C/min and 30 °C.

In the first instance let's take into account the green density 6.5 g/cm^3. Figure 6.1 shows the dilatometry curves at different heating rate.

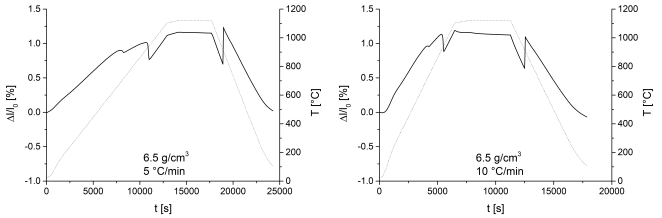

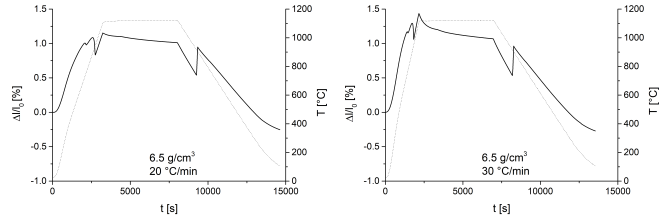

Figure 6.1 Dilatometry curves: green density 6.5 g/cm^3 and heating rate 5 °C/min, 10 °C/min, 20 °C/min and 30 °C/min

We focus on heating: in Figure 6.2 are reported the relative change in length vs temperature.

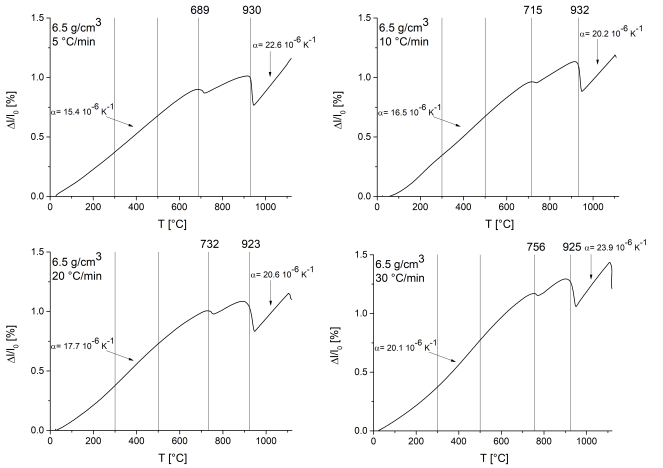

Figure 6.2 Detail of the heating step in case of green density 6.5 g/cm^3 and heating rate from 5 °C/min to 30 °C/min

From this step, information about the following parameters may be obtained:

- Thermal expansion coefficient in the temperature range 300 – 500 °C
- Temperature at which the shrinkage initiate $T_{shrinkage}$
- Temperature corresponding to the maximum of the curve before T_C, T_{max}
- Temperature of transformation from α-Fe to γ-Fe: $T_{\alpha/\gamma}$

- Anisothermal shrinkage, $\Delta l/l_{0\ aniso}$
- Thermal expansion coefficient in the temperature range $T_{\alpha/\gamma}$ -1100 °C

In the first instance, we take into account the thermal expansion coefficients (Table 6.1).

Table 6.1 Thermal expansion coefficients relevant to the temperature range 300 – 500 °C and $T_{\alpha/\gamma}$ - 1100 °C (green density 6.5 g/cm^3)

Heating rate [°C/min]	Thermal expansion coefficient 300 – 500 °C [10^{-6} K^{-1}]	Thermal expansion coefficient $T_{\alpha/\gamma}$ - 1100 °C [10^{-6} K^{-1}]
5	15.4	22.6
10	16.5	20.2
20	17.7	20.6
30	20.1	23.9

The thermal expansion coefficient in the range 300 – 500 °C increases on increasing the heating rate while the thermal expansion coefficient between $T_{\alpha/\gamma}$ and 1100 °C in coherent with the literature data 20.6 10^{-6} K^{-1} for heating rates until 20 °C/min, then increases. In Table 6.2 are summarized the results relative to the temperatures $T_{shrinkage}$, T_{max} and $T_{\alpha/\gamma}$.

Table 6.2 $T_{shrinkage}$, T_{max} and $T_{\alpha/\gamma}$ for the four heating rates considered (green density 6.5 g/cm^3)

Heating rate [°C/min]	$T_{shrinkage}$ [°C]	T_{max} [°C]	$T_{\alpha/\gamma}$ [°C]
5	508	689	930
10	520	715	932
20	507	732	923
30	620	756	925

$T_{shrinkage}$ seems not to be affected by the heating rate, except for 30 °C/min that pushes it over 600 °C. On increasing the heating rate T_{max} shifts to a higher temperature while $T_{\alpha/\gamma}$ does not change. From the curves in Figure 6.2 it may be noticed that, especially for the highest heating rates, a change in the slope is registered between 1100 °C and 1120 °C, interval in which the rate is decreased down to 1 °C/min to avoid overheating. This means that an additional contribution to the anisothermal shrinkage may be present. Therefore, we will refer to the anisothermal shrinkage up to $T_{\alpha/\gamma}$ as $\Delta l/l_{0\ aniso\ 1}$ and to the anisothermal shrinkage from 1100 °C up to 1120 °C as $\Delta l/l_{0\ aniso\ 2.}$ $\Delta l/l_{0\ aniso\ 2}$ is the difference, at 1120 °C, between the extrapolation of the line of the thermal expansion of γ-Fe and the relative change in length measured experimentally, as highlighted in Figure 6.3.

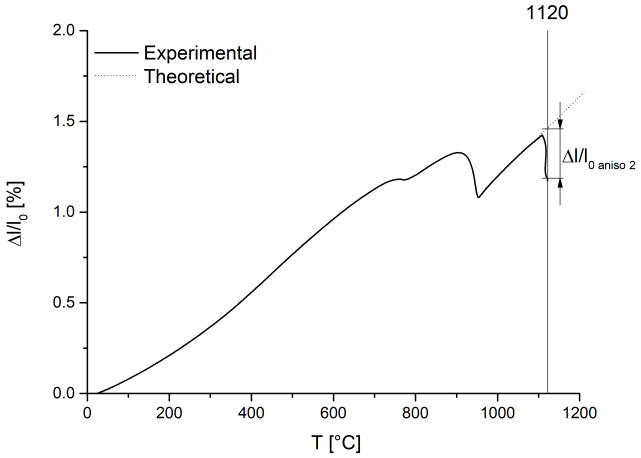

Figure 6.3 Anisothermal shrinkage from 1100 °C up to 1120 °C

Table 6.3 concerns the anisothermal shrinkages.

Table 6.3 Anisothermal shrinkages (green density 6.5 g/cm^3)

Heating rate [°C/min]	$\Delta l/l_{0\ aniso\ 1}$ [%]	$\Delta l/l_{0\ aniso\ 2}$ [%]
5	-0.35 ± 0.01	0
10	-0.35 ± 0.02	< 0.01
20	-0.42 ± 0.05	-0.09 ± 0.00
30	-0.35 ± 0.01	-0.26 ± 0.01

On increasing the heating rate $\Delta l/l_{0\ aniso\ 1}$ may be considered constant while $\Delta l/l_{0\ aniso\ 2}$ increases significantly, passing from 0 (the slope of the curve does not change) to 0.26 %. $\Delta l/l_{0\ aniso\ 2}$ is lower than the corresponding $\Delta l/l_{0\ aniso\ 1}$.

The isothermal shrinkage is plotted as a function of time in Figure 6.4.

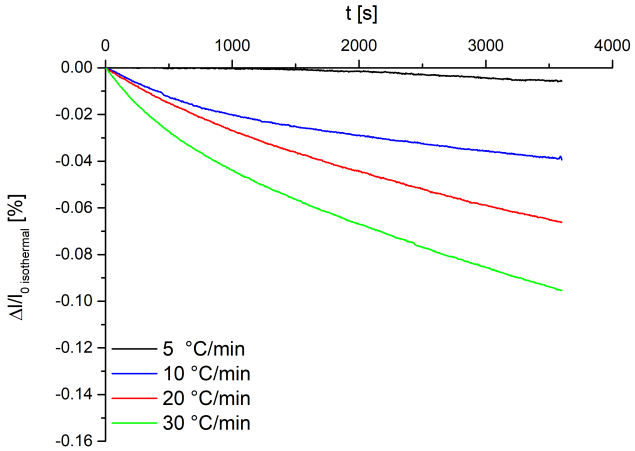

Figure 6.4 Isothermal shrinkage as a function of time in case of green density 6.5 g/cm^3 and heating rate from 5 °C/min and 30 °C/min

As previously observed, the isothermal shrinkages are lower than the corresponding anisothermals ($\Delta l/l_{0\ aniso\ 1}$ and $\Delta l/l_{0\ aniso\ 2}$, where present). In addition, it is clear that the heating

rate influences the isothermal shrinkage, in particular $\Delta l/l_{0\ iso}$ is enhanced by the increase of the heating rate.

Similar remarks can be drawn considering the green density 6.9 g/cm^3 and 7.3 g/cm^3 and the data are reported hereafter. Figures from 6.5 to 6.7 and Tables from 6.4 to 6.6 concern the green density 6.9 g/cm^3.

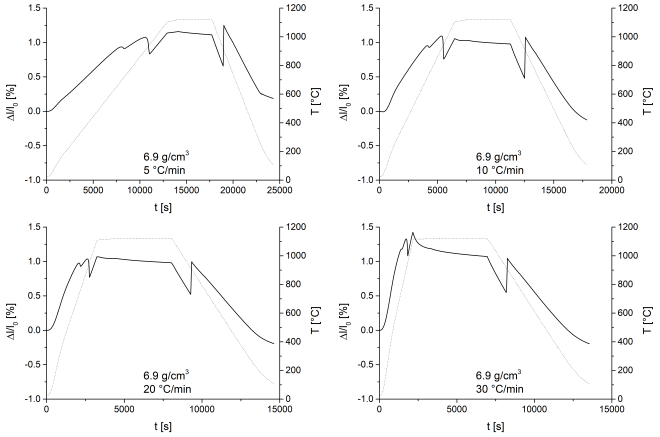

Figure 6.5 Dilatometry curves: green density 6.9 g/cm^3 and heating rate from 5 °C/min to 30 °C/min

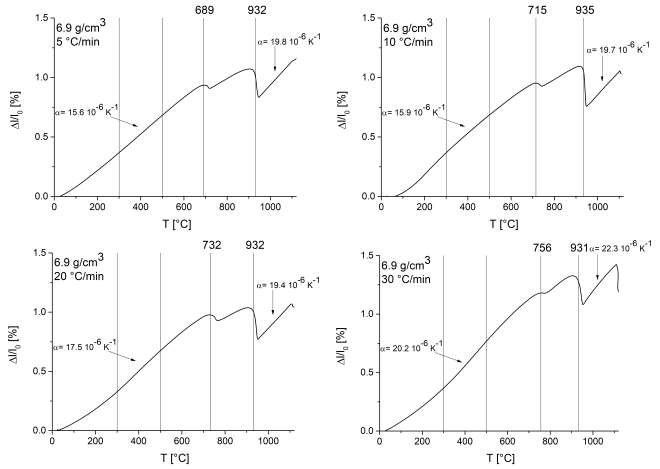

Figure 6.6 Detail of the heating step in case of green density 6.9 g/cm^3 and heating rate from 5 °C/min to 30 °C/min

Table 6.4 Thermal expansion coefficients relevant to the temperature range 300 – 500 °C and $T_{\alpha/\gamma}$ - 1100 °C (green density 6.9 g/cm^3)

Heating rate [°C/min]	Thermal expansion coefficient 300 – 500 °C [10^{-6} K^{-1}]	Thermal expansion coefficient $T_{\alpha/\gamma}$ - 1100 °C [10^{-6} K^{-1}]
5	15.6	19.8
10	15.9	19.7
20	17.5	19.4
30	20.2	22.3

Table 6.5 $T_{shrinkage}$, T_{max} and $T_{\alpha/\gamma}$ for the four heating rates considered (green density 6.9 g/cm^3)

Heating rate [°C/min]	$T_{shrinkage}$ [°C]	T_{max} [°C]	$T_{\alpha/\gamma}$ [°C]
5	515	689	932
10	520	715	935
20	510	732	932
30	620	756	931

Table 6.6 Anisothermal shrinkages (green density 6.9 g/cm^3)

Heating rate [°C/min]	$\Delta l/l_{0\ aniso\ 1}$ [%]	$\Delta l/l_{0\ aniso\ 2}$ [%]
5	-0.31 ± 0.01	0
10	-0.30 ± 0.02	< -0.01
20	-0.31 ± 0.04	-0.06 ± 0.02
30	-0.32 ± 0.01	-0.29 ± 0.02

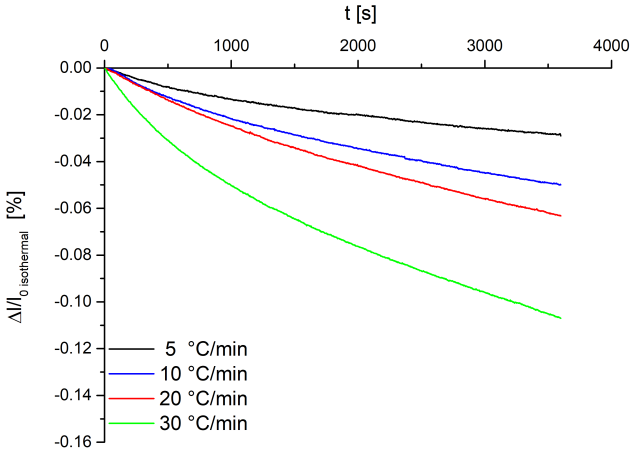

Figure 6.7 Isothermal shrinkage as a function of time in case of green density 6.9 g/cm^3 and heating rate from 5 °C/min and 30 °C/min

Figures from 6.8 to 6.10 and Tables from 6.7 to 6.9 are related to the density 7.3 g/cm^3.

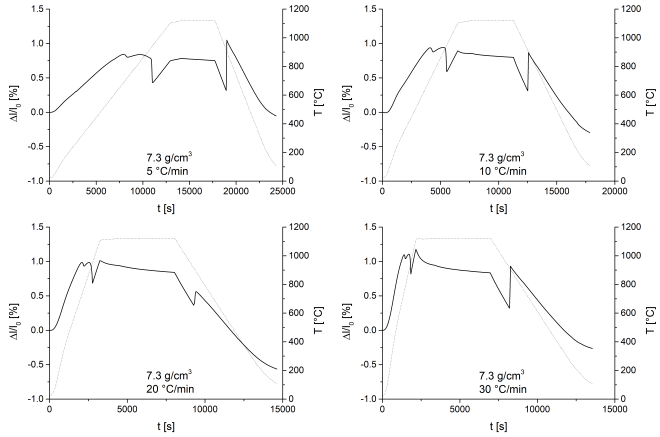

Figure 6.8 Dilatometry curves: green density 7.3 g/cm^3 and heating rate from 5 °C/min to 30 °C/min

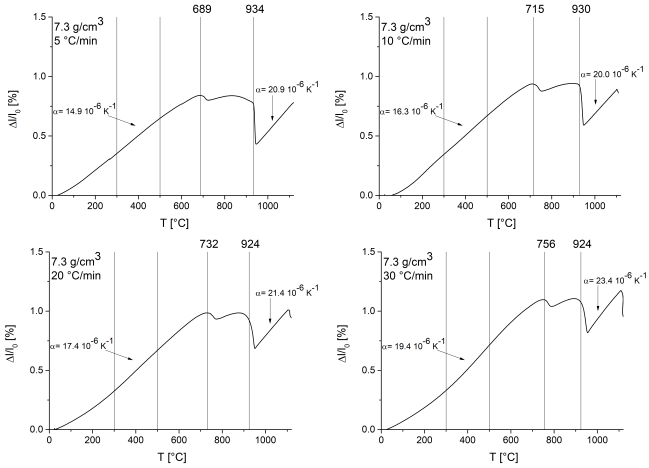

Figure 6.9 Detail of the heating step in case of green density 7.3 g/cm^3 and heating rate from 5 °C/min to 30 °C/min

The curves relevant to the density 7.3 g/cm^3 are characterized by a less intense expansion after T_C if compared to those relative to the density 6.5 g/cm^3 (Figure 6.2) and 6.9 g/cm^3 (Figure 6.6).

Table 6.7 Thermal expansion coefficients relevant to the temperature range 300 – 500 °C and $T_{\alpha/\gamma}$ - 1100 °C (green density 7.3 g/cm^3)

Heating rate [°C/min]	Thermal expansion coefficient 300 – 500 °C [10^{-6} K^{-1}]	Thermal expansion coefficient $T_{\alpha/\gamma}$ - 1100 °C [10^{-6} K^{-1}]
5	14.9	20.9
10	16.3	20.0
20	17.4	21.4
30	19.4	23.4

Table 6.8 $T_{shrinkage}$, T_{max} and $T_{\alpha/\gamma}$ for the four heating rates considered (green density 7.3 g/cm^3)

Heating rate [°C/min]	$T_{shrinkage}$ [°C]	T_{max} [°C]	$T_{\alpha/\gamma}$ [°C]
5	510	689	934
10	520	715	930
20	510	732	924
30	630	756	924

Table 6.9 Anisothermal shrinkages (green density 7.3 g/cm^3)

Heating rate [°C/min]	$\Delta l/l_{0\ aniso\ 1}$ [%]	$\Delta l/l_{0\ aniso\ 2}$ [%]
5	-0.49 ± 0.05	0
10	-0.54 ± 0.01	< -0.01
20	-0.51 ± 0.03	-0.11 ± 0.02
30	-0.56 ± 0.04	-0.27 ± 0.01

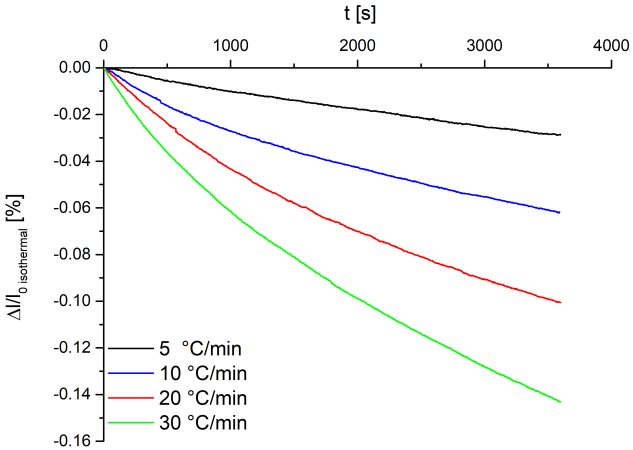

Figure 6.10 Isothermal shrinkage as a function of time in case of green density 7.3 g/cm^3 and heating rate from 5 °C/min and 30 °C/min

By the comparison of the data reported in Table 6.1, Table 6.4 and Table 6.7 it may be concluded that the thermal expansion coefficient between 300 °C and 500 °C increases

on increasing the heating rate, for all the green density, while the thermal expansion coefficient relative to γ-Fe corresponds to literature data for heating rates until 20 °C/min, then increases.

Table 6.2, Table 6.5 and Table 6.8 show that the temperature at which the shrinkage begins $T_{shrinkage}$ is around 515 °C as long as the heating rate is lower or equal to 20 °C. In case of heating rate of 30 °C/min, $T_{shrinkage}$ increases significantly, exceeding 600 °C. This result suggests that there is a dependence on the heating rate that becomes evident only for high rates. An attempt to carry out tests at higher rates has been made but the experimental set up does not allow it because of a high thermal inertia. T_{max} is independent from the green density but it is affected by the heating rate. In fact, it increases from 689 °C to 756 °C by varying the heating rate from 5 °C/min to 30 °C/min. Neither the green density nor the heating rate influence $T_{\alpha/\gamma}$.

In Figure 6.11 the anisothermal shrinkage up to $T_{\alpha/\gamma}$ is plotted as a function of the heating rate. The curves are parametric respect to the green density.

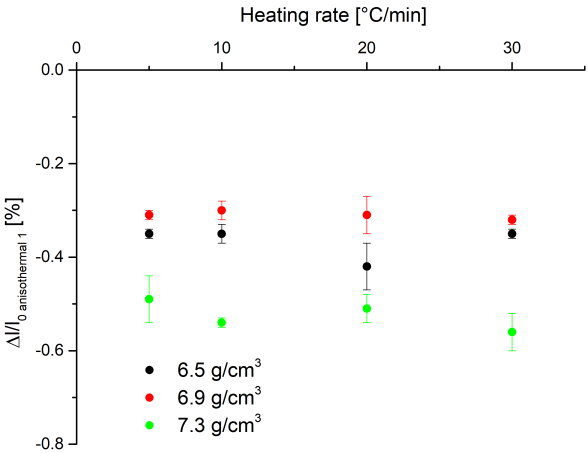

Figure 6.11 Anisothermal shrinkage up to $T_{\alpha/\gamma}$ vs heating rate for the green density 6.5 g/cm^3, 6.9 g/cm^3 and 7.3 g/cm^3

$\Delta l/l_{0\ aniso\ 1}$ is not affected by the heating rate but depends on the green density. The average values for each green density are listed in Table 6.10.

Table 6.10 Average values of the anisothermal shrinkages up to $T_{\alpha/\gamma}$

Green density [g/cm^3]	$\Delta l/l_{0\ aniso\ 1}$ [%]
6.5	-0.37 ± 0.03
6.9	-0.31 ± 0.01
7.3	-0.53 ± 0.03

Figure 6.12 shows the anisothermal shrinkages from 1100 °C up to 1120 °C vs the heating rate for each green density.

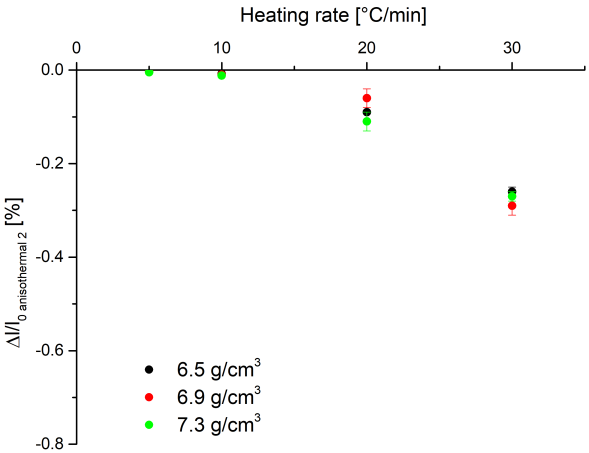

Figure 6.12 Anisothermal shrinkage from 1100 °C up to 1120 °C vs heating rate for the green density 6.5 g/cm^3, 6.9 g/cm^3 and 7.3 g/cm^3

In case of low heating rates (5 °C/min and 10 °C/min), $\Delta l/l_{0\ aniso\ 2}$ is equal to 0. For 20 °C/min and 30 °C/min, $\Delta l/l_{0\ aniso\ 2}$ increases on increasing the heating rate. Considering the heating rate 20 °C/min, the shrinkages relevant to the three green density are basically overlapped and the same may be observed for 30 °C/min. This result suggests that there is no effect of the green density on $\Delta l/l_{0\ aniso\ 2}$. The mean values for each heating rate are reported in Table 6.11.

Table 6.11 Mean anisothermal shrinkages from 1100 °C up to 1120 °C for each heating rate

Heating rate [°C/min]	$\Delta l/l_{0\ aniso\ 2}$ [%]
5	0
10	0
20	-0.09 ± 0.02
30	-0.27 ± 0.01

In Figure 6.13 are reported the isothermal shrinkages as a function of the heating rate for the green density taken into account.

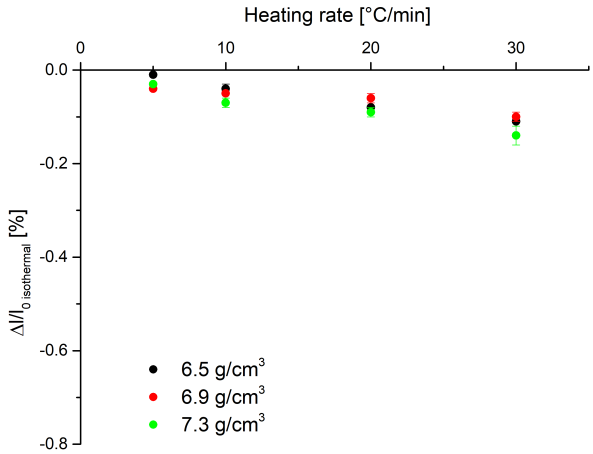

Figure 6.13 Isothermal shrinkage vs heating rate for the green density 6.5 g/cm^3, 6.9 g/cm^3 and 7.3 g/cm^3

The isothermal shrinkages are lower than the corresponding $\Delta l/l_{0\ aniso\ 1}$. In addition, $\Delta l/l_{0\ iso}$ is not affected by the green density and increases on increasing the heating rate. For each heating rate, a mean isothermal shrinkage may be calculated and the results are listed in Table 6.12.

Table 6.12 Mean isothermal shrinkages for each heating rate

Heating rate [°C/min]	$\Delta l/l_{0\ iso}$
5	-0.03 ± 0.01
10	-0.05 ± 0.01
20	-0.08 ± 0.01
30	-0.12 ± 0.01

To conclude, the anisothermal shrinkage is given by two contributes: $\Delta l/l_{0\ aniso\ 1}$ from room temperature up to $T_{\alpha/\gamma}$ and $\Delta l/l_{0\ aniso\ 2}$ from 1100 °C up to 1120 °C. The former

depends on the green density but it is not influenced the heating rate. The latter is not registered for low heating rates then it increases on increasing the heating rate but it is not affected by the green density. A similar trend characterizes the isothermal shrinkage that is not affected by the green density but it is enhanced by high heating rate.

Therefore:

- in the segment of the cycle characterized by different heating rate, the shrinkage ($\Delta l/l_{0\ aniso\ 1}$) does not depend on the rate
- in the segments identical for all the cycles (heating at rate 1 °C/min and isothermal holding) the shrinkages ($\Delta l/l_{0\ aniso\ 2}$ and $\Delta l/l_{0\ iso}$) increase with the heating rate.

These aspects introduce a further complication in the possibility of prediction of the anisothermal shrinkages and a significant amount of work is needed to clarify them.

7.CONCLUSIONS

The anisotropic sintering shrinkage of iron and austenitic stainless steel AISI 316L was investigated in the present PhD thesis through an experimental approach. The dimensional changes were measured by means of dilatometry tests and the green parts were characterized in terms of microstructure. The results have been critically discussed on the base of the concepts of geometrical and structural activity. Both affect the sintering shrinkage: the former is related to extension the interparticle contact areas while the latter deals with the non equilibrium structural defectiveness in the contacts.

In the first part, a novel kinetic equation for the isothermal shrinkage that accounts for the extension of the interparticle contact areas has been developed. It is based on a simplified geometrical model where two spherical particles with the same diameter are in contact over a surface and the mass transport mechanism responsible for neck growth and shrinkage is volume diffusivity. The equation shows that shrinkage is enhanced by the increase in the internal neck radius. This phenomenon represents the geometrical activity in sintering of prior cold compacted powders. Moreover, for the same isothermal time, shrinkage increases on decreasing the particle size. Thanks to the present equation, the structural activity during the isothermal holding may be indirectly estimated considering the experimental shrinkage. The geometrical model assumes particles with the same diameter, while powders have a particle size distribution. The main issue in introducing this characteristic is related to

the selection of the most representative combinations of particle size in contact after prior compaction, which should be supported by either a detailed investigation of the green microstructure or by a physical modelling of the deformation promoted by compaction in the particulate body, that is still quite hard in case of particles of different dimensions.

The effect of the green density on the geometrical activity of the green parts and on the sintering shrinkage has been studied with the atomized iron powder. The geometrical activity was found to be anisotropic, the contacts that contribute to the longitudinal shrinkage are larger than those contribute to the transversal one. Moreover, both of them increase linearly on increasing the green density. Concerning the sintering shrinkage, it is the sum of the anisothermal and the isothermal one. The analysis of the dilatometry curves demonstrated that shrinkage initiates on heating above 500 °C, temperature at which the diffusive mechanisms that involve atoms from the bulk are sufficiently active thanks to the presence of dislocations, and increases up to the transformation from α-Fe to γ-Fe. The anisothermal shrinkage is higher and more affected by the green density in the longitudinal direction than in the transversal one. The trend, characterized by the presence of a minimum around 6.9 g/cm^3, is due to the combination of the opposite effect of geometrical and structural activity (increase) and driving force related to the excess of surface area (decreases), on increasing the green density. The anisotropy may be imputed to the anisotropic geometrical and structural activity. Due to the recrystallization of the material during the bcc to fcc transformation, no dislocation activate shrinkage occurs in the γ-field on heating. The isothermal shrinkages are lower than the corresponding anisothermals because of the lower self-diffusion coefficient for fcc than bcc iron and the absence, in γ-field, of the structural defectiveness introduced by cold compaction. A trend depending on the green density

cannot be identified and the anisotropy is less pronounced than that characterizes the anisothermal shrinkages due to the lack of the contribute of the structural activity introduced by prior cold compaction. Considering the geometrical activity at the sintering temperature, the theoretical isothermal shrinkages were calculated. The anisotropy is correctly predicted, nevertheless the shrinkages do not fit perfectly the experimental data. The inaccuracies may be attributed to the approximations introduced both in the development and in the application of the model. Particular importance has the fact of having neglected the particle size distribution and the introduction of the bulk diffusivity of pure iron, constant in time so that effect of self-activation of sintering is not taken into account. The structural activity during the isothermal holding has resulted to be isotropic, demonstrating that the anisotropy of isothermal shrinkage is related to the geometrical activity.

The comparison of the shrinkages relevant to the samples of atomized iron and sponge with the same green density highlighted that, on heating, the effect of deformation prevails over that of the specific surface area. On the contrary, the isothermal shrinkage is significantly higher for the sponge iron and the difference is more evident in the longitudinal direction. Therefore, the excess of the specific surface area causes a general increase in the isothermal shrinkage, independently from the direction, but the shape of the particles and the porosity inside them enhance the shrinkage in the longitudinal direction.

For austenitic stainless steel it is expected a poor influence of the structural activity introduced by prior cold compaction. In fact, AISI 316L is paramagnetic and, being fcc, requires high sintering temperatures (above recrystallization) so that there is shrinkage. The dependence of the sintering shrinkage of such a material on the driving force related to the particle size has been evaluated by means of samples made by two powders at different granulometry. The results

showed a limited dependence of the shrinkages on the green density, both as regards anisothermals and isothermals. The small size of the particles increases both of them due to a greater driving force. This is particularly evident in the transversal direction, the reasons are currently unknown and deserve further investigation. The anisotropy is really modest, where present. For anisothermal shrinkage it is less than that recorded for iron due to the lack of the structural activity, for isothermal shrinkage it is even opposite, being the transversal shrinkage greater than the longitudinal one. If we consider the total volumetric shrinkage it can be observed that, as it increases, the anisotropy decreases until it reverses. This behavior finds evidences in literature and can be justified considering that, to reach the full density, in the transversal direction is required a higher shrinkage than in the longitudinal one since the initial contact areas are less extended.

Given the relevance of the anisothermal shrinkage on the total sintering shrinkage and the need to consider it for the prediction of isothermal shrinkage, a preliminary investigation has been carried out to understand if and how it is affected by the heating rate. It emerged that even the anisothermal shrinkage is due to two contributes: in addition to that up to $T_{\alpha/\gamma}$, another one is recorded during the last part of the heating step, when the rate is reduced to 1 °C/min, in case of high heating rates (> 20 °C/min). They show a different dependence on the heating rate: the former is not affected while the latter is enhanced. In addition, the isothermal shrinkage is increased by the heating rate. The phenomenon is very complex and a more extensive investigation is necessary for a full comprehension.

To conclude, future developments of the work may be

- the introduction, in the kinetic model for the isothermal shrinkage, of the dependence on the particle size distribution

- an accurate study and the modeling of the anisothermal shrinkage

Both of them are quite challenging tasks which would represent significant steps forward for the study and the prediction of sintering shrinkage.

8. SCIENTIFIC PRODUCTION

PAPERS ON JOURNAL

S. Baselli, E. Torresani, M. Zago, I. Cristofolini, A. Molinari, Sintering shrinkage of uniaxial cold compacted iron. Part 2: Influence of the microstructure on the anisothermal and isothermal shrinkage of uniaxial cold compacted iron, Powder Metall. 61(4) (2018) 276-284.

S. Baselli, A. Molinari, Sintering shrinkage of uniaxial cold compacted iron: a new shrinkage kinetic equation accounting for the microstructure of the green parts, Powder Metall. 62(1) (2019) 1-7.

S. Baselli, A. Molinari, Attività strutturale e geometrica in sinterizzazione, La Metallurgia Italiana 6 (2019) 5-10.

S. Baselli, A. Molinari, A dilatometry study of the influence of green density on anisothermal and isothermal shrinkage of plain iron green parts, Powder Metallurgy
DOI: 10.1080/00325899.2020.1777723

CONFERENCE PROCEEDINGS

A. Molinari, S. Baselli, E. Torresani, L'equazione della cinetica del ritiro dei verdi ottenuti per pressatura a freddo, 36° Convegno Nazionale AIM, Parma, 2016

A. Molinari, S. Baselli, E. Torresani, I. Cristofolini, M. Larsson, The

shrinkage of uniaxially cold compacted iron green parts, World PM2016 Congress and Exhibition, Hamburg, 2016.

S. Baselli, A. Molinari, The Geometrical Model of Sintering, Euro PM2017 Congress and Exhibition, Milano, 2017.

S. Baselli, A. Molinari, Uniaxially cold compacted green parts: shrinkage kinetic law and effective particle size, Euro PM2018, Bilbao, 2018.

S. Baselli, A. Molinari, Sintering shrinkage: effect of the prior cold compaction and effect of the surface area, Euro PM2019, Maastricht, 2019.

IN PREPARATION

S. Baselli, A. Molinari, Influence of the powder surface area on sintering shrinkage of iron green parts

ACKNOWLEDGMENTS

I wish to thank Professor Alberto Molinari for the passion for the subject of my doctoral studies, for his precious advice and the challenging discussion. I am grateful for the confidence he has always placed in me and in the work I have done.
A thanks to Professor Ilaria Cristofolini for her helpful support.
I am thankful to all the colleagues with whom I have shared this journey.